SANDIA REPORT SAND84—1101 • Unlimited Release • UC—70
Printed December 1985

Nevada Nuclear Waste Storage Investigations Project

Uniaxial and Triaxial Compression Test Series on Topopah Spring Tuff From USW G-4, Yucca Mountain, Nevada

Francis B. Nimick, Ronald H. Price, Richard G. Van Buskirk,
John R. Goodell

Prepared by
Sandia National Laboratories
Albuquerque, New Mexico 87185 and Livermore, California 94550
for the United States Department of Energy
under Contract DE-AC04-76DP00789

8608150064 860304
PDR WASTE
WM-11 PDR

SF2900Q(8-81)

"Prepared by Nevada Nuclear Waste Storage Investigations (NNWSI) Project participants as part of the Civilian Radioactive Waste Management Program (CRWM). The NNWSI Project is managed by the Waste Management Project Office (WMPO) of the U. S. Department of Energy, Nevada Operations Office (DOE/NV). NNWSI Project work is sponsored by the Office of Geologic Repositories (OGR) of the DOE Office of Civilian Radioactive Waste Management (OCRWM)."

Issued by Sandia National Laboratories, operated for the United States Department of Energy by Sandia Corporation.

NOTICE: This report was prepared as an account of work sponsored by an agency of the United States Government. Neither the United States Government nor any agency thereof, nor any of their employees, nor any of their contractors, subcontractors, or their employees, makes any warranty, express or implied, or assumes any legal liability or responsibility for the accuracy, completeness, or usefulness of any information, apparatus, product, or process disclosed, or represents that its use would not infringe privately owned rights. Reference herein to any specific commercial product, process, or service by trade name, trademark, manufacturer, or otherwise, does not necessarily constitute or imply its endorsement, recommendation, or favoring by the United States Government, any agency thereof or any of their contractors or subcontractors. The views and opinions expressed herein do not necessarily state or reflect those of the United States Government, any agency thereof or any of their contractors or subcontractors.

Printed in the United States of America
Available from
National Technical Information Service
U.S. Department of Commerce
5285 Port Royal Road
Springfield, VA 22161

NTIS price codes
Printed copy: A06
Microfiche copy: A01

Distribution
Category UC-70

SAND84-1101
Unlimited Release
Printed December 1985

Uniaxial and Triaxial Compression Test Series on Topopah Spring Tuff from USW G-4, Yucca Mountain, Nevada

Francis B. Nimick
Geotechnical Projects Division
Sandia National Laboratories
Albuquerque, New Mexico 87185

Ronald H. Price
Geomechanics Division
Sandia National Laboratories
Albuquerque, New Mexico 87185

Richard G. Van Buskirk and John R. Goodell
Terra Tek Research
Salt Lake City, Utah 84108

ABSTRACT

Fifty-seven uniaxial and triaxial compression experiments were performed on cylindrical samples taken from the Topopah Spring Member of the Paintbrush Tuff from drillhole USW G-4 at Yucca Mountain in southern Nevada. All of the samples were nominally 25.4 mm in diameter, 50.8 mm in length, and 100% water saturated. All samples were deformed in compression at room temperature under confining pressures ranging from atmospheric to 10 MPa and nominal strain rates from 10^{-7} to 10^{-3} s^{-1}.

Table of Contents

Section	Page
INTRODUCTION	5
EXPERIMENTAL TECHNIQUES	6
EXPERIMENTAL RESULTS	10
SUMMARY	14
REFERENCES	15
TABLES	17
FIGURES	31
DISTRIBUTION LIST	106

List of Tables

Table	Title	Page
1	Symbols, Abbreviations, Definitions, Conventions, and Units	17
2	Load Cell, Axial Gage, and Lateral Gage Calibration Data (SNL)	19
3	Aluminum Sample Calibration Data (SNL)	20
4	Load Cell, Axial Gage, and Lateral Gage Calibration Data (TTR)	21
5	Aluminum Sample Calibration Data (TTR)	22
6	Test Sample Information	23
7	Brief Sample Descriptions	25
8	Summary Test Results	28
9	Ranges of Mechanical Property Data	30

List of Figures

Figure	Title	Page
1	Location map of the Nevada Test Site, Yucca Mountain, and Drillhole USW G-4.	31
2	Plots of axial stress versus axial strain and axial strain versus lateral strain data with linear, least-squares fits for pre- and post-test series system calibrations at SNL with a 6061-T651 aluminum sample.	32
3	Plots of axial stress versus axial strain and axial strain versus lateral strain data with linear, least-squares fits for pre-, intra-, and post-test series system calibrations at TTR with a 6061-T651 aluminum sample.	36
4	Plots of axial stress versus axial strain for the densely welded, devitrified samples.	44
5	Plots of axial stress versus axial strain for the moderately welded, vitric samples.	81
6	Plots of axial stress versus axial strain for the partially welded, vitric samples.	86
7	Plots of axial stress versus axial strain for the nonwelded, zeolitized samples.	94
8	Plots of confining pressure versus ultimate differential stress.	100
9	Plots of log strain rate versus ultimate differential stress.	103

INTRODUCTION

Yucca Mountain, located near the southwest margin of the Nevada Test Site (NTS) in southern Nevada (Figure 1), is being evaluated as a potential site for the underground disposal of radioactive wastes. Yucca Mountain consists primarily of layered volcanic tuff (Bish et al., 1981). At present, the Topopah Spring Member of the Paintbrush Tuff is being tested for physical, thermal, and mechanical properties as part of the Nevada Nuclear Waste Storage Investigations (NNWSI) Project, which is administered by the Nevada Operations Office of the U.S. Department of Energy (DOE). The mechanical property data contained in this report ultimately will be used to aid in assessing the mineability and stability of underground openings in the Topopah Spring Member and to evaluate predicted near- and far-field responses to the presence of a repository within the unit.

This report is the fifth (see Olsson and Jones, 1980; Price, Nimick, and Zirzow, 1982; Price, Spence, and Jones, 1984; Price et al., 1985) that presents data from mechanical tests conducted on intact samples of the Topopah Spring Member. The test specimens used in this study were obtained from Drillhole USW G-4 (see Figure 1 for location) core at 12 different stratigraphic levels ranging in depth from 209.3 to 426.9 m (686.6 to 1400.6 ft). Water-saturated samples were deformed in compression at room temperature under confining pressures ranging from atmospheric to 10 MPa and at nominal strain rates of 10^{-7} to 10^{-3} s^{-1}.

All symbols and abbreviations used in this report can be found in Table 1. Within this table the terms are defined, conventions explained, and standard units assigned. The sample/test identification used throughout this report consists of seven or eight numbers and letters representing the drillhole (G4), sample depth (in feet), and individual sample identification in the form of a one-letter suffix.

This test series includes tests performed at Terra Tek Research (TTR) in Salt Lake City, Utah, and at Sandia National Laboratories (SNL) in Albuquerque, New Mexico. Distinction is made between the two laboratories as necessary in subsequent sections of this report.

EXPERIMENTAL TECHNIQUES

Test Apparatus and Techniques

Sandia National Laboratories

The experiments at SNL were performed on a load frame having a maximum load capacity of 1.0 MN (220 kip). A constant displacement rate of the loading piston is achieved by servo-control of the hydraulic loading ram while monitoring a linear variable displacement transformer (LVDT) at the base of the loading column.

Throughout this test series, axial stress (σ_1) was calculated by dividing the force measured on a standard load cell by the original cross-sectional area of the sample. Axial strain (ϵ_1) was calculated by averaging the measured displacements on two diametrically opposed LVDTs mounted directly on the sample and dividing by the average value of the original gage lengths. Lateral (transverse) displacement was measured across one sample diameter by a disk gage (as described by Schuler, 1978). Lateral strain ($\epsilon_2 = \epsilon_3$) was then obtained by dividing the displacement by the original diameter of the test specimen. Axial force, axial displacement, transverse displacement, ram displacement, and time data were collected, reduced, and plotted by a mini-computer, and stored on floppy disks.

Terra Tek Research

The experiments at TTR were performed on a load frame having a maximum load capacity of 1.1 MN. A constant displacement rate of the loading piston was achieved by servo-control of the hydraulic loading ram with servo-feedback from an LVDT mounted at the top of the loading column. The LVDT had been calibrated to be accurate to 0.03 mm. Confining pressure was applied to the sample with silicon oil.

Axial stress (σ_1) was calculated by dividing the force, measured on a standard load cell, by the original cross-sectional area of the sample. Axial strain (ϵ_1) was calculated by averaging the measured displacements on two cantilever gages mounted on the endcaps at 90° to each other around the circumference of the sample and then by dividing the average displacement by the average value of the original gage lengths. Lateral (transverse) displacements were measured with 2 cantilever gages across 2 sample diameters at 90° to each other. Average lateral strain (assuming $\epsilon_2 = \epsilon_3$) was then

obtained by dividing the average displacement by the average value of the original diameter of the sample. Axial force, axial displacement, transverse displacement, ram displacement, and time data were collected, reduced, and stored on magnetic tapes.

Calibrations

Sandia National Laboratories

The test system load cell is calibrated once a year against a standard transducer that is traceable to the U. S. Bureau of Standards (USBS). The axial displacement LVDT gage sets and transverse displacement gage were calibrated with a standard micrometer head (also traceable to the USBS) before the test series. Calibration data for the load cell, LVDTs, and disk gage are listed in Table 2.

Calibrations of the experimental methods and of the entire instrumentation setup were obtained preceding and following the tuff sample experiments by testing an aluminum sample of known mechanical properties. The gages were tested on a 6061-T651 aluminum cylinder (25.4 by 50.8 mm) with a Young's modulus (E) of 69.7 GPa and a Poisson's ratio (ν) of 0.333. The calibration check test data are listed in Table 3 and plotted in Figure 2. Also shown in Figure 2 are least-squares fit lines used to obtain the elastic properties noted on the plots.

Terra Tek Research

The test system load cell is calibrated before each test series against a standard transducer that is traceable to the USBS. The axial and transverse displacement gages were also calibrated immediately before the test series. Calibration data for the load cell, axial, and transverse gages are listed in Table 4.

The experimental design at TTR results in the inclusion of some endcap deformation in the axial displacement measurements. This deformation must be determined as a function of axial stress in order to calculate the actual deformation of a test sample. To estimate the correction factor, a sample of known properties is deformed, the ideal and actual displacements are compared, and the difference at a given stress is assumed to be the correction value at that stress. The stress and correction factor values are fit by the method of least squares to determine an equation that calculates a correction

factor at any given stress, and this correction is applied when running an actual test sample.

A sample of 6061-T651 aluminum was used as the standard for this test series. The correction factor/stress relationship was determined before the test series and was used in correcting subsequent aluminum runs. The results for the four aluminum tests are listed in Table 5 and plotted in Figure 3. Also shown in Figure 3 are least-squares fit lines used to obtain the elastic properties noted on the plots.

During the data reduction process at TTR, the procedure described above was modified slightly. Although data from the last 3 aluminum runs were corrected using the correction factor from the first aluminum run, this correction factor was used only in the first 17 rock tests. Subsequent rock tests were corrected using data from the most recent preceding aluminum test. Thus, 25 rock tests were corrected using data from the second aluminum test and 10 tests with data from the third aluminum test.

Comparison of Figures 2 and 3 suggests that elastic moduli data measured at TTR have greater uncertainties than those measured at SNL. Although the Young's moduli in the TTR pre- and post-test series are comparable to those obtained at SNL, an uncertainty in the Young's moduli measurements of approximately 7% should be assumed for the rock samples tested at TTR in order to be conservative.

Subsequent to the completion of this test series, TTR discovered in the course of a test series on materials with well-known mechanical properties that a small systematic error in the measured transverse displacements had been occurring for some time. [The test series is discussed by Nimick (1985)]. This error resulted in errors in the Poisson's ratio measurements for tests during the time interval. The pre- and post-test aluminum tests at TTR (Figures 3B and 3H) showed high values of Poisson's ratio, suggesting that a similar error occurred in these tests. Based on this observation, it should be assumed that Poisson's ratios for the rock samples tested at TTR are 10% higher than actual values.

Sample Preparation

The 57 test specimens were all right-circular cylinders machined from Drillhole USW G-4 core material. The samples ranged in diameter from 25.2 to 25.3 mm and in length from 49.9 to 50.9 mm. The sample IDs, depths, diameters, lengths, functional porosities, and average grain densities are listed in Table 6. The porosity and grain density values were determined from data contained in Nimick, Price, and Schwartz (in

preparation) and the montmorillonite values from Bish and Vaniman (in preparation). The specific values for each depth given in Table 6 were linearly interpolated from data on samples from depths as close to the mechanical test specimens as possible. In addition, a brief physical description of each sample is contained in Table 7.

All samples were stored in groundwater from Well J-13 (NTS). Before testing, most of the samples were subjected to 3 or more vacuum saturation cycles that included at least 45 hr under an active vacuum and 24 hr at ambient pressure. The samples were considered to be saturated when the weight gain after a given saturation step was less than or equal to 0.05% of the weight at the beginning of the step. Five of the samples (910.7-A, 965.2-A, 1001.9-A, 1065.8-A, and 1307.2-A) were frozen during the first vacuum cycle to which they were subjected because of an inadequate supply of water in the vacuum chamber. In addition, these 5 samples and 12 others (686.6-A, 686.6-G, 742.75-E, 742.75-F, 748.6-A, 748.6-B, 911.3-C, 1307.2-C, 1369.1-E, 1369.1-F, 1400.6-A, and 1400.6-E) were subjected to only 1 vacuum cycle before testing. The effect of this discrepancy on mechanical test results is discussed later in the report.

After saturation, each sample was placed between steel end pieces and jacketed in polyolefin shrink tubing (SNL) or FEP teflon tubing (TTR). The axial and transverse transducers were then mounted on the specimen, the sample assembly was placed between the loading ram and the load cell, and the test was begun.

Test Conditions

All samples were deformed in compression under saturated, drained, constant confining pressure, room temperature, and constant strain rate conditions. Four samples were run at 5 MPa confining pressure, 6 were run at 10 MPa, and the remainder were tested at atmospheric confining pressure. All triaxial tests were deformed at a nominal strain rate of 10^{-5} s^{-1}. Of the unconfined tests, 6 were deformed at a nominal strain rate of 10^{-7} s^{-1}, 6 at 10^{-3} s^{-1}, and the remainder at 10^{-5} s^{-1}. One sample (1400.6-A) was tested with incorrect initialization of the testing equipment, and, consequently, the test results are not useable because of the lack of certainty regarding the strain rate to which the sample was subjected.

EXPERIMENTAL RESULTS

A summary of the mechanical property results is given in Table 8. The ranges of Young's moduli, Poisson's ratios, ultimate strengths, and axial strains at failure for different test conditions are summarized in Table 9. As indicated in earlier reports (e.g., Price and Nimick, 1982; Price, Spence, and Jones, 1984) and discussed in detail in Price (1983), these wide ranges are attributable to variations in the physical and mineralogic characteristics of the tuffs.

The differential stress/axial strain curves are presented in Figures 4, 5, 6, and 7. The general shapes of the stress/strain curves for the densely welded, devitrified samples are very similar to results reported for previous tests on the Topopah Spring Member (Price, Nimick, and Zirzow, 1982; Price, Spence, and Jones, 1984) and on other Yucca Mountain silicic tuffs (Price and Jones, 1982; Price, Jones, and Nimick, 1982; Price and Nimick, 1982). Samples 965.2-B and 965.2-E, tested at 10 MPa confining pressure, were slightly more ductile. [Ductility is defined as the amount of greatest principal strain prior to failure (Handin and Hager, 1957), as well as relating to the mode of sample failure: extreme brittle behavior relating to a single extension (axial) or shear fracture or extreme ductile behavior relating to a homogeneous distribution of deformation throughout the sample.] Samples from a depth of 209.3 m (686.6 ft) were also tested under confining pressures up to 10 MPa but essentially behaved in a brittle fashion.

The partially welded, vitric samples (1369.1-A to -H) underwent much more compaction at low differential stresses than did the densely welded, devitrified samples. This behavioral difference is attributable to the substantially greater porosity of the partially welded samples. Failure of the partially welded samples tended to be gradual, and a slow decline in load-bearing capacity followed the ultimate differential stress.

The zeolitized samples (1400.6-A to -H), which were tested at different confining pressures, showed strong differences in behavior at the different pressures. The samples tested at atmospheric pressure exhibited stress/strain behavior intermediate to that of the partially welded, vitric samples and that of the densely welded, devitrified samples. The application of confining pressure resulted in a distinct increase in ductility both at 5 MPa and at 10 MPa. In fact, for samples 1400.6-C, -F, and -G, the assignment of a failure stress is not clear-cut. The axial strain on sample 1400.6-C reached 0.02 without achieving an ultimate differential stress, and, at an equivalent strain, sample 1400.6-F had shown only a slight decrease in differential stress.

Compressive Strength

Seventeen of the 57 samples tested were not subjected to the same saturation procedure as that used for the remaining samples. These 17 samples underwent only one vacuum cycle, compared to 3 or more vacuum cycles for the other samples. As a result, the saturation state of the 17 samples at the time of testing was probably less than that of the remaining samples. An examination of the test results for the 17 samples showed no definitive trend in the differences in strength between them and their more completely saturated, sample counterparts from equivalent depths. Five of the 17 samples were also frozen during sample saturat' .ı. The freezing does not appear to have caused any significant differences in strengtl results.

Analysis of test results on many tuff samples from the NTS has led to correlations of unconfined compressive strength and Young's modulus with the functional porosity of the sample, where the functional porosity is defined as the volume fraction of void space plus the volume fraction of montmorillonite in the sample (Price, 1983; Price and Bauer, 1985). The relationships are as follows:

$$E = 85.5\ exp(-6.96n) \tag{1}$$

and

$$C_0 = 4.04\ n^{-1.85}, \tag{2}$$

where E is Young's modulus (GPa), C_0 is unconfined compressive strength (MPa), and n is functional porosity (volume fraction). These correlations indicate a decrease in both modulus and strength with an increase in functional porosity.

Samples from depths between 209.3 and 324.9 m (686.6 and 1065.8 ft) are densely welded, devitrified tuff. Examination of the strength data for the densely welded, devitrified samples indicates that, although the expected trend is approximately duplicated by the experimental data, there are exceptions. Especially noteworthy is sample 1065.8-A, which has a compressive strength of 12 MPa and a functional porosity of 0.138. Using Equation 2, a strength of 12 MPa would suggest a functional porosity of about 0.55. For this sample, the functional porosity has been underestimated by a significant amount. The sample description in Table 7 indicates that not only is the porosity underestimated, but its distribution within the sample is not uniform, which may have contributed to the exceptionally low strength. Other deviations from the expected trend are attributable to the presence of such features as pre-existing fractures or relatively large pumice fragments, which are not taken into account by the functional porosity model.

The test samples from the 398.4-m (1307.2-ft) depth are from the main vitrophyre of the Topopah Spring Member. Rather than being composed primarily of glass, however, these samples contain significant quantities of clay concentrated in patches. Thus, test results for these samples are representative of the altered vitrophyre described by Levy (1984) that occurs between the welded, devitrified portion of the Topopah Spring Member and the underlying unaltered vitrophyre.

Samples from a depth of 417.3 m (1369.1 ft) are taken from the partially welded, vitric ashflow tuffs that underlie the main vitrophyre. As indicated in Table 7, these samples also contain appreciable quantities of clay. All of the samples from depths greater than 417.3 m (1369.1 ft) are zeolitized to varying degrees and are from non-welded ashflows. Both the vitric and the zeolitized samples provided data that agree with the correlation between functional porosity and compressive strength. For these two sample groups, however, the strength data show less variability than did corresponding data for welded, devitrified samples. The greater homogeneity may be attributed partly to the decreased frequency of fractures in the lower units and partly to the tendency of the process of zeolitization to homogenize the porosity within a sample.

Ultimate strength/confining pressure plots are presented in Figure 8. The results reported here do not show clearly the effect of confining pressure on the ultimate compressive strengths of the densely welded, devitrified tuffs (Figure 8A). For samples from the 209.3-m (686.6-ft) depth, the highest strengths are associated with the highest confining pressure (10 MPa), as expected. However, the lowest strengths were measured at the intermediate value of confining pressure (5 MPa), and the samples tested without confining pressure had intermediate strengths.

Samples from a depth of 294.2 m (965.2 ft) showed a slight increase in average strength for samples tested at 10 MPa relative to results from unconfined tests (Figure 8B), but the difference is not statistically significant. These results indicate that mechanical test results are influenced more by sample variability than by differences in confining pressure.

The effect of confining pressure on the strength of the zeolitized samples [from a depth of 426.9 m (1400.6 ft)] was also examined (Figure 8C). The average strength of the samples increased slightly at each increment of confining pressure between 0 and 10 MPa, but the differences are not significant relative to strength variability at any one confining pressure.

The effect of variation in strain rate on ultimate strength is graphically shown in Figure 9. The trend seems to be better defined than that of confining pressure for the densely welded samples. Testing of samples from a depth of 226.4 m (742.75 ft) showed

a decrease in strength of 4 to 7% for each order-of-magnitude decrease in strain rate (Figure 9A). A decrease in 9% per order-of-magnitude decrease in strain rate is shown by the data for samples from a depth of 305.5 m (1002.4 ft) (Figure 9B). However, the ranges in strengths at different strain rates overlap, so sample variability is still a very important factor relative to variations in strain rate. Samples from the partially welded, vitric interval [417.3 m (1369.1 ft)] were also tested to determine the dependence of the compressive strength on strain rate. Differences in results at different strain rates showed no significant trend (Figure 9C).

Young's Modulus

The 17 samples for which pre-test sample treatment was different produced test results indistinguishable from other results from equivalent depths. Thus, the results from these 17 samples are included in the discussion below.

The Young's moduli of the test samples should show a decrease with increasing functional porosity, as discussed earlier, for all samples except those from the main vitrophyre. For the densely welded, devitrified samples, this approximate trend is present, although neither the average moduli nor the porosities have large enough ranges to provide definitive information. Both the partially welded and the nonwelded samples have much higher porosities and much lower moduli than the densely welded, devitrified samples, as expected, and have mutually indistinguishable moduli.

Variation in confining pressure between 0 and 10 MPa produced no definitive trend in Young's moduli for the densely welded, devitrified samples, nor for the nonwelded, zeolitized samples. As was found for compressive strengths, the moduli are a stronger function of sample variability than of variation in confining pressure.

The same conclusion can be made for the effect of variation in strain rate on Young's modulus. Neither the densely welded, devitrified samples nor the partially welded, vitric samples showed any consistent pattern as the strain rate was varied.

SUMMARY

Fifty-seven compression experiments were performed on saturated samples at constant confining pressure, room temperature, and constant strain rate. Confining pressure was found to have no definitive effect on the strength or Young's modulus of any samples, although both densely welded, devitrified samples and zeolitized samples showed an increase in ductility at higher confining pressures. Changes in strain rate caused a decrease in strength of 4 to 9% per order-of-magnitude decrease in strain rate for the densely welded, devitrified samples but had no effect on the strength of the nonwelded samples or on the Young's moduli of any sample group.

REFERENCES

Bish, D. L., Caporuscio, F. A., Copp, J. F., Crowe, B. M., Purson, J. D., Smyth, J. R., and Warren, R. G., Preliminary Stratigraphic and Petrologic Characterization of Core Samples from USW-G1, Yucca Mountain, Nevada, Los Alamos National Laboratory Report, LA-8840-MS, Los Alamos, NM, 1981.

Bish, D. L., and Vaniman, D. T., Mineralogic Summary of Yucca Mountain, Nevada, Los Alamos National Laboratory Report, Los Alamos, NM, in preparation.

Handin, J., and Hager, R. V., Jr., Experimental Deformation of Sedimentary Rocks under Confining Pressure: Tests at Room Temperature on Dry Samples, Amer. Assoc. Petr. Geol., **41**, 1-50, 1957.

Levy, S. S., Petrology of Samples from Drill Holes USW H-3, H-4, and H-5, Yucca Mountain, Nevada, Los Alamos National Laboratory Report, LA-9706-MS, Los Alamos, NM, June 1984.

Nimick, F. B., Comparative Mechanical Testing, Unclassified memo to T. E. Blejwas, Sandia National Laboratories, Albuquerque, NM, May 1985.

Nimick, F. B., Price, R. H., and Schwartz, B. M., Bulk, Thermal and Mechanical Properties of the Topopah Spring Member of the Paintbrush Tuff, Yucca Mountain, Nevada, Sandia National Laboratories Report, SAND85-0762, Albuquerque, NM, in preparation.

Olsson, W. A. and Jones, A. K., Rock Mechanics Properties of Volcanic Tuffs from the Nevada Test Site, Sandia National Laboratories Report, SAND80-1453, Albuquerque, NM, November 1980.

Price, R. H., Analysis of Rock Mechanics Properties of Volcanic Tuff Units from Yucca Mountain, Nevada Test Site, Sandia National Laboratories Report, SAND82-1315, Albuquerque, NM, August 1983.

Price, R. H., and Bauer, S. J., Analysis of the Elastic and Strength Properties of Yucca Mountain Tuff, Nevada, in Proceedings of the 26th U. S. Symposium on Rock Mechanics, Rapid City, SD, June 26-28, 1985.

Price, R. H., and Jones, A. K., Uniaxial and Triaxial Compression Test Series on Calico Hills Tuff, Sandia National Laboratories Report, SAND82-1314, Albuquerque, NM, October 1982.

Price, R. H., Jones, A. K., and Nimick, K. G., Uniaxial Compression Test Series on Bullfrog Tuff, Sandia National Laboratories Report, SAND82-0481, Albuquerque, NM, April 1982.

Price, R. H., Nimick, F. B., Connolly, J. R., Keil, K., Schwartz, B. M., and Spence, S. J., Preliminary Characterization of the Petrologic, Bulk, and Mechanical Properties of a Lithophysal Zone Within the Topopah Spring Member of the Paintbrush Tuff, Sandia National Laboratories Report, SAND84-0860, Albuquerque, NM, February 1985.

Price, R. H., and Nimick, K. G., Uniaxial Compression Test Series on Tram Tuff, Sandia National Laboratories Report, SAND82-1055, Albuquerque, NM, July 1982.

Price, R. H., Nimick, K. G., and Zirzow, J. A., Uniaxial and Triaxial Compression Test Series on Topopah Spring Tuff, Sandia National Laboratories Report, SAND82-1723, Albuquerque, NM, October 1982.

Price, R. H., Spence, S. J., and Jones, A. K., Uniaxial and Triaxial Compression Test Series on Topopah Spring Tuff From USW GU-3, Yucca Mountain, Southern Nevada, Sandia National Laboratories Report, SAND83-1646, Albuquerque. NM, February 1984.

Schuler, K. W., Lateral-Deformation Gage for Rock Mechanics Testing, Experimental Mechanics, 18, 477-480, 1978.

Table 1a.
Symbols, Definitions, Conventions and Units

SYMBOL	DEFINITION	UNITS
E	Elastic constant : Young's modulus	GPa
ν	Elastic constant : Poisson's ratio	—
σ_1 , σ_2 , σ_3	Principal stresses, compressive stresses are positive	MPa
σ_{ax}	Stress parallel to the sample axis, $(\sigma_{ax} = \sigma_1)$	MPa
$(\Delta\sigma)_u$	Ultimate differential stress $[(\Delta\sigma)_u = \sigma_1 - \sigma_3]$	MPa
P_c	Confining pressure $(P_c = \sigma_2 = \sigma_3)$	MPa
ϵ_1 , ϵ_2 , ϵ_3	Principal strains, compressive strains are positive	
ϵ_{ax}	Strain parallel to the sample axis $(\epsilon_{ax} = \epsilon_1)$	
ϵ_{lat}	Strain perpendicular to the sample axis $(\epsilon_{lat} = \epsilon_2 = \epsilon_3)$	
$\dot{\epsilon}$	Nominal axial strain rate	s^{-1}
$(\epsilon_1)_u$	Greatest principal strain at ultimate stress	
n	Functional porosity (porosity + montmorillonite volume fraction)	
ρ_g	Average grain density	$\frac{g}{cm^3}$
f	Force f_a : actual force f_m : measured force	N
δ	Displacement δ_a : actual displacement δ_m : measured displacement	m
e_m	Error of the measured value [e.g., $100\ (f_m - f_a)/f_a$]	%

Table 1b.
Abbreviations and Definitions

ABBREVIATION	DEFINITION
SNL	Sandia National Laboratories
TTR	Terra Tek Research
DOE	Department of Energy
NTS	Nevada Test Site
NNWSI	Nevada Nuclear Waste Storage Investigations
USW G-4	Drillhole at Yucca Mountain
J-13	Drillhole east of Yucca Mountain
USBS	United States Bureau of Standards
LVDT	Linear variable displacement transformer

Table 2.
Load Cell, Axial Gage, and Lateral Gage Calibration Data (SNL)

Load Cell		
f_a (kN)	f_m (kN)	e_m (%)
44.50	44.144	-0.8
89.00	88.555	-0.5
133.5	133.10	-0.3
178.0	178.00	0.0
222.5	222.66	0.1

Axial Gage			Lateral Gage		
δ_a (mm)	δ_m (mm)	e_m (%)	δ_a (μm)	δ_m (μm)	e_m (%)
0.0000	0.0000	0.0	0.000	0.000	0.0
0.1016	0.1015	-0.1	50.80	51.49	1.4
0.2032	0.1996	-1.8	101.6	104.2	2.6
0.3048	0.2937	-3.6	152.4	156.4	2.6
0.4064	0.3974	-2.2	203.2	205.9	1.3
0.5080	0.5025	-1.1	254.0	260.8	2.7

Table 3.
Aluminum Sample Calibration Data (SNL)

Pre-Test Series			Post-Test Series		
σ_{ax} (MPa)	ϵ_{ax} (millistrain)	ϵ_{lat} (millistrain)	σ_{ax} (MPa)	ϵ_{ax} (millistrain)	ϵ_{lat} (millistrain)
0.000	0.000	0.000	0.000	0.000	0.000
7.586	0.1173	-0.04764	6.328	0.1014	-0.02037
14.94	0.2146	-0.06916	16.11	0.2423	-0.09284
22.39	0.3421	-0.1083	23.44	0.3559	-0.1167
30.10	0.4515	-0.1453	33.14	0.4898	-0.1715
37.94	0.5659	-0.1976	38.29	0.5843	-0.1879
45.48	0.6565	-0.2094	51.15	0.7529	-0.2563
53.35	0.7828	-0.2597	56.76	0.8698	-0.2802
61.40	0.8871	-0.2987	68.99	1.021	-0.3298
69.03	1.011	-0.3308	74.22	1.112	-0.3623
76.34	1.098	-0.3763	85.23	1.238	-0.4106
83.52	1.232	-0.4224	90.43	1.335	-0.4340
91.16	1.321	-0.4575	101.4	1.484	-0.4906
99.12	1.443	-0.5015	107.0	1.578	-0.5266
107.1	1.538	-0.5325	118.7	1.725	-0.5814
⋮					

Table 4.
Load Cell, Axial Gage, and Lateral Gage Calibration Data (TTR)

Load Cell			Axial Gage		
f_a (kN)	f_m (kN)	e_m (%)	δ_a (mm)	δ_m (mm)	e_m (%)
11.13	11.47	3.05	0.1524	0.1551	1.77
22.25	22.39	0.63	0.3048	0.3066	0.59
33.38	33.26	-0.36	0.4572	0.4601	0.63
44.50	44.50	0.00	0.6096	0.6091	-0.08
55.63	55.61	-0.04	0.7620	0.7581	-0.51
66.75	67.24	0.73	0.9144	0.9152	0.09
89.00	89.29	0.33	1.0668	1.0621	-0.44
111.3	111.0	-0.27	1.2192	1.2192	0.00
133.5	133.4	-0.07	1.3716	1.3722	0.04
155.8	155.6	-0.13	1.5240	1.5273	0.22

Lateral Gage 1			Lateral Gage 2		
δ_a (mm)	δ_m (mm)	e_m (%)	δ_a (mm)	δ_m (mm)	e_m (%)
0.0762	0.0752	-1.31	0.0762	0.0753	-1.18
0.1524	0.1533	0.59	0.1524	0.1548	1.57
0.2286	0.2293	0.31	0.2286	0.2306	0.87
0.3048	0.3048	0.00	0.3048	0.3047	-0.03
0.3810	0.3810	0.00	0.3810	0.3847	0.97
0.4572	0.4565	-0.15	0.4572	0.4613	0.90
0.5334	0.5344	0.19	0.5334	0.5371	0.69
0.6096	0.6099	0.05	0.6096	0.6104	0.13
0.6858	0.6853	-0.07	0.6858	0.6828	-0.44
0.7620	0.7616	-0.05	0.7620	0.7561	-0.77

Table 5.
Aluminum Sample Calibration Data (TTR)

Pre-Test Series			Intra-Test Series 1		
σ_{ax} (MPa)	ϵ_{ax} (millistrain)	ϵ_{lat} (millistrain)	σ_{ax} (MPa)	ϵ_{ax} (millistrain)	ϵ_{lat} (millistrain)
0.000	0.000	0.000	0.000	0.000	0.000
6.440	0.105	-0.038	7.690	0.106	-0.039
13.26	0.189	-0.075	14.95	0.202	-0.075
20.70	0.254	-0.121	21.92	0.312	-0.112
27.84	0.385	-0.160	29.43	0.462	-0.154
35.15	0.507	-0.196	36.34	0.550	-0.193
41.76	0.557	-0.233	43.78	0.660	-0.236
48.88	0.706	-0.277	52.23	0.796	-0.274
55.57	0.794	-0.311	59.46	0.893	-0.315
62.04	0.907	-0.342	67.13	1.010	-0.349
69.17	1.006	-0.378	75.23	1.124	-0.391
76.01	1.096	-0.408	83.13	1.248	-0.434
83.51	1.194	-0.453	91.13	1.404	-0.469
91.51	1.264	-0.501	99.23	1.510	-0.518
98.71	1.325	-0.543			

Intra-Test Series 2			Post-Test Series		
σ_{ax} (MPa)	ϵ_{ax} (millistrain)	ϵ_{lat} (millistrain)	σ_{ax} (MPa)	ϵ_{ax} (millistrain)	ϵ_{lat} (millistrain)
0.000	0.000	0.000	0.000	0.000	0.000
8.000	0.127	-0.042	8.410	0.091	-0.045
16.18	0.259	-0.084	16.68	0.250	-0.075
24.56	0.424	-0.131	29.42	0.419	-0.162
32.31	0.533	-0.168	38.07	0.515	-0.204
40.19	0.643	-0.219	46.52	0.633	-0.251
48.85	0.785	-0.262	55.37	0.795	-0.295
56.88	0.904	-0.299	63.99	0.951	-0.347
65.60	1.082	-0.345	72.75	1.021	-0.395
73.86	1.211	-0.385	81.85	1.118	-0.440
82.06	1.273	-0.434	90.75	1.323	-0.491
91.16	1.408	-0.478	104.4	1.451	-0.569
99.86	1.541	-0.522			

Table 6.
Test Sample Information

Sample ID	Depth (m)	Lab	Diameter (mm)	Length (mm)	n*	ρ_g* $(\frac{g}{cm^3})$
G4-686.6-A	209.3	TTR	25.32	50.88	0.122	2.50
G4-686.6-B	209.3	TTR	25.32	50.90	0.122	2.50
G4-686.6-C	209.3	TTR	25.32	50.88	0.122	2.50
G4-686.6-D	209.3	TTR	25.32	50.88	0.122	2.50
G4-686.6-E	209.3	TTR	25.35	50.88	0.122	2.50
G4-686.6-F	209.3	TTR	25.35	50.90	0.122	2.50
G4-686.6-G	209.3	TTR	25.30	50.85	0.122	2.50
G4-742.75-A	226.4	TTR	25.32	50.83	0.103	2.51
G4-742.75-B	226.4	TTR	25.32	50.85	0.103	2.51
G4-742.75-C	226.4	TTR	25.32	50.88	0.103	2.51
G4-742.75-D	226.4	TTR	25.32	50.88	0.103	2.51
G4-742.75-E	226.4	TTR	25.32	50.88	0.103	2.51
G4-742.75-F	226.4	TTR	25.32	50.85	0.103	2.51
G4-742.75-G	226.4	TTR	25.32	50.88	0.103	2.51
G4-742.75-H	226.4	TTR	25.32	50.88	0.103	2.51
G4-748.6-A	228.2	TTR	25.35	50.88	0.104	2.51
G4-748.6-B	228.2	TTR	25.32	50.85	0.104	2.51
G4-749.0-A	228.3	SNL	25.30	50.77	0.104	2.51
G4-749.0-B	228.3	SNL	25.30	50.77	0.104	2.51
G4-910.7-A	277.6	TTR	25.32	50.88	0.162	2.53
G4-911.3-A	277.8	SNL	25.30	50.77	0.161	2.53
G4-911.3-B	277.8	TTR	25.35	49.91	0.161	2.53
G4-911.3-C	277.8	TTR	25.32	50.85	0.161	2.53
G4-965.2-A	294.2	TTR	25.32	50.75	0.145	2.57
G4-965.2-B	294.2	TTR	25.32	50.88	0.145	2.57
G4-965.2-D	294.2	TTR	25.32	50.85	0.145	2.57
G4-965.2-E	294.2	TTR	25.32	50.88	0.145	2.57
G4-965.2-H	294.2	TTR	25.32	50.88	0.145	2.57

* These data were derived from Nimick, Price, and Schwartz (in preparation) and Bish and Vaniman (in preparation).

Table 6.
Test Sample Information (concluded)

Sample ID	Depth (m)	Lab	Diameter (mm)	Length (mm)	n*	ρ_g* ($\frac{g}{cm^3}$)
G4-1001.9-A	305.4	TTR	25.32	50.88	0.129	2.57
G4-1001.9-B	305.4	TTR	25.32	50.85	0.129	2.57
G4-1001.9-C	305.4	TTR	25.32	50.80	0.129	2.57
G4-1002.4-A	305.5	TTR	25.32	50.88	0.129	2.57
G4-1002.4-B	305.5	SNL	25.30	50.77	0.129	2.57
G4-1002.4-C	305.5	SNL	25.30	50.75	0.129	2.57
G4-1002.4-D	305.5	TTR	25.32	50.88	0.129	2.57
G4-1065.8-A	324.9	TTR	25.30	50.88	0.138	2.56
G4-1065.8-C	324.9	TTR	25.35	50.90	0.138	2.56
G4-1307.2-A	398.4	TTR	25.27	50.88	0.124	2.58
G4-1307.2-C	398.4	TTR	25.27	50.88	0.124	2.58
G4-1307.2-D	398.4	TTR	25.27	50.85	0.124	2.58
G4-1307.2-E	398.4	TTR	25.27	50.72	0.124	2.58
G4-1307.2-F	398.4	TTR	25.27	50.88	0.124	2.58
G4-1369.1-A	417.3	TTR	25.27	50.83	0.381	2.41
G4-1369.1-B	417.3	TTR	25.27	50.77	0.381	2.41
G4-1369.1-C	417.3	TTR	25.30	50.77	0.381	2.41
G4-1369.1-D	417.3	TTR	25.27	50.83	0.381	2.41
G4-1369.1-E	417.3	TTR	25.27	50.80	0.381	2.41
G4-1369.1-F	417.3	TTR	25.30	50.88	0.381	2.41
G4-1369.1-G	417.3	TTR	25.25	50.80	0.381	2.41
G4-1369.1-H	417.3	TTR	25.27	50.80	0.381	2.41
G4-1400.6-A	426.9	TTR	25.30	50.90	0.352	2.35
G4-1400.6-C	426.9	TTR	25.32	50.85	0.352	2.35
G4-1400.6-D	426.9	TTR	25.32	50.83	0.352	2.35
G4-1400.6-E	426.9	TTR	25.30	50.83	0.352	2.35
G4-1400.6-F	426.9	TTR	25.32	50.83	0.352	2.35
G4-1400.6-G	426.9	TTR	25.32	50.88	0.352	2.35
G4-1400.6-H	426.9	TTR	25.32	50.85	0.352	2.35

* These data were derived from Nimick, Price, and Schwartz (in preparation) and Bish and Vaniman (in preparation).

Table 7a.
Brief Sample Descriptions

Sample ID	Description* Color, Welding, Fabric, F-L-P, Comments
G4-686.6-A	Pv,D,i
G4-686.6-B	lB,D,i,1eF
G4-686.6-C	lB,D,i,2 possible pretest fractures(0°)
G4-686.6-D	lB,D,i
G4-686.6-E	lB,D,i75°
G4-686.6-F	lB,D,i
G4-686.6-G	lB,D,i
G4-742.75-A	dB,D,i,1eP
G4-742.75-B	dB,D,i,1 pretest fracture(90°)
G4-742.75-C	dB,D,i90°,3eP
G4-742.75-D	dB,D,i,mP
G4-742.75-E	lB,D,d75°
G4-742.75-F	lB,D,i
G4-742.75-G	lB,D,i,2eP
G4-742.75-H	lB,D,i
G4-748.6-A	lB,D,i,5F
G4-748.6-B	lB,D,i,4F
G4-749.0-A	lB,D,i
G4-749.0-B	lB,D,i,2eF
G4-910.7-A	lBPu,D,i,mF,oP,1 healed pretest fracture(90°)
G4-911.3-A	lB,D,i
G4-911.3-B	dB,D,i,1 possible pretest fracture on one end
G4-911.3-C	lB,D,i,1eF
G4-965.2-A	lB,D,i
G4-965.2-B	lB,D,i,1eF,2foL
G4-965.2-D	lB,D,i,1foL
G4-965.2-E	lBPu,D,i,1eF
G4-965.2-H	lBPu,D,i,3foL

* See Table 7b for a key to the symbols used.

Table 7a.
Brief Sample Descriptions (concluded)

Sample ID	Description* Color, Welding, Fabric, F-L-P, Comments
G4-1001.9-A	lB,D,1eF,1 pretest fracture across one end
G4-1001.9-B	PuB,D,i,1 pretest fracture(90°),1 healed pretest fracture (0°)
G4-1001.9-C	PuB,D,i,1 healed pretest fracture (70°)
G4-1002.4-A	lBPu,D,i80°,2-3F
G4-1002.4-B	lB,D,i75°,1eF,1eP
G4-1002.4-C	Pu,D,i80°,1eF,1eP
G4-1002.4-D	lBPu,D,i70°,1F
G4-1065.8-A	Pu,D,i,apparent porosity increases along axis
G4-1065.8-C	lBPu,D,i,1F,1 healed pretest fracture
G4-1307.2-A	BlB,D,i,mF,many clay patches in vitric matrix
G4-1307.2-C	BlB,M,i,1F,large clay patches in vitric matrix
G4-1307.2-D	BlB,M,i,1 pretest clay-lined fracture, other clay patches
G4-1307.2-E	BlB,D,i,1eF,large clay patches in vitric matrix
G4-1307.2-F	BlB,M,i,1eF,common small clay patches
G4-1369.1-A	BlB,Pa,i,2-3F,porous,several clay patches
G4-1369.1-B	BlB,Pa,i,2eP,one large clay patch at one end
G4-1369.1-C	BlB,Pa,i,porous
G4-1369.1-D	BlB,Pa,i,large clay patches at each end
G4-1369.1-E	BlB,Pa,i,one large clay patch at one end
G4-1369.1-F	BlB,Pa,i,clay patches at both ends
G4-1369.1-G	BlB,Pa,i,2F(1e),porous,several clay patches
G4-1369.1-H	BlB,Pa,i,mF,porous,several clay patches
G4-1400.6-A	lGPi,N,i,porous,1 healed pretest fracture
G4-1400.6-C	lGPi,N,i,porous
G4-1400.6-D	lGPi,N,i,1oF,porous
G4-1400.6-E	lGPi,N,i,porous
G4-1400.6-F	lGPi,N,i,porous
G4-1400.6-G	lGPi,N,i,porous
G4-1400.6-H	lGPi,N,i,porous,several possible pretest fractures

* See Table 7b for a key to the symbols used.

Table 7b.
Brief Sample Descriptions - Symbols Key

Section	Symbol	Definition
Color		Sample Color
	l	light
	d	dark
	Pu	Purple
	Pi	Pink
	G	Gray
	B	Brown
	Bl	Black
Welding		Degree of sample welding
	D	Densely
	M	Moderately
	Pa	Partially
	N	Nonwelded or bedded
Fabric		Preferred orientation of sample fabric
	d	distinct
	i	indistinct
	( )	orientation relative to sample axis
F-L-P		Lithic fragments (F), Lithophysae (L), Pumice fragments (P)
	m	many(>10)
	e	intersecting end of sample
	o	open void space
	f	flattened

Table 8.
Summary Test Results

Sample ID	Lab	P_c (MPa)	$\dot{\epsilon}$ (s^{-1})	E (GPa)	ν	$(\Delta\sigma)_u$ (MPa)	$(\epsilon_1)_u$ (milli)
G4-686.6-A	TTR	0.1	10^{-5}	36.2	0.18	270	8.7
G4-686.6-B	TTR	5	10^{-5}	40.5	0.16	156	13.3
G4-686.6-C	TTR	10	10^{-5}	38.0	0.23	344	10.8
G4-686.6-D	TTR	0.1	10^{-5}	40.7	0.17	326	10.0
G4-686.6-E	TTR	5	10^{-5}	43.6	0.30	87	1.8
G4-686.6-F	TTR	10	10^{-5}	35.0	0.25	360	11.8
G4-686.6-G	TTR	0.1	10^{-5}	33.1	0.21	180	6.4
G4-742.75-A	TTR	0.1	10^{-3}	37.4	0.29	319	9.5
G4-742.75-B	TTR	0.1	10^{-3}	34.0	0.28	283	9.4
G4-742.75-C	TTR	0.1	10^{-3}	38.4	0.25	280	8.9
G4-742.75-D	TTR	0.1	10^{-7}	37.5	0.20	243	6.9
G4-742.75-E	TTR	0.1	10^{-5}	35.6	0.21	235	7.2
G4-742.75-F	TTR	0.1	10^{-5}	36.8	0.21	256	8.3
G4-742.75-G	TTR	0.1	10^{-5}	34.6	0.21	279	9.3
G4-742.75-H	TTR	0.1	10^{-7}	33.6	0.11	230	7.5
G4-748.6-A	TTR	0.1	10^{-5}	32.2	0.16	196	6.6
G4-748.6-B	TTR	0.1	10^{-5}	32.3	0.21	190	7.0
G4-749.0-A	SNL	0.1	10^{-5}	33.5	0.29	268	8.7
G4-749.0-B	SNL	0.1	10^{-5}	34.1	0.27	188	6.7
G4-910.7-A	TTR	0.1	10^{-5}	30.1	0.18	131	5.5
G4-911.3-A	SNL	0.1	10^{-5}	37.6	0.36	160	4.8
G4-911.3-B	TTR	0.1	10^{-5}	24.8	0.15	88	4.8
G4-911.3-C	TTR	0.1	10^{-5}	26.0	0.19	118	5.1
G4-965.2-A	TTR	0.1	10^{-5}	38.0	0.21	187	5.6
G4-965.2-B	TTR	10	10^{-5}	14.1	0.21	97	11.0
G4-965.2-D	TTR	0.1	10^{-5}	31.1	0.18	131	4.4
G4-965.2-E	TTR	10	10^{-5}	32.7	0.28	247	9.6
G4-965.2-H	TTR	0.1	10^{-5}	33.1	0.19	148	6.0

Table 8.
Summary Test Results (concluded)

Sample ID	Lab	P_e (MPa)	$\dot{\epsilon}$ (s^{-1})	E (GPa)	ν	$(\Delta\sigma)_u$ (MPa)	$(\epsilon_1)_u$ (milli)
G4-1001.9-A	TTR	0.1	10^{-5}	22.8	0.19	99	5.1
G4-1001.9-B	TTR	0.1	10^{-5}	32.7	0.20	170	
G4-1001.9-C	TTR	0.1	10^{-5}	31.8	0.18	147	4.8
G4-1002.4-A	TTR	0.1	10^{-7}	22.0	0.11	123	4.4
G4-1002.4-B	SNL	0.1	10^{-5}	33.6	0.32	179	5.6
G4-1002.4-C	SNL	0.1	10^{-5}	31.1	-	137	4.5
G4-1002.4-D	TTR	0.1	10^{-7}	32.8	0.20	138	4.5
G4-1065.8-A	TTR	0.1	10^{-5}	2.44	-	12	18.5
G4-1065.8-C	TTR	0.1	10^{-5}	26.7	0.21	124	4.3
G4-1307.2-A	TTR	0.1	10^{-5}	30.2	0.23	104	5.3
G4-1307.2-C	TTR	0.1	10^{-5}	22.8	0.20	79	3.3
G4-1307.2-D	TTR	0.1	10^{-5}	20.0	0.30	31	1.9
G4-1307.2-E	TTR	0.1	10^{-5}	16.6	0.24	65	7.2
G4-1307.2-F	TTR	0.1	10^{-5}	34.9	0.20	98	3.3
G4-1369.1-A	TTR	0.1	10^{-3}	2.96	0.26	13	7.0
G4-1369.1-B	TTR	0.1	10^{-3}	1.76	0.16	8	6.0
G4-1369.1-C	TTR	0.1	10^{-3}	3.37	0.12	15	6.8
G4-1369.1-D	TTR	0.1	10^{-7}	1.41	0.17	8	5.5
G4-1369.1-E	TTR	0.1	10^{-5}	2.21	0.21	11	7.3
G4-1369.1-F	TTR	0.1	10^{-5}	3.70	0.14	14	6.4
G4-1369.1-G	TTR	0.1	10^{-5}	1.53	0.19	6	6.5
G4-1369.1-H	TTR	0.1	10^{-7}	3.10	0.17	12	6.3
G4-1400.6-A	TTR	-	-	-	-	-	-
G4-1400.6-C	TTR	5	10^{-5}	3.10	0.21	17	19.8
G4-1400.6-D	TTR	10	10^{-5}	3.14	0.30	16	20.0
G4-1400.6-E	TTR	0.1	10^{-5}	2.32	0.18	19	7.2
G4-1400.6-F	TTR	5	10^{-5}	3.68	0.20	29	12.0
G4-1400.6-G	TTR	10	10^{-5}	4.35	0.30	32	16.0
G4-1400.6-H	TTR	0.1	10^{-5}	2.25	0.18	14	6.1

Table 9.
Ranges of Mechanical Property Data

Lithology*	# Samples	$P_c/\dot{\epsilon}$ (Mpa/s^{-1})	E (GPa)	ν	$(\Delta\sigma)_u$ (MPa)	$(\epsilon_1)_u$ (milli)
D, dV	3	$0.1/10^{-3}$	34.0-38.4	0.25-0.29	280-319	8.9-9.5
D, dV	24	$0.1/10^{-5}$	2.44-40.7	0.16-0.36	12-326	4.3-18.4
D, dV	4	$0.1/10^{-7}$	22.0-37.5	0.11-0.20	123-243	4.4-7.5
D, dV	2	$5/10^{-5}$	40.5-43.6	0.16-0.30	87-156	1.8-13.3
D, dV	4	$10/10^{-5}$	14.1-38.0	0.21-0.28	97-360	9.6-11.8
M, V, C	5	$0.1/10^{-5}$	16.6-34.9	0.20-0.30	31-104	1.9-7.2
P, V, C	3	$0.1/10^{-3}$	1.76-3.37	0.12-0.26	8-15	6.0-7.0
P, V, C	3	$0.1/10^{-5}$	1.53-3.70	0.14-0.21	6-14	6.4-7.3
P, V, C	2	$0.1/10^{-7}$	1.41-3.10	0.17	8-12	5.5-6.3
N, Z	2	$0.1/10^{-5}$	2.25-2.32	0.18	14-19	6.1-7.2
N, Z	2	$5/10^{-5}$	3.10-3.68	0.20-0.21	17-29	12.0-19.8
N, Z	2	$10/10^{-5}$	3.14-4.35	0.30	16-32	16.0-20.0

* D : Densely welded
M : Moderately welded
P : Partially welded
N : Nonwelded

dV : Devitrified
V : Vitric
C : Clay alteration
Z : Zeolitized

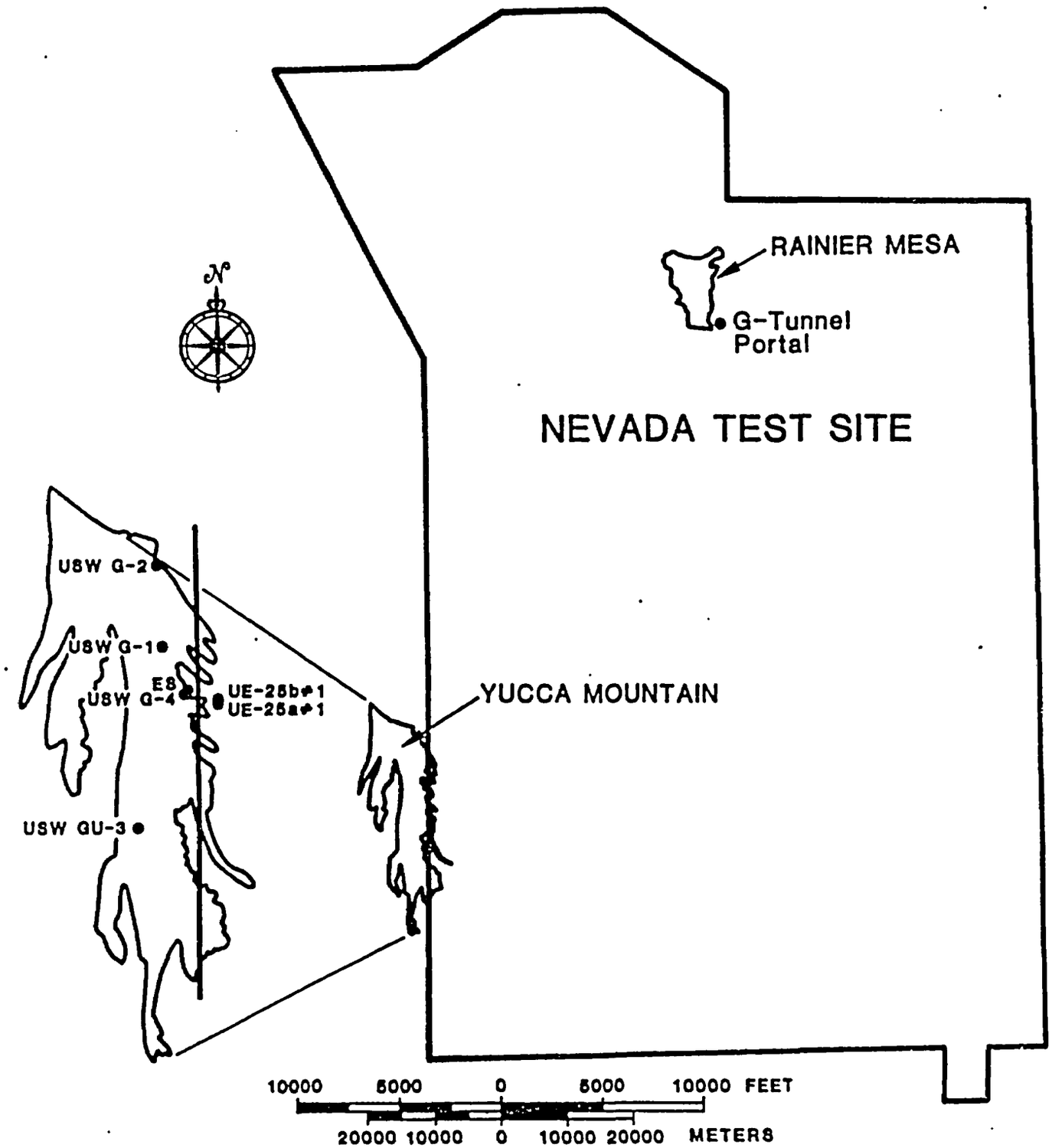

Figure 1.
Location map of the Nevada Test Site, Yucca Mountain, and Drillhole USW G-4.

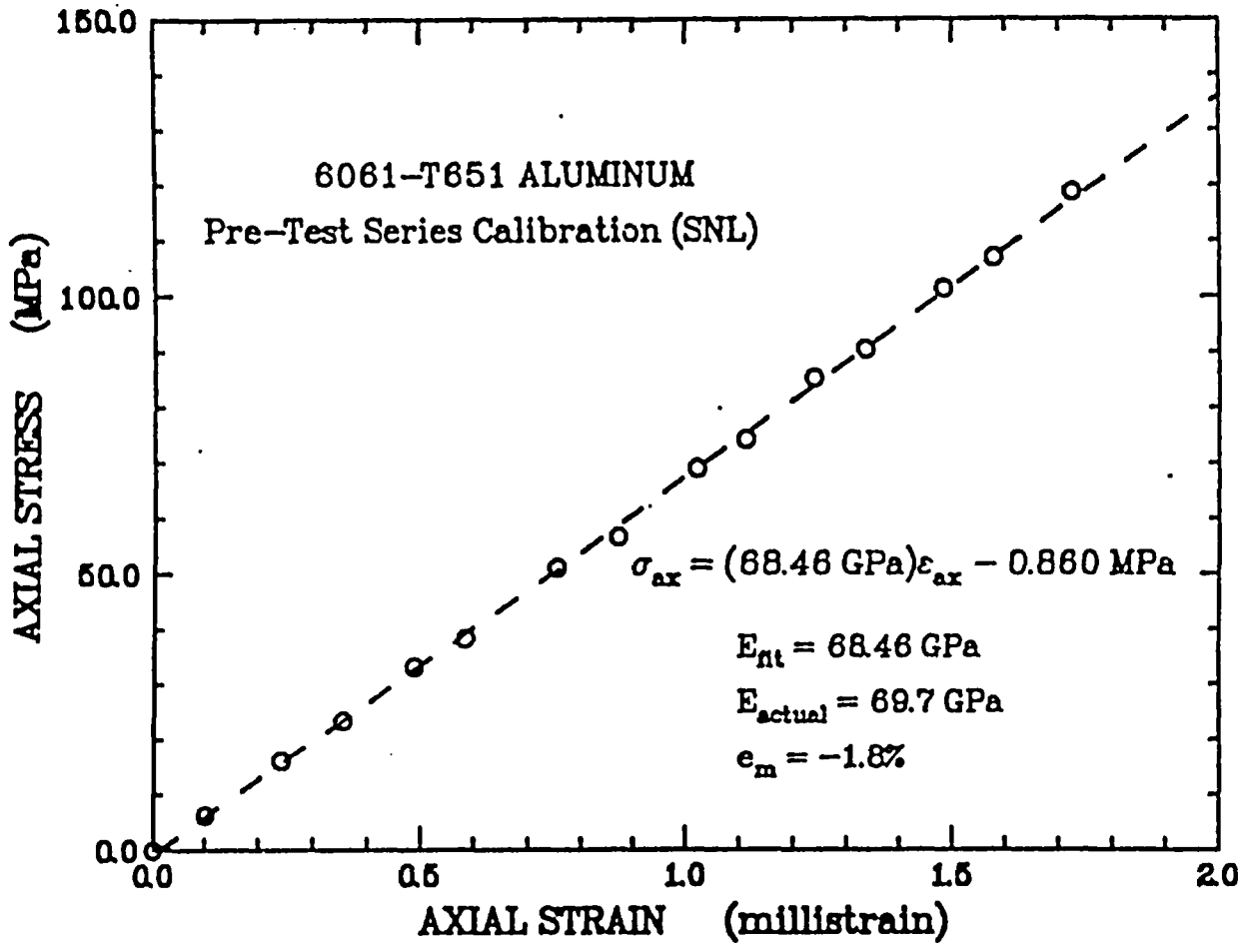

Figure 2a.

Plot of axial stress versus axial strain data with linear, least-squares fits for pre-test series system calibration at SNL with a 6061-T651 aluminum sample.

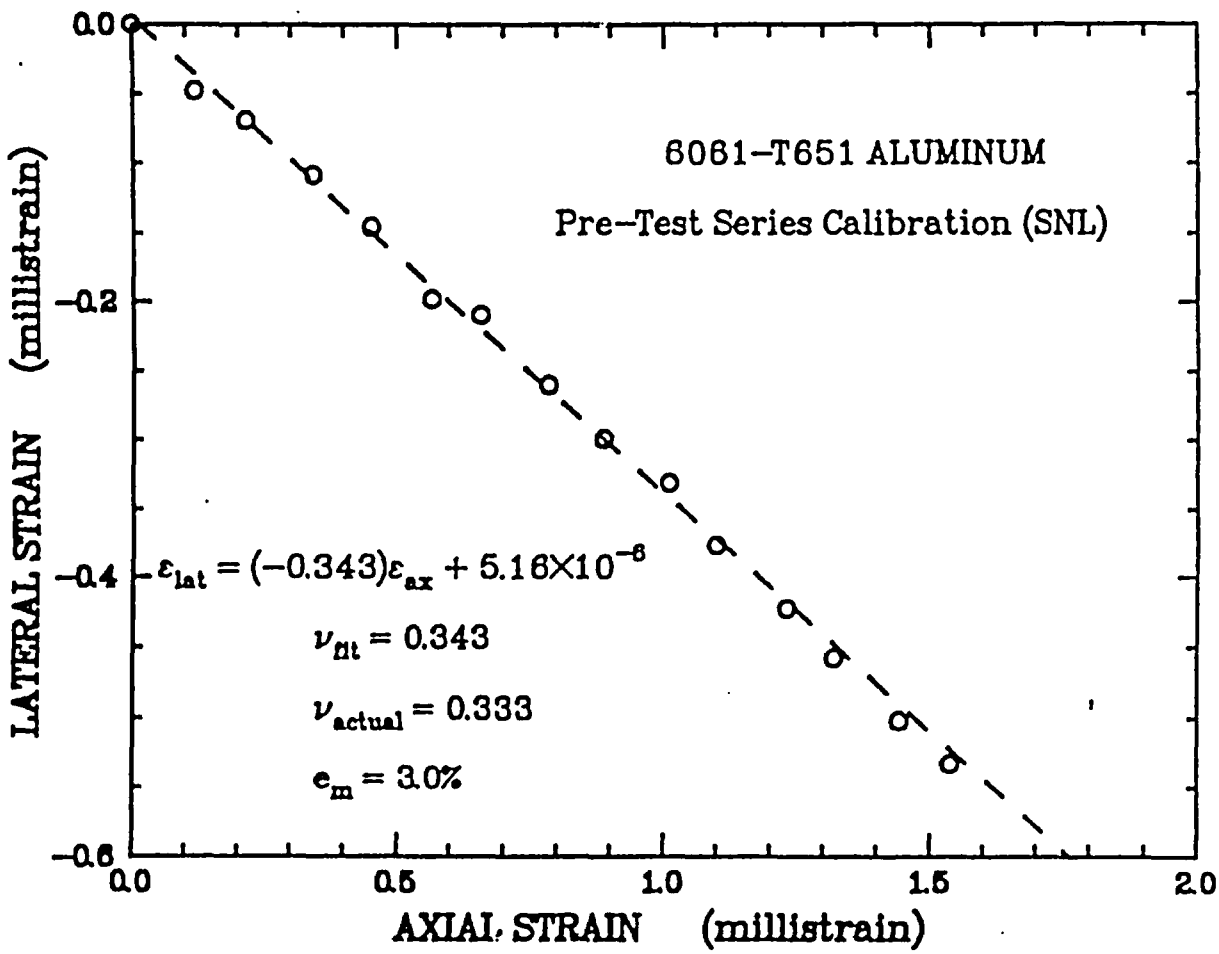

Figure 2b.

Plot of axial strain versus lateral strain data with linear, least-squares fits for pre-test series system calibration at SNL with a 6061-T651 aluminum sample.

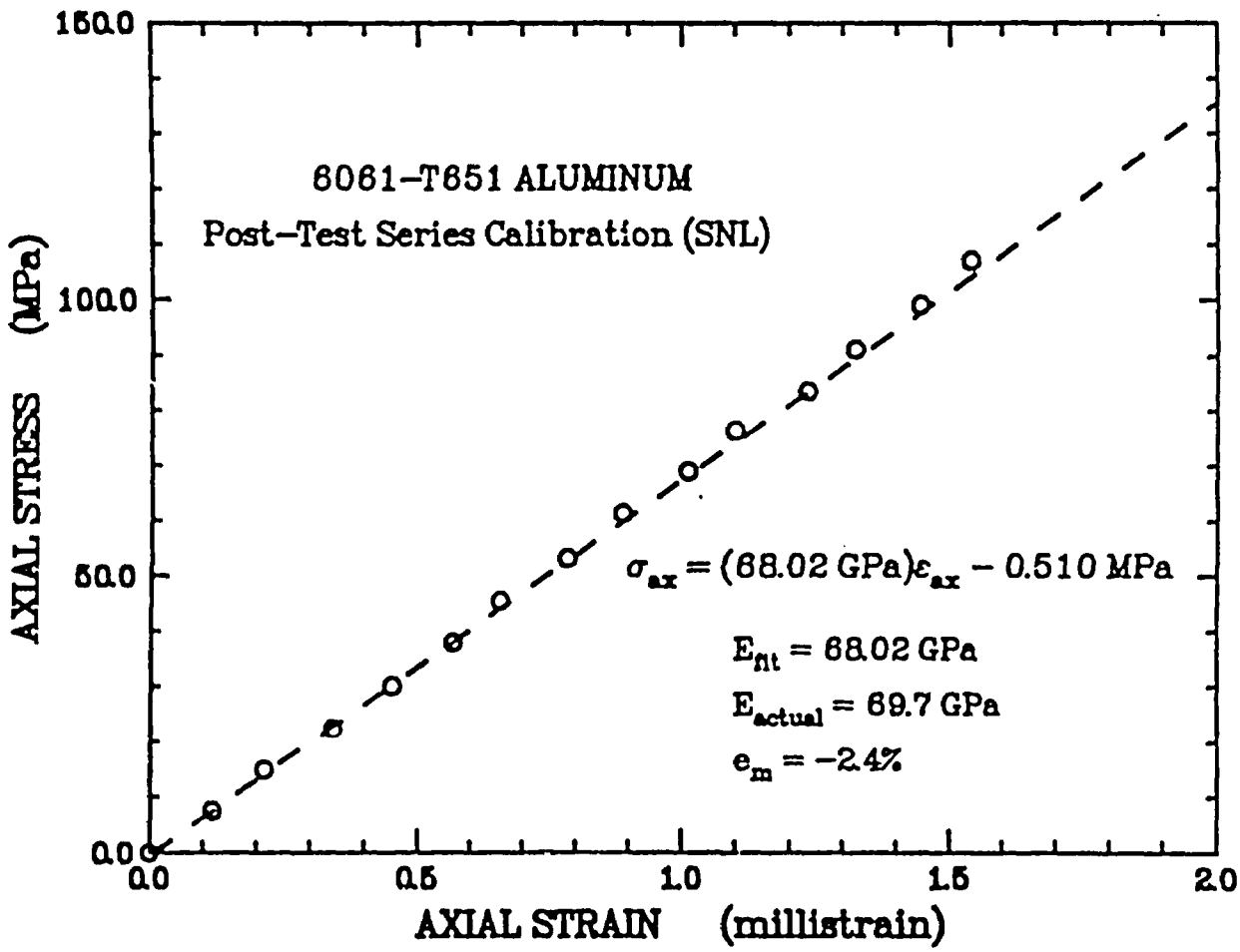

Figure 2c.

Plot of axial stress versus axial strain data with linear, least-squares fits for post-test series system calibration at SNL with a 6061-T651 aluminum sample.

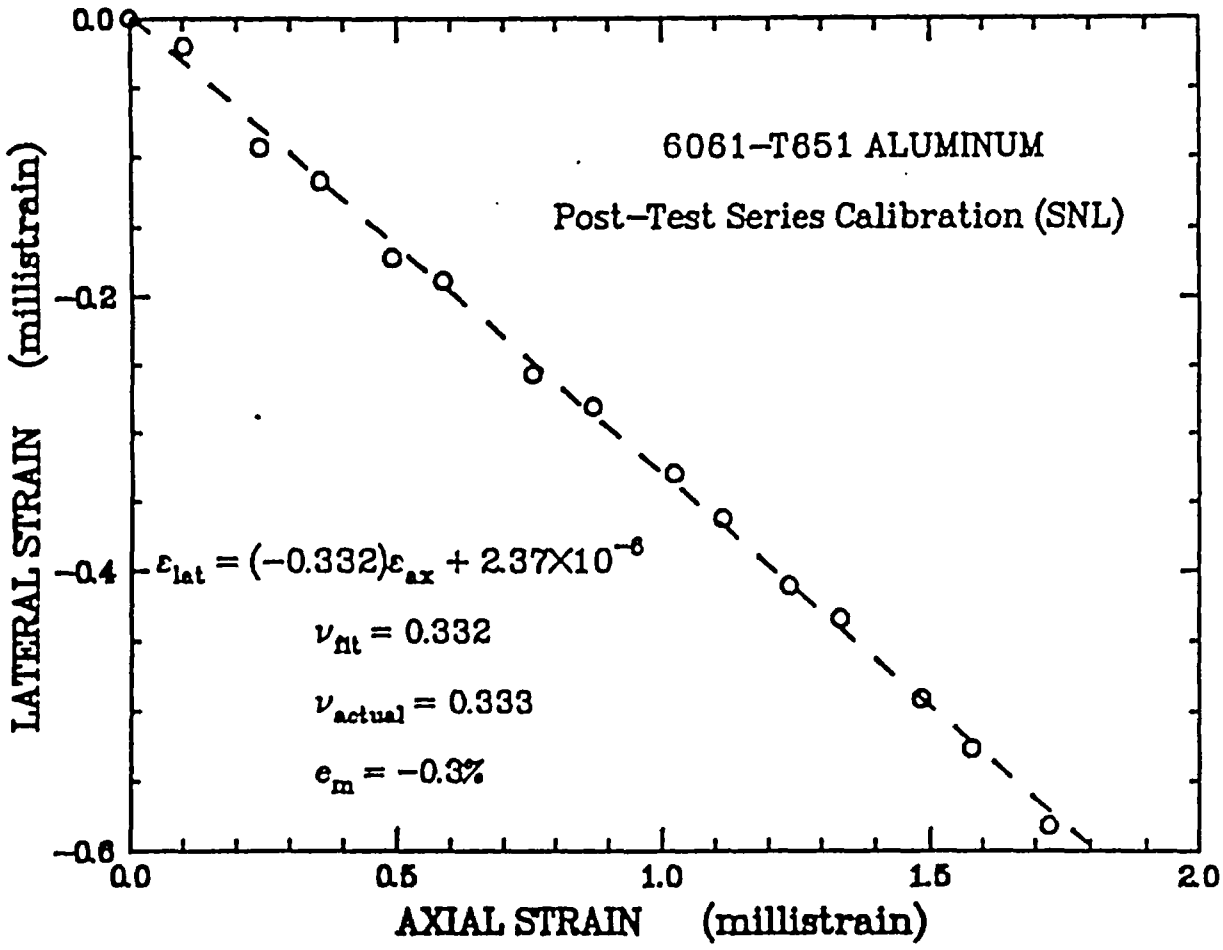

Figure 2d.

Plot of axial strain versus lateral strain data with linear, least-squares fits for post-test series system calibration at SNL with a 6061-T651 aluminum sample.

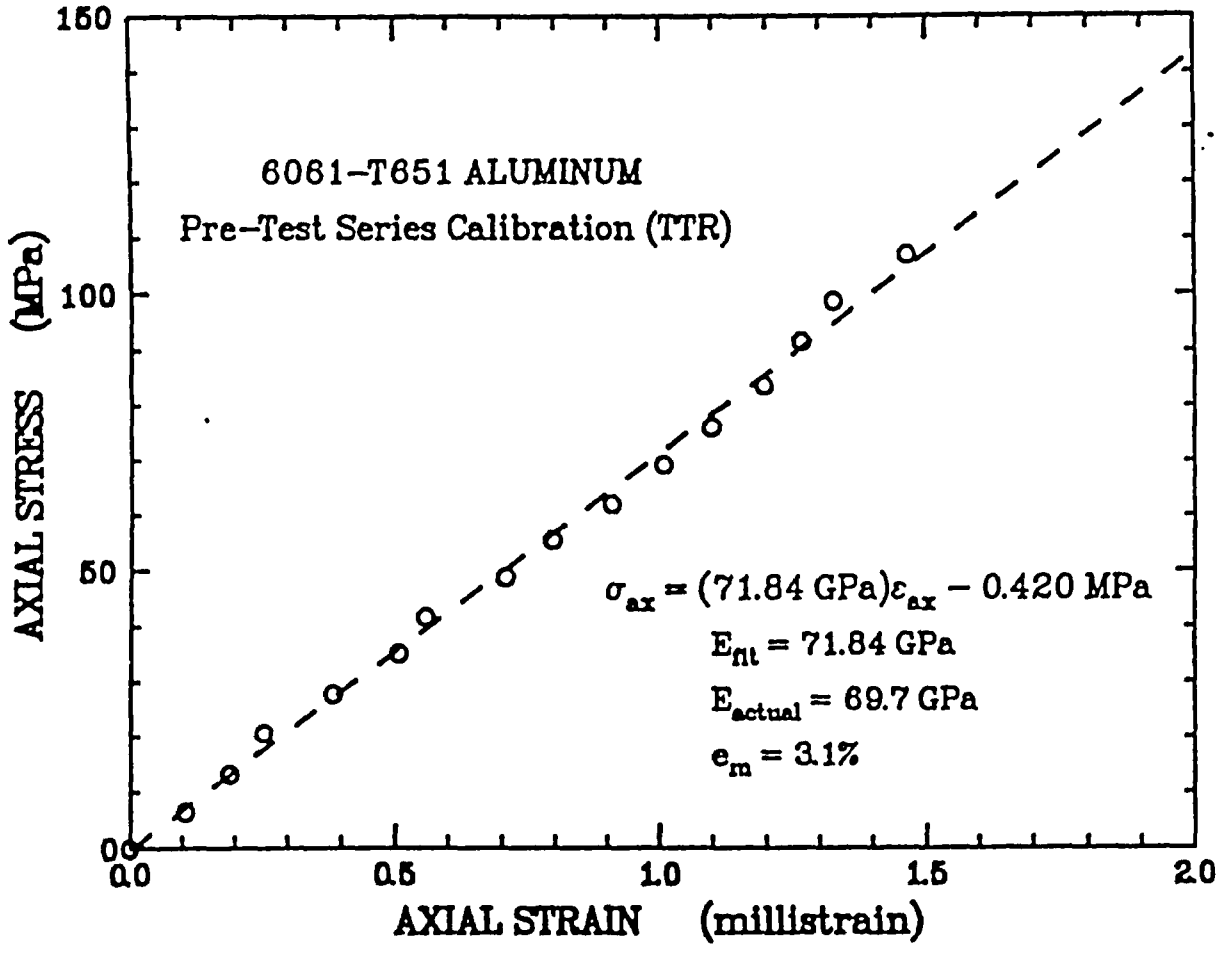

Figure 3a.

Plot of axial stress versus axial strain data with linear, least-squares fits for pre-test series system calibration at TTR with a 6061-T651 aluminum sample.

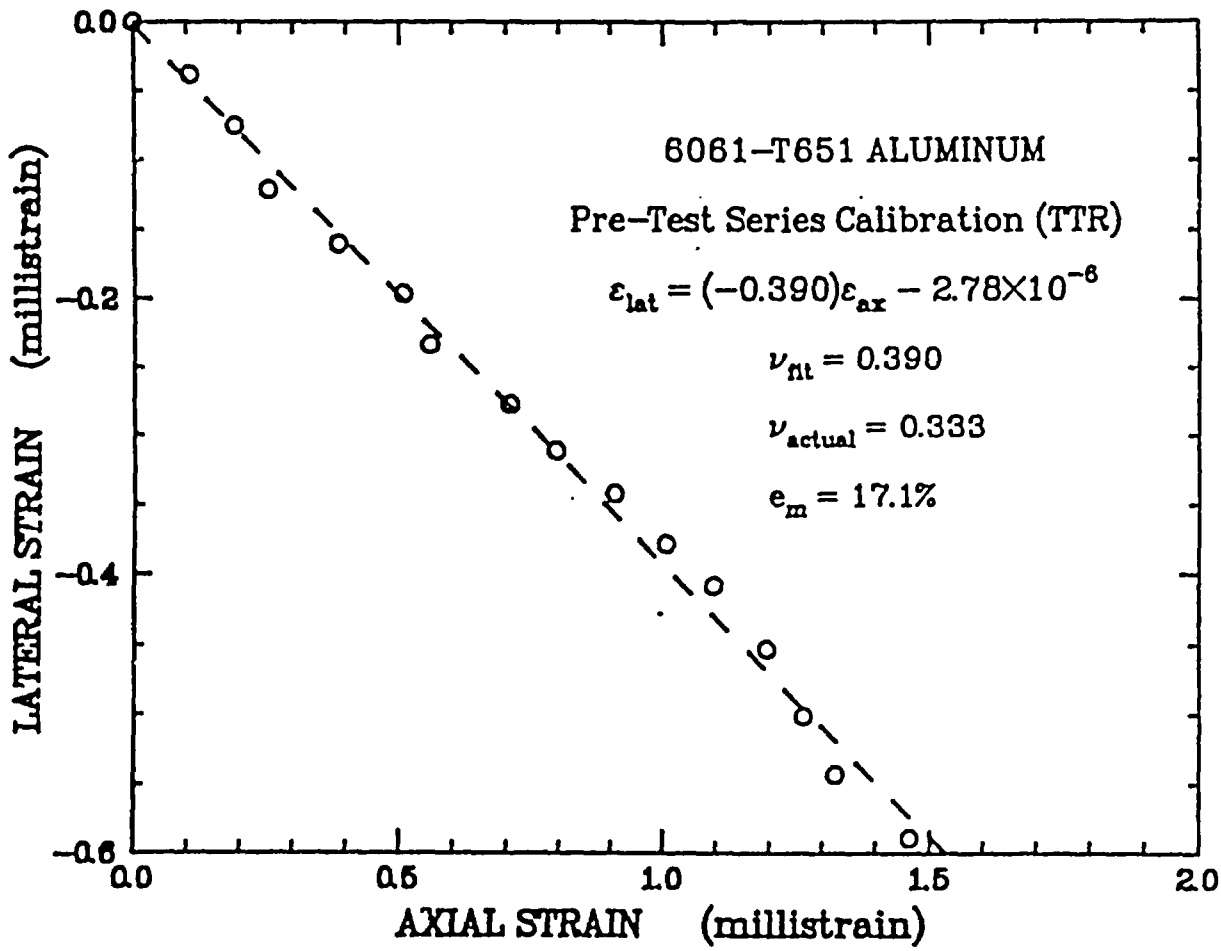

Figure 3b.

Plot of axial strain versus lateral strain data with linear, least-squares fits for pre-test series system calibration at TTR with a 6061-T651 aluminum sample.

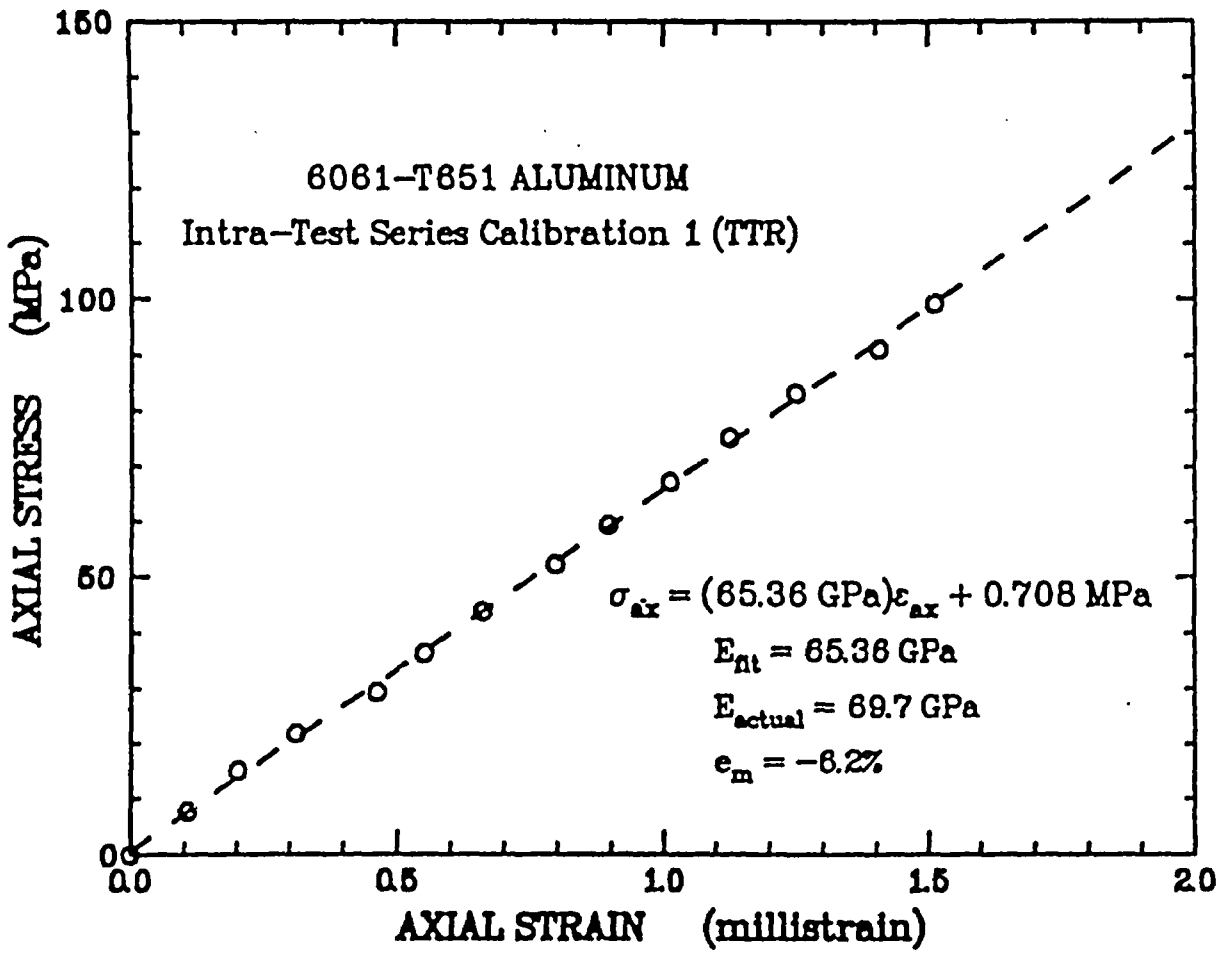

Figure 3c.

Plot of axial stress versus axial strain data with linear, least-squares fits for intra-test series 1 system calibration at TTR with a 6061-T651 aluminum sample.

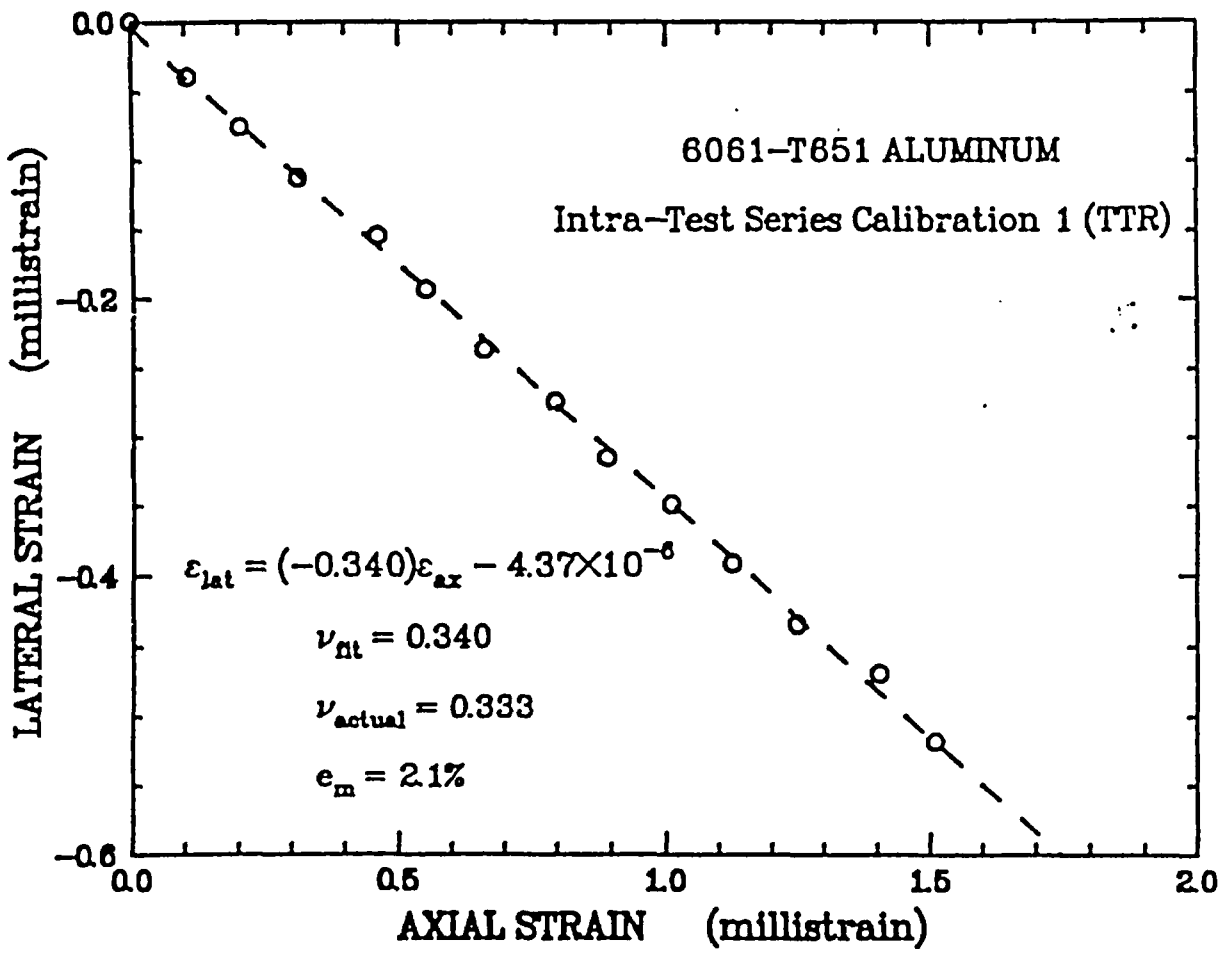

Figure 3d.

Plot of axial strain versus lateral strain data with linear, least-squares fits for intra-test series 1 system calibration at TTR with a 6061-T651 aluminum sample.

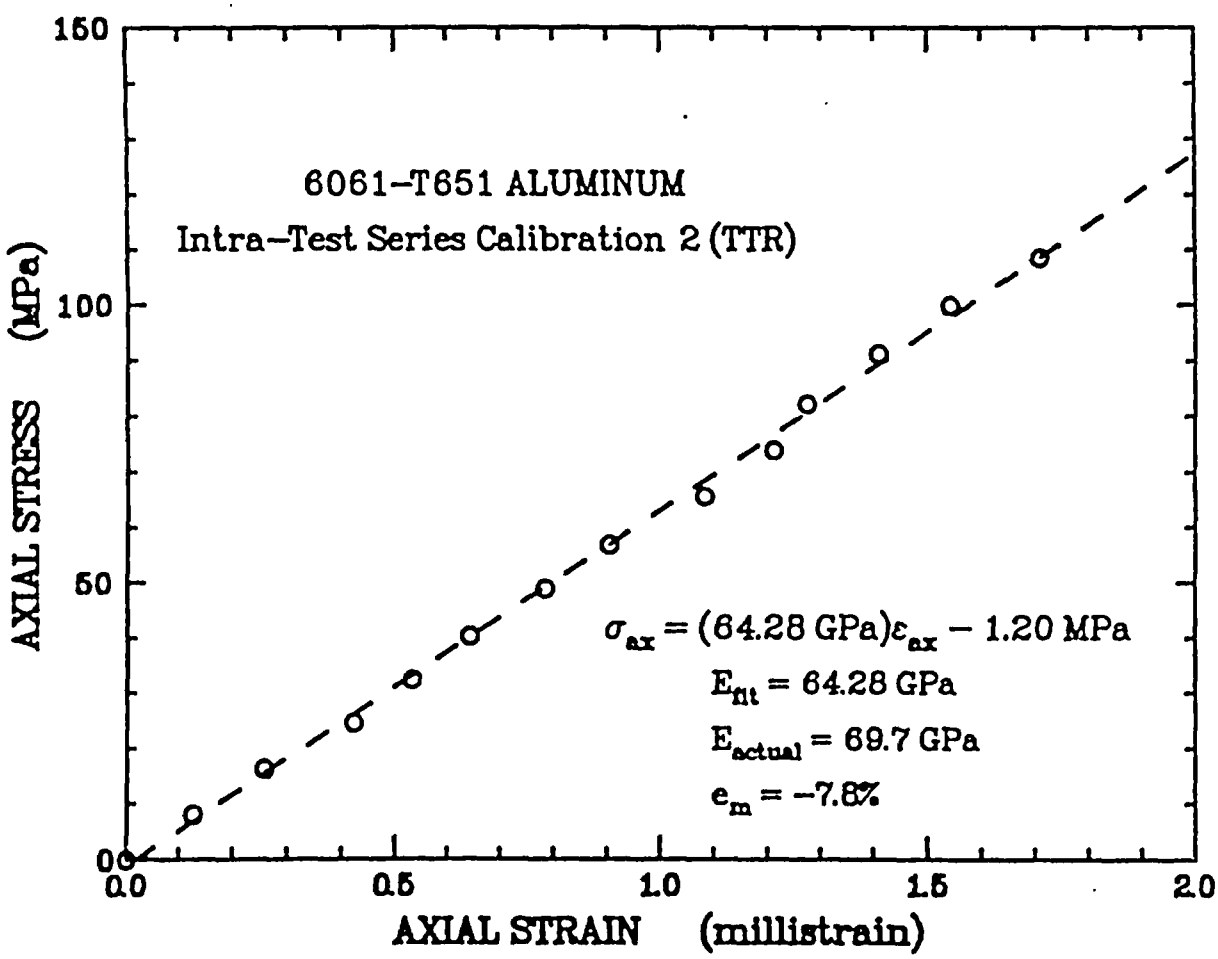

Figure 3e.

Plot of axial stress versus axial strain data with linear, least-squares fits for intra-test series 2 system calibration at TTR with a 6061-T651 aluminum sample.

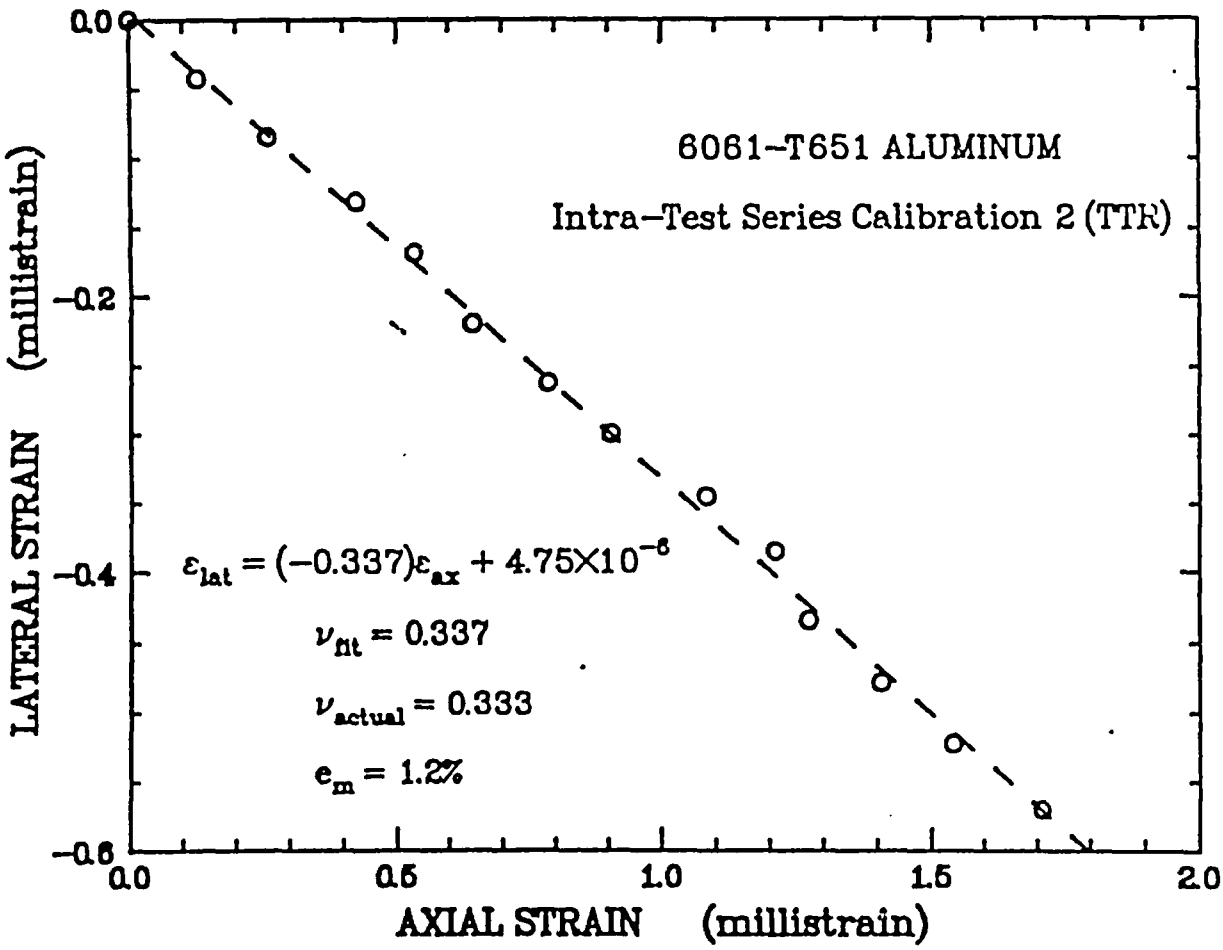

Figure 3f.

Plot of axial strain versus lateral strain data with linear, least-squares fits for intra-test series 2 system calibration at TTR with a 6061-T651 aluminum sample.

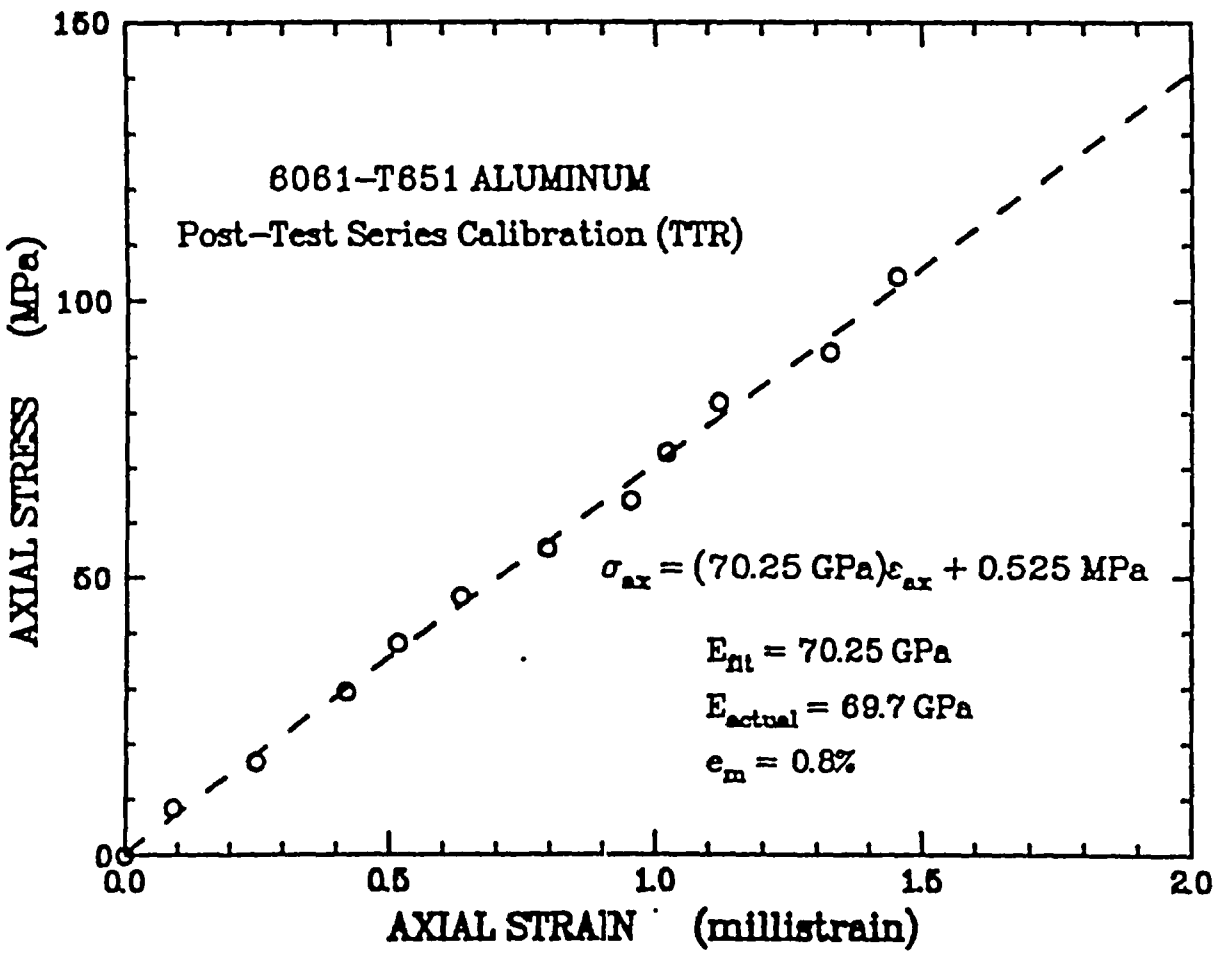

Figure 3g.

Plot of axial stress versus axial strain data with linear, least-squares fits for post-test series system calibration at TTR with a 6061-T651 aluminum sample.

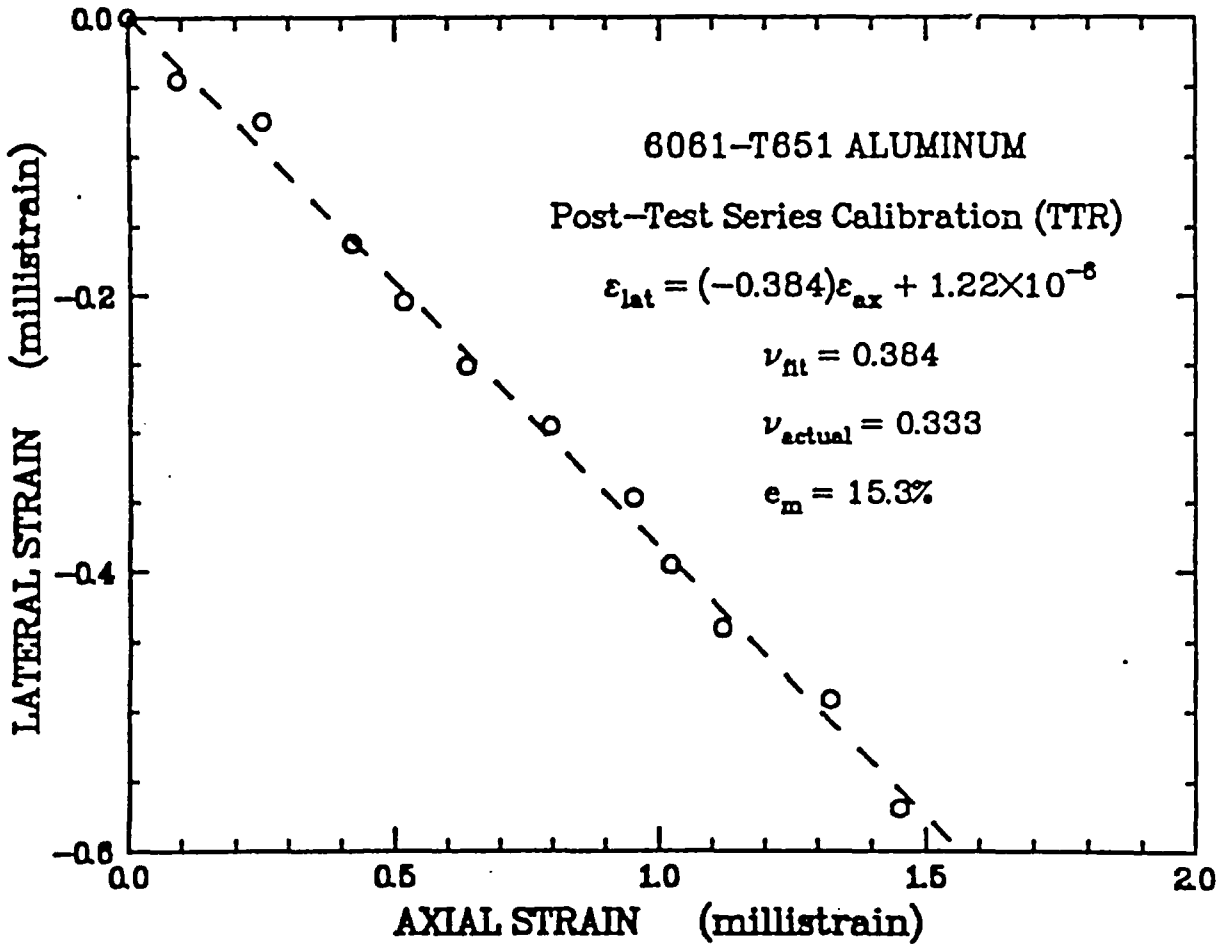

Figure 3h.

Plot of axial strain versus lateral strain data with linear, least-squares fits for post-test series system calibration at TTR with a 6061-T651 aluminum sample.

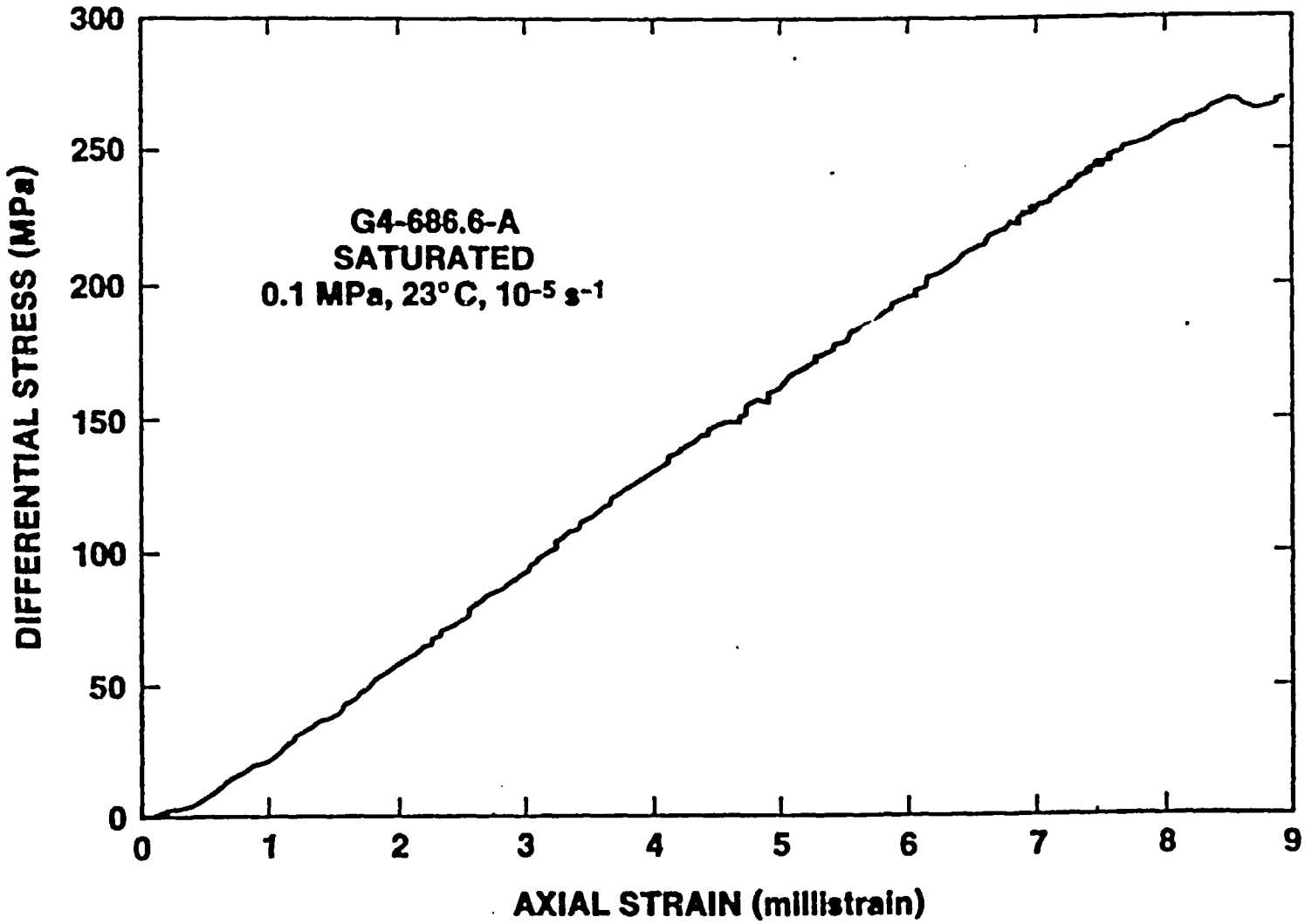

Figure 4a.

Plot of axial stress versus axial strain for sample G4-686.6-A, deformed in compression at 0.1 MPa confining pressure, room temperature, and a nominal axial strain rate of 10^{-5} s^{-1}.

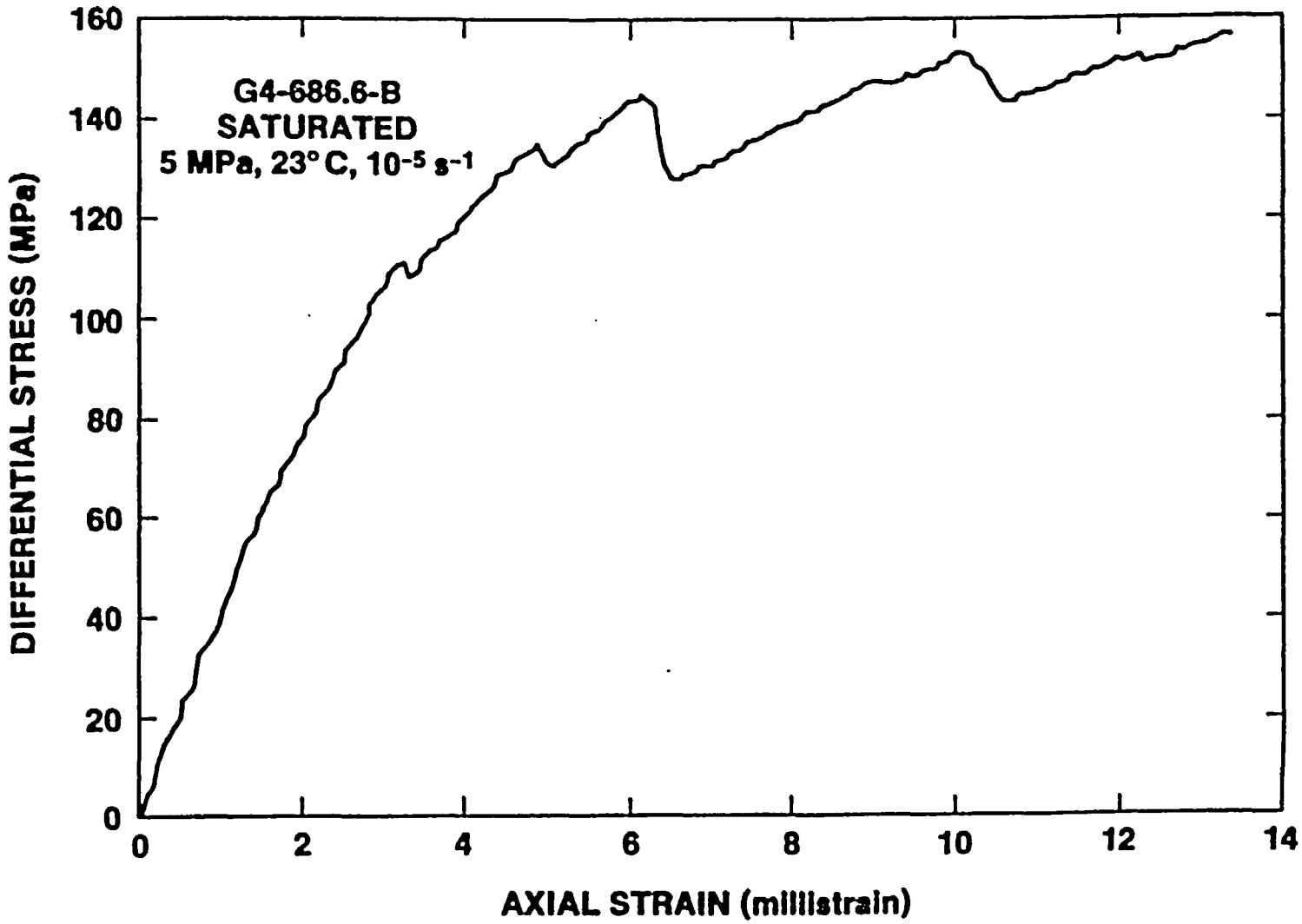

Figure 4b.

Plot of axial stress versus axial strain for sample G4-686.6-B, deformed in compression at 5 MPa confining pressure, room temperature, and a nominal axial strain rate of 10^{-5} s^{-1}.

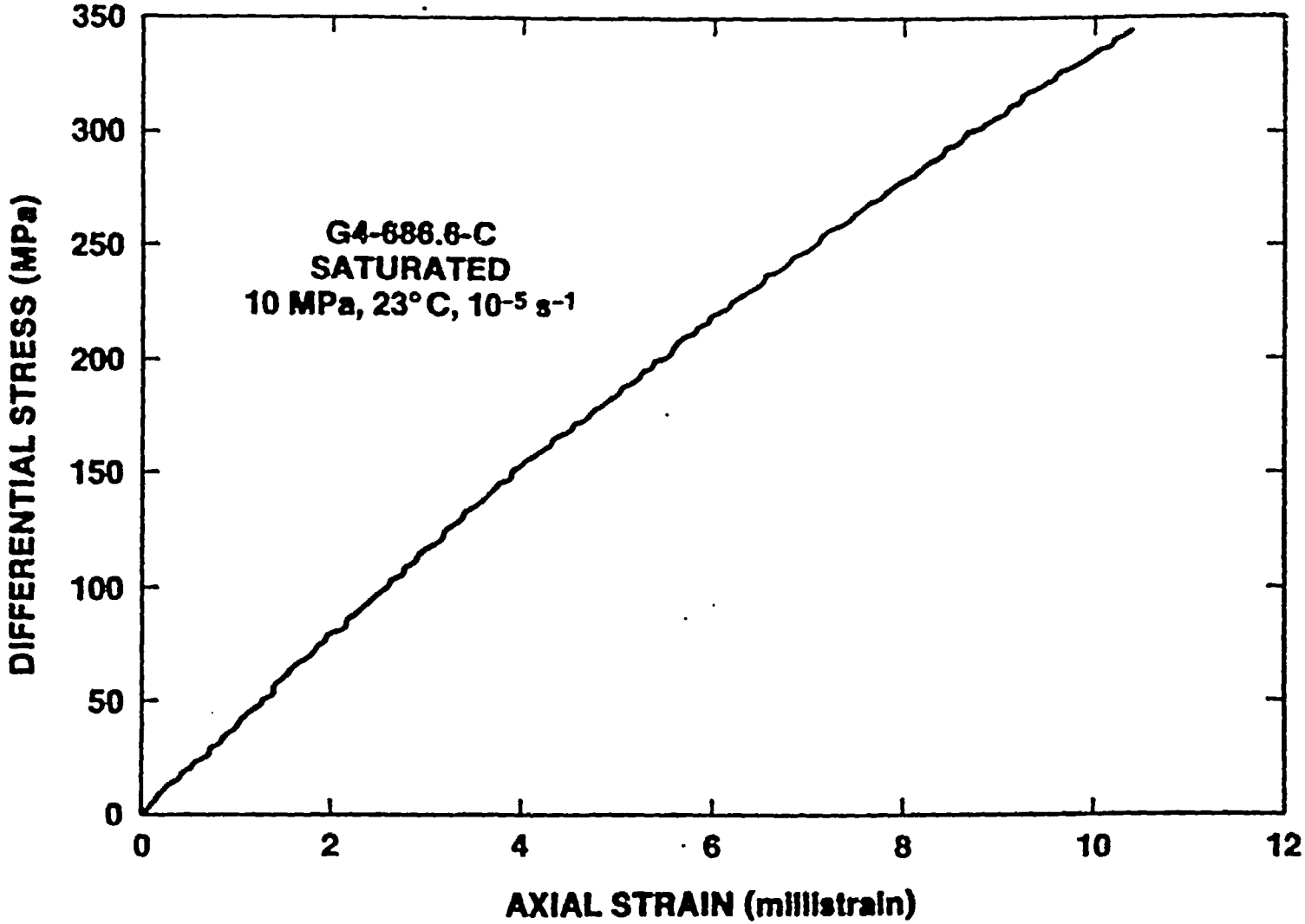

Figure 4c.

Plot of axial stress versus axial strain for sample G4-686.6-C, deformed in compression at 10 MPa confining pressure, room temperature, and a nominal axial strain rate of 10^{-5} s^{-1}.

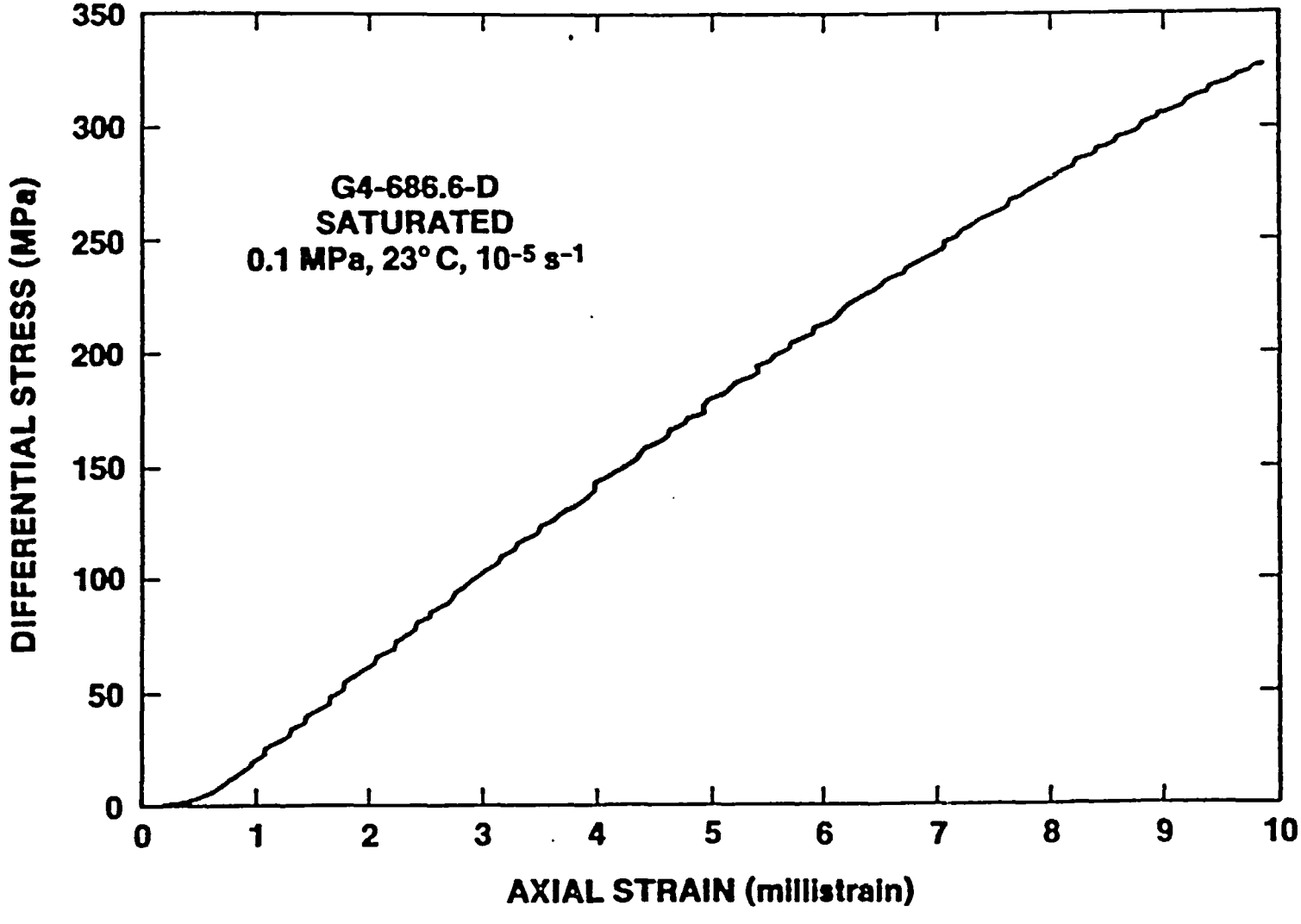

Figure 4d.

Plot of axial stress versus axial strai: for sample G4-686.6-D, deformed in compression at 0.1 MPa confining pressure, room temperature, and a nominal axial strain rate of 10^{-5} s^{-1}.

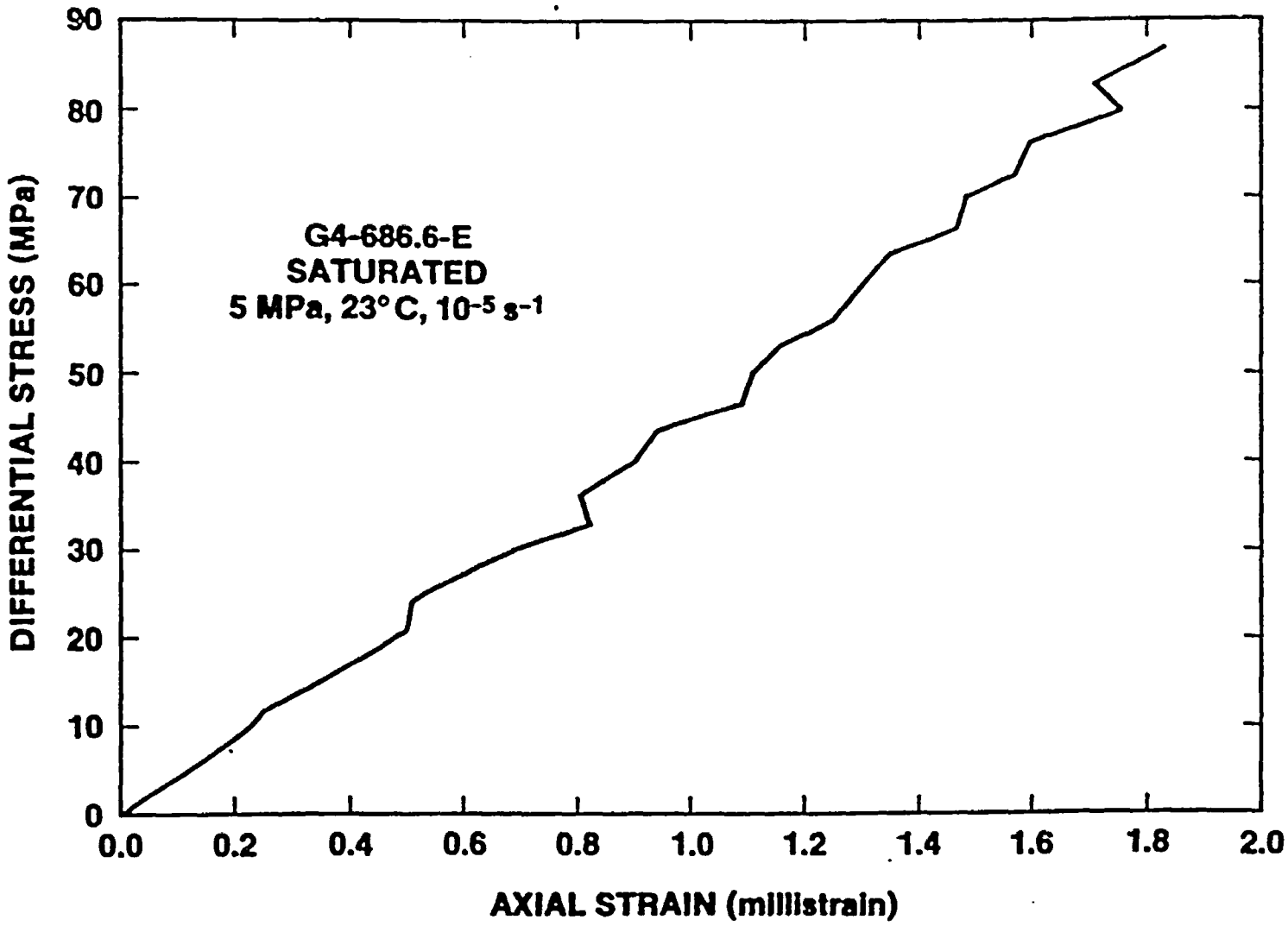

Figure 4e.

Plot of axial stress versus axial strain for sample G4-686.6-E, deformed in compression at 5 MPa confining pressure, room temperature, and a nominal axial strain rate of 10^{-5} s^{-1}.

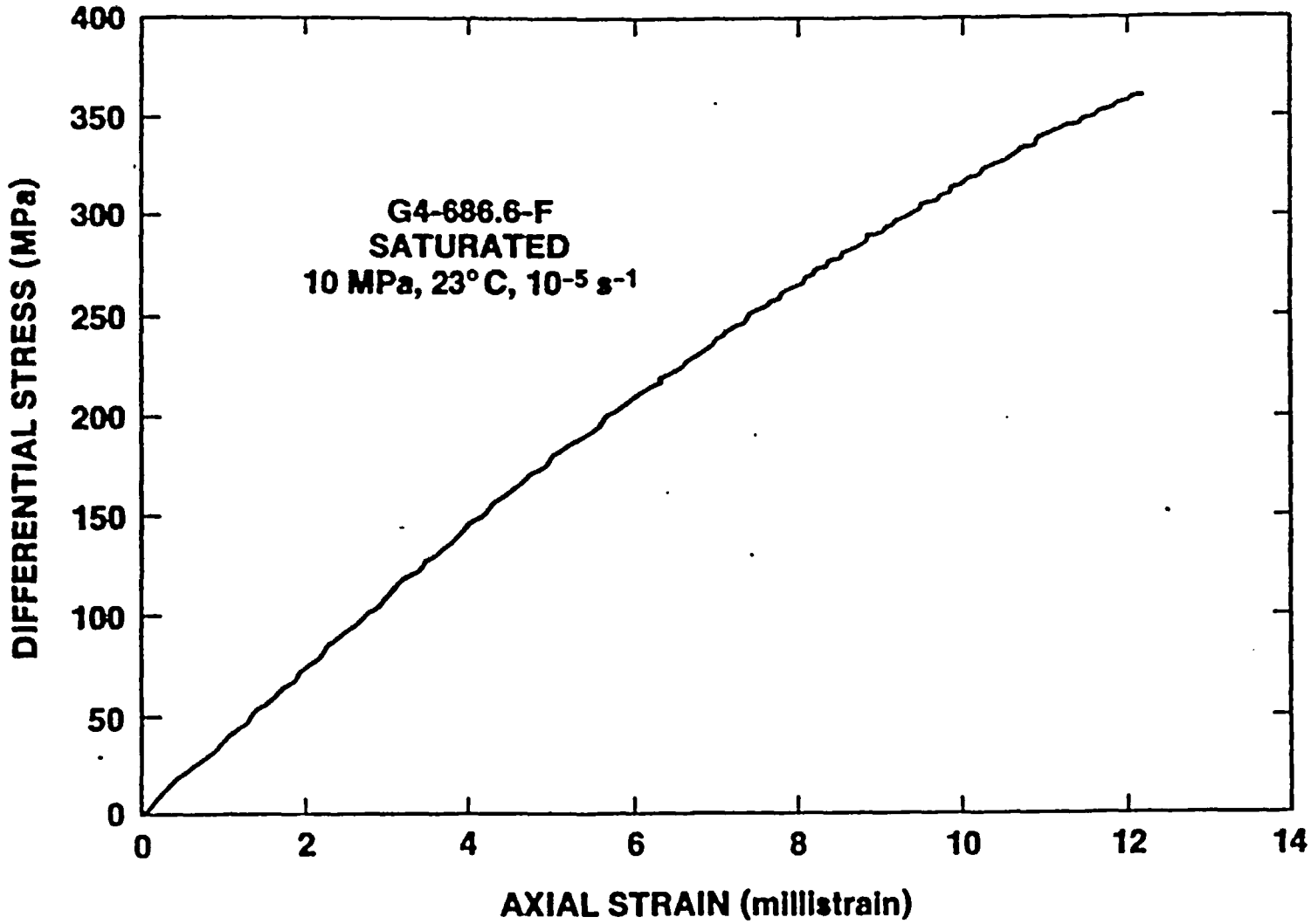

Figure 4f.

Plot of axial stress versus axial strain for sample G4-686.6-F, deformed in compression at 10 MPa confining pressure, room temperature, and a nominal axial strain rate of 10^{-5} s^{-1}.

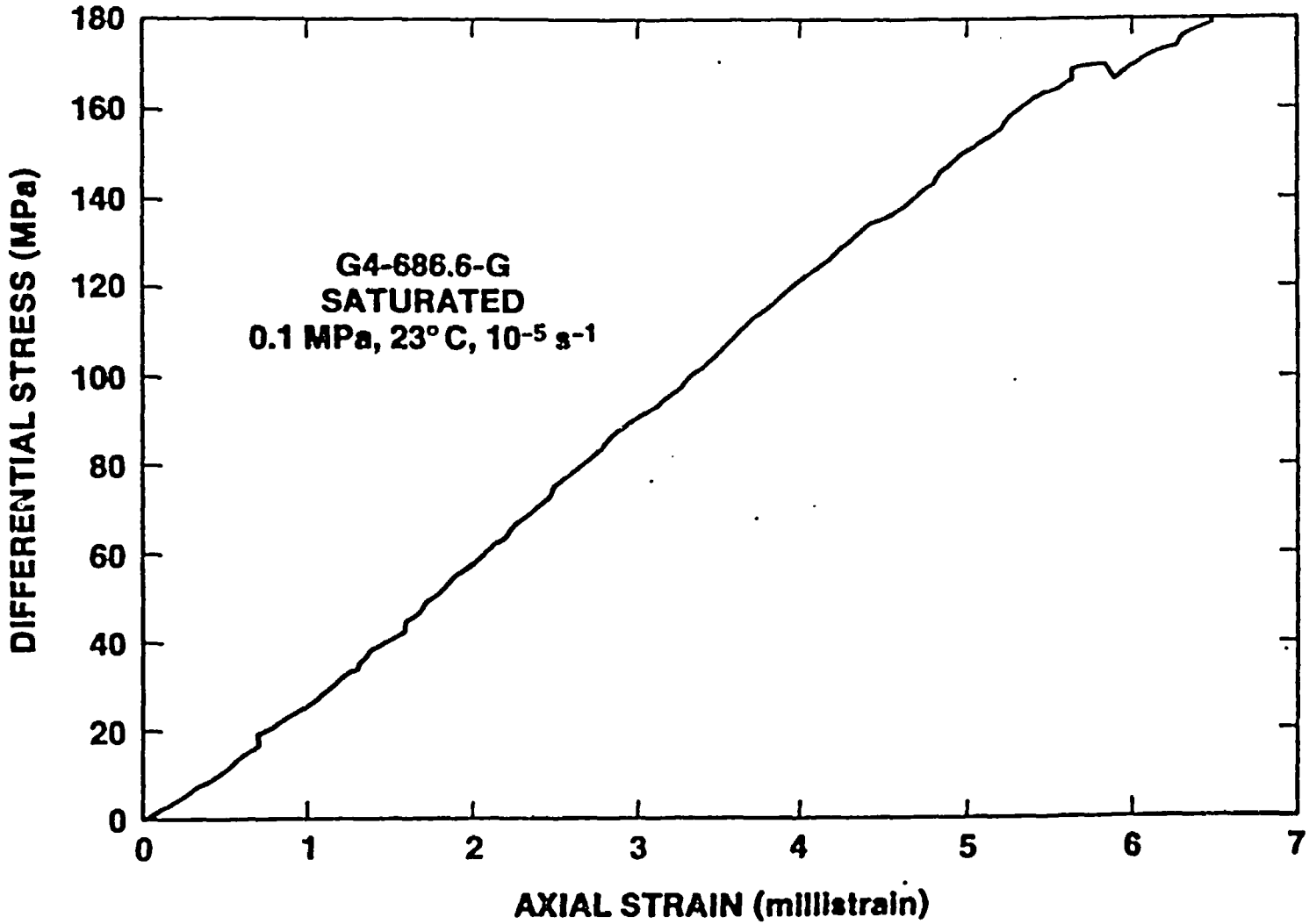

Figure 4g.

Plot of axial stress versus axial strain for sample G4-686.6-G, deformed in compression at 0.1 MPa confining pressure, room temperature, and a nominal axial strain rate of 10^{-5} s^{-1}.

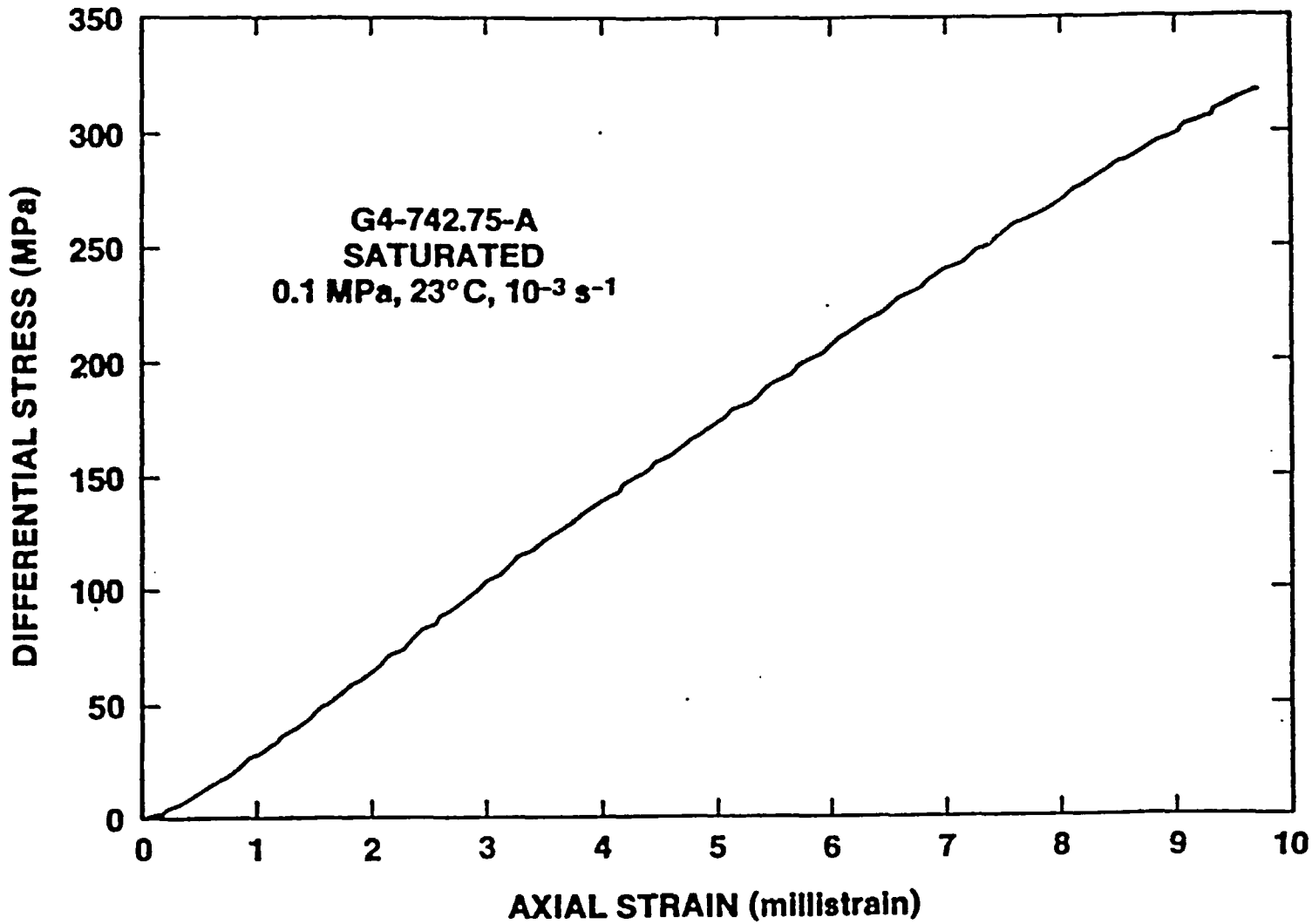

Figure 4h.

Plot of axial stress versus axial strain for sample G4-742.75-A, deformed in compression at 0.1 MPa confining pressure, room temperature, and a nominal axial strain rate of 10^{-3} s^{-1}.

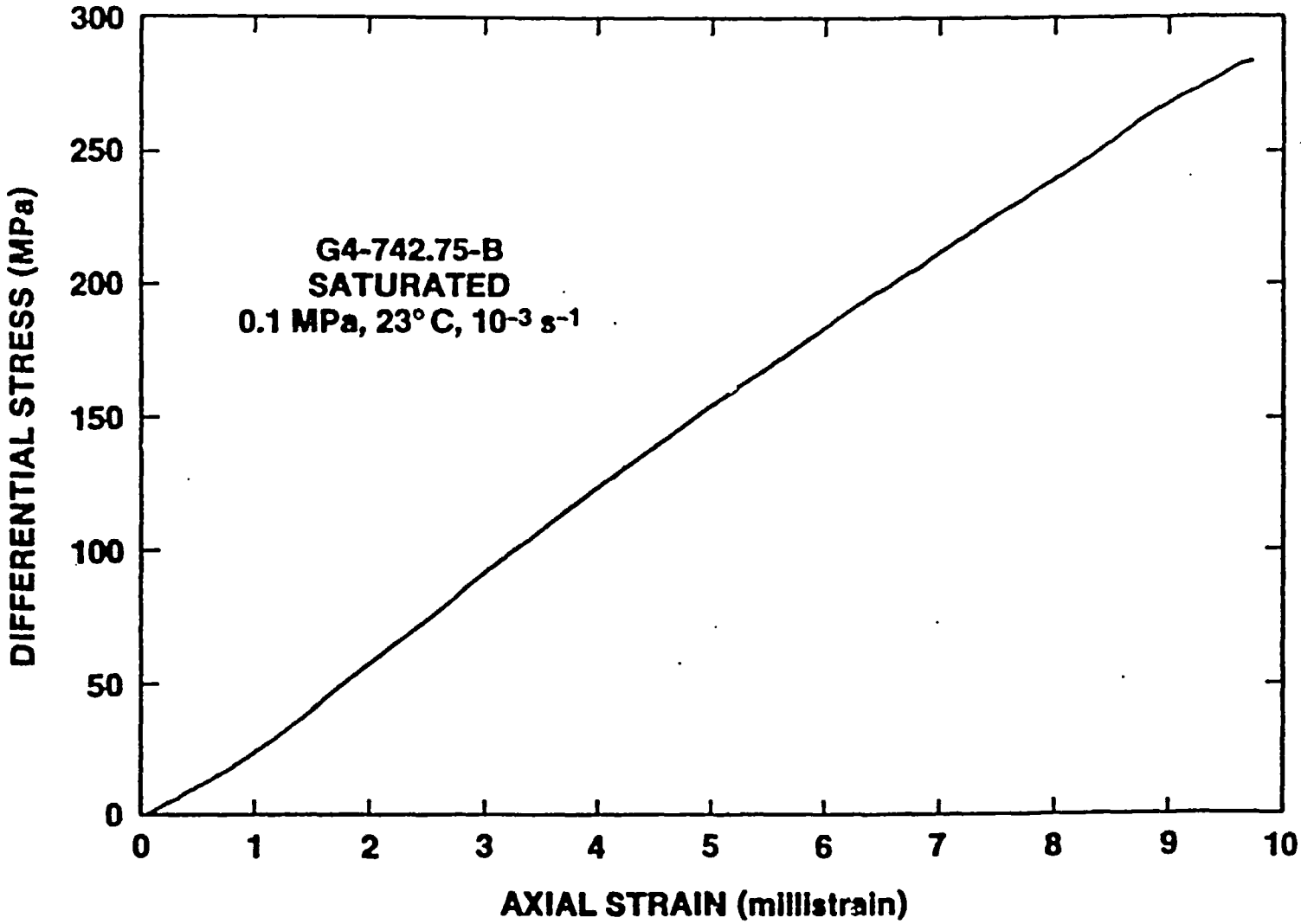

Figure 4i.

Plot of axial stress versus axial strain for sample G4-742.75-B, deformed in compression at 0.1 MPa confining pressure, room temperature, and a nominal axial strain rate of 10^{-3} s^{-1}.

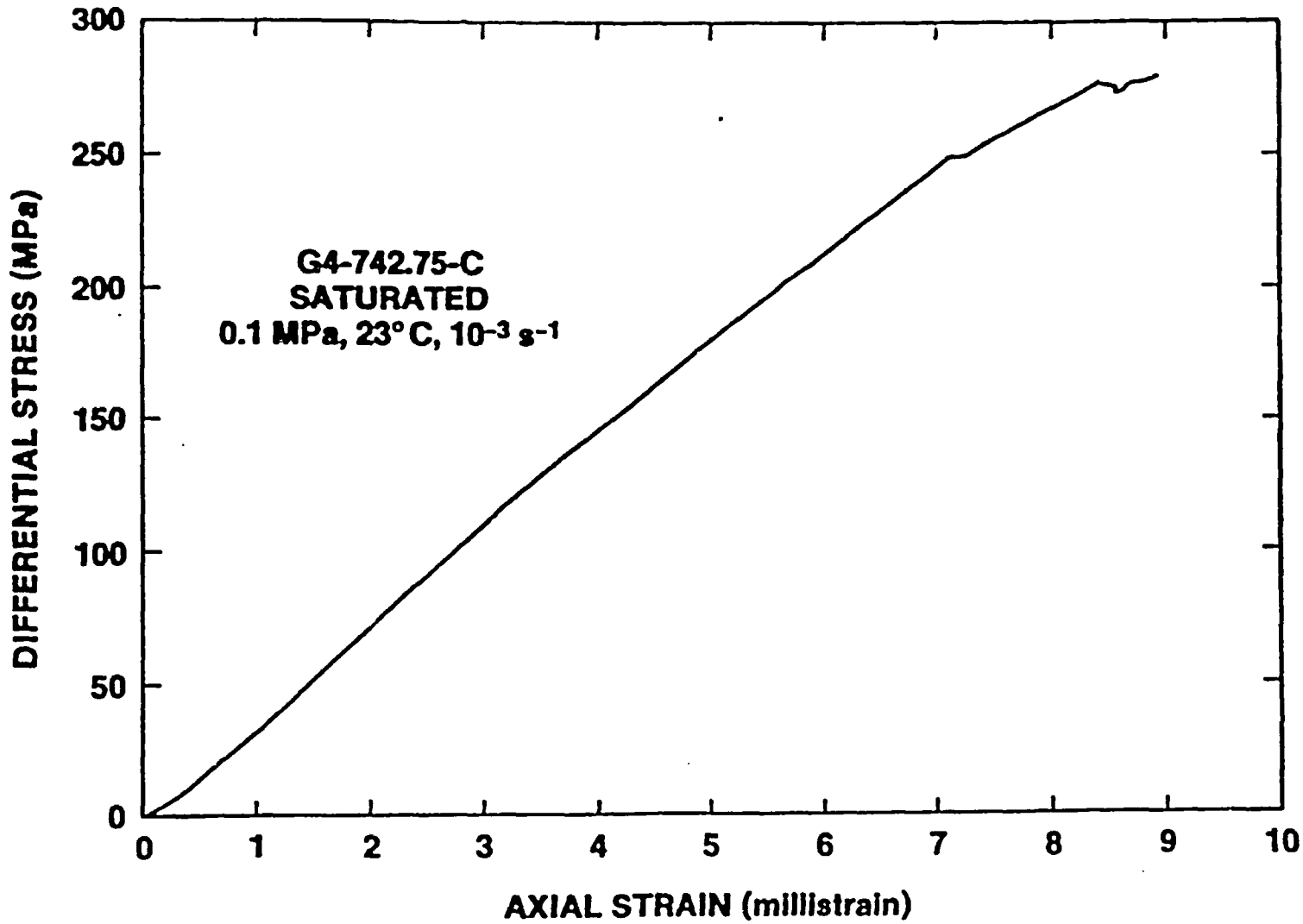

Figure 4j.

Plot of axial stress versus axial strain for sample G4-742.75-C, deformed in compression at 0.1 MPa confining pressure, room temperature, and a nominal axial strain rate of 10^{-3} s^{-1}.

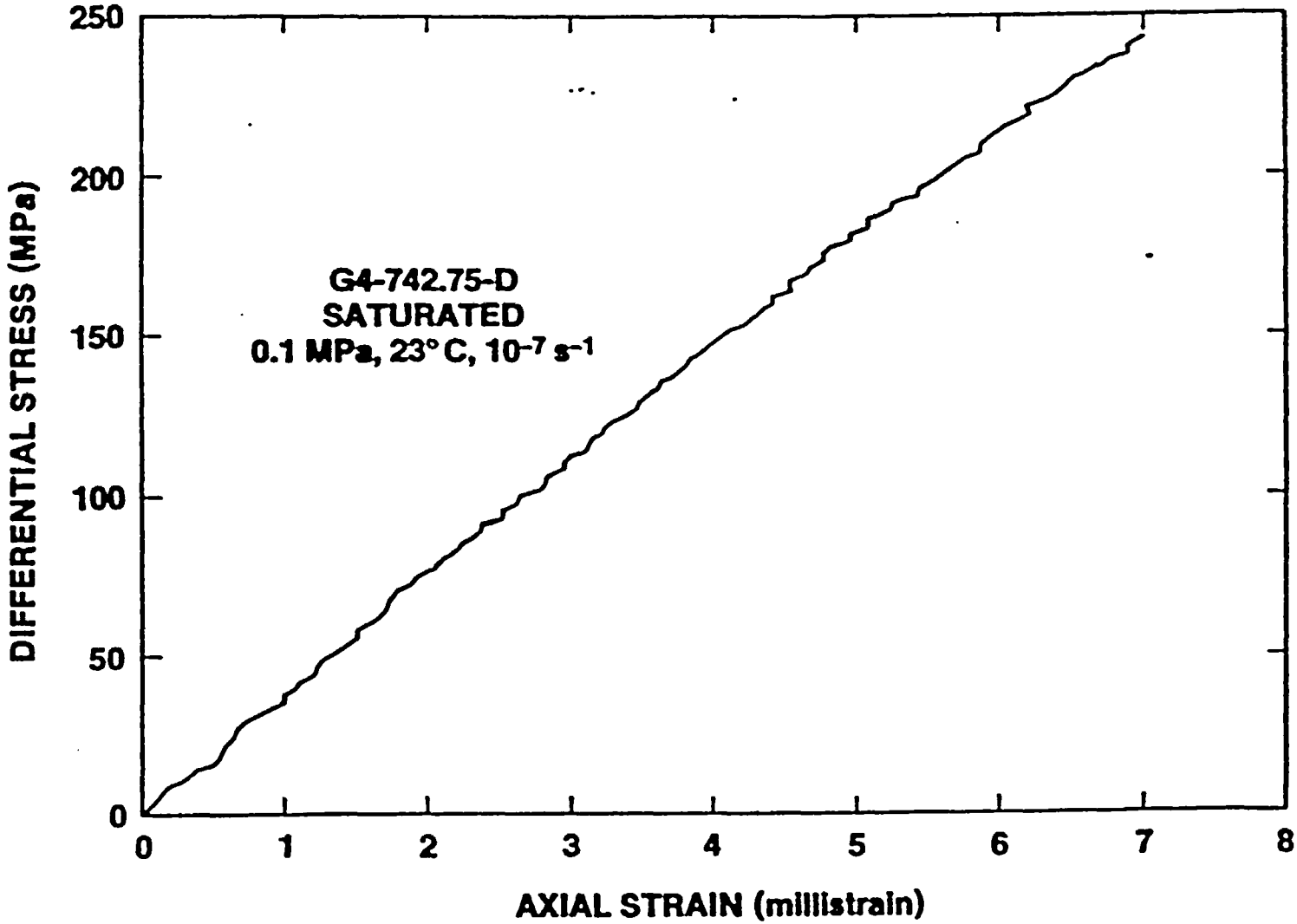

Figure 4k.

Plot of axial stress versus axial strain for sample G4-742.75-D, deformed in compression at 0.1 MPa confining pressure, room temperature, and a nominal axial strain rate of 10^{-7} s^{-1}.

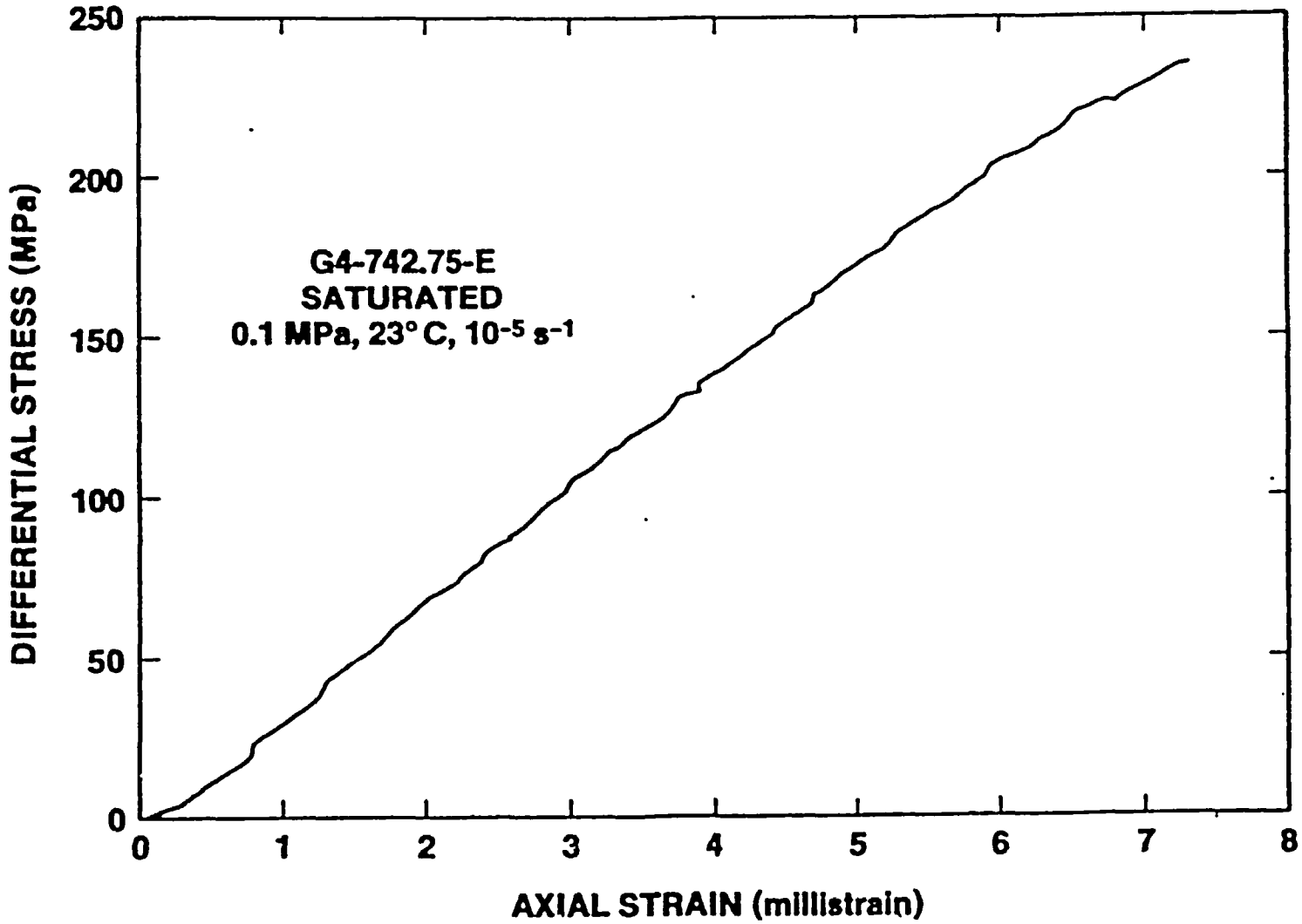

Figure 41.

Plot of axial stress versus axial strain for sample G4-742.75-E, deformed in compression at 0.1 MPa confining pressure, room temperature, and a nominal axial strain rate of 10^{-5} s^{-1}.

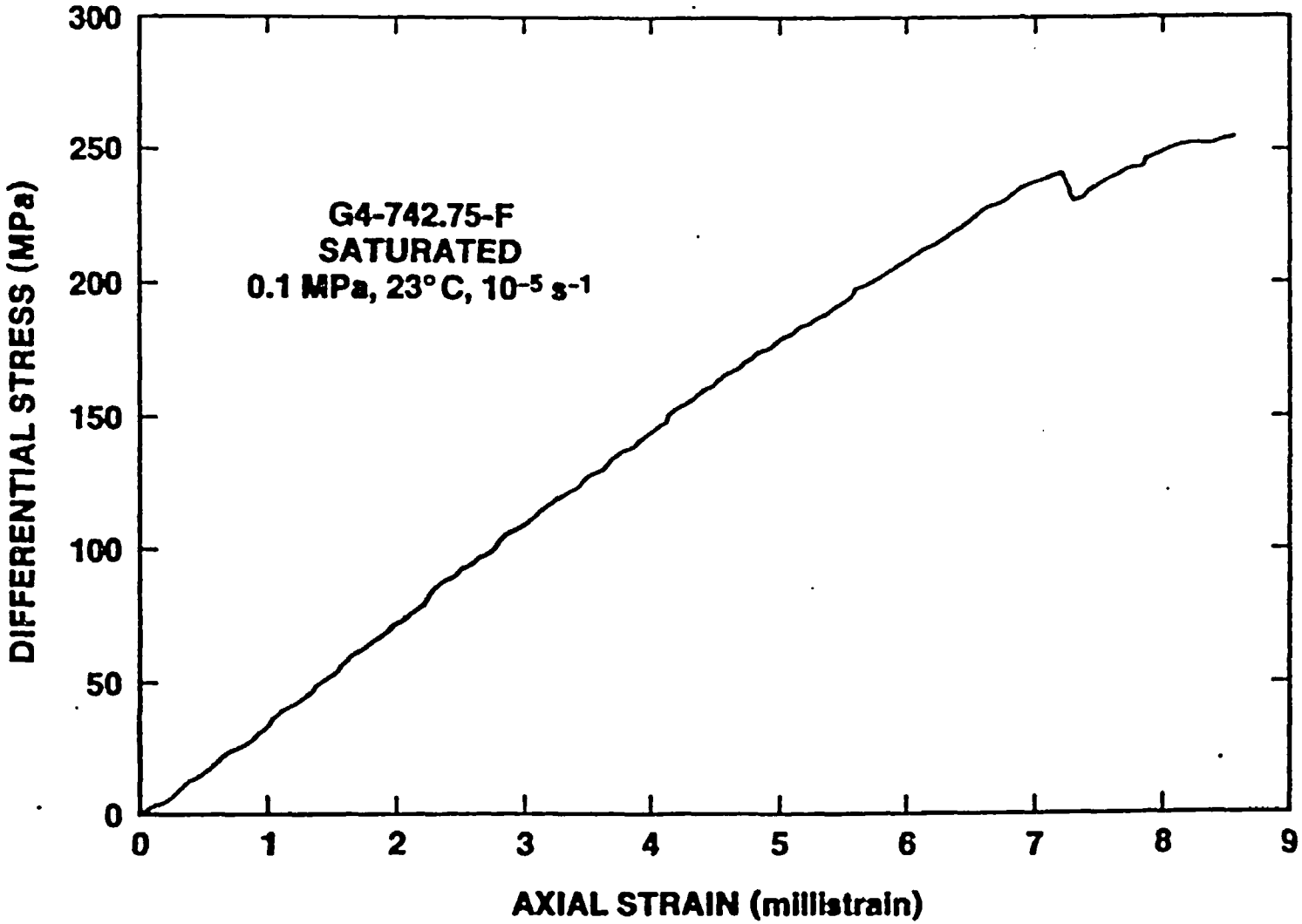

Figure 4m.

Plot of axial stress versus axial strain for sample G4-742.75-F, deformed in compression at 0.1 MPa confining pressure, room temperature, and a nominal axial strain rate of 10^{-5} s^{-1}.

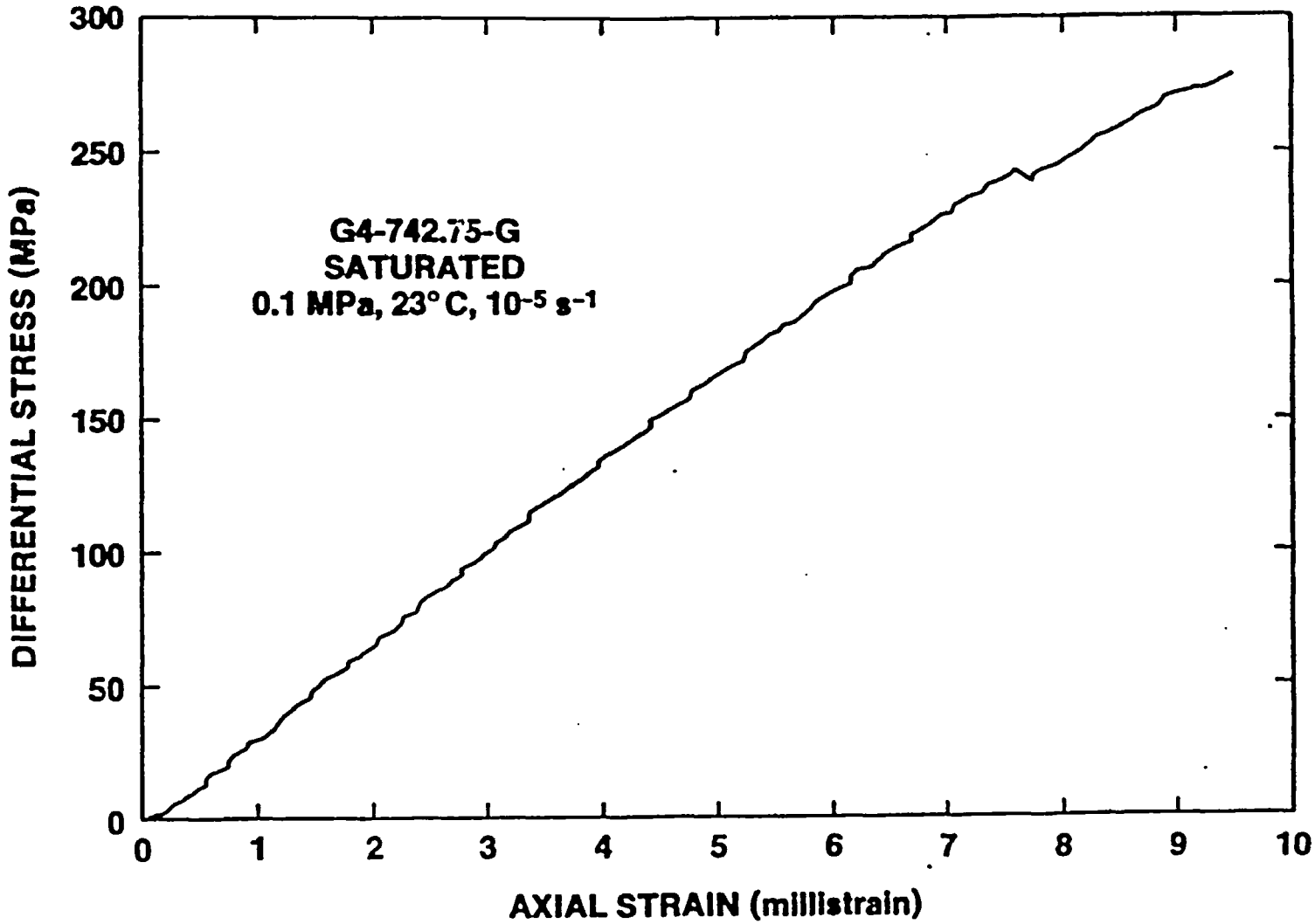

Figure 4n.

Plot of axial stress versus axial strain for sample G4-742.75-G, deformed in compression at 0.1 MPa confining pressure, room temperature, and a nominal axial strain rate of 10^{-5} s^{-1}.

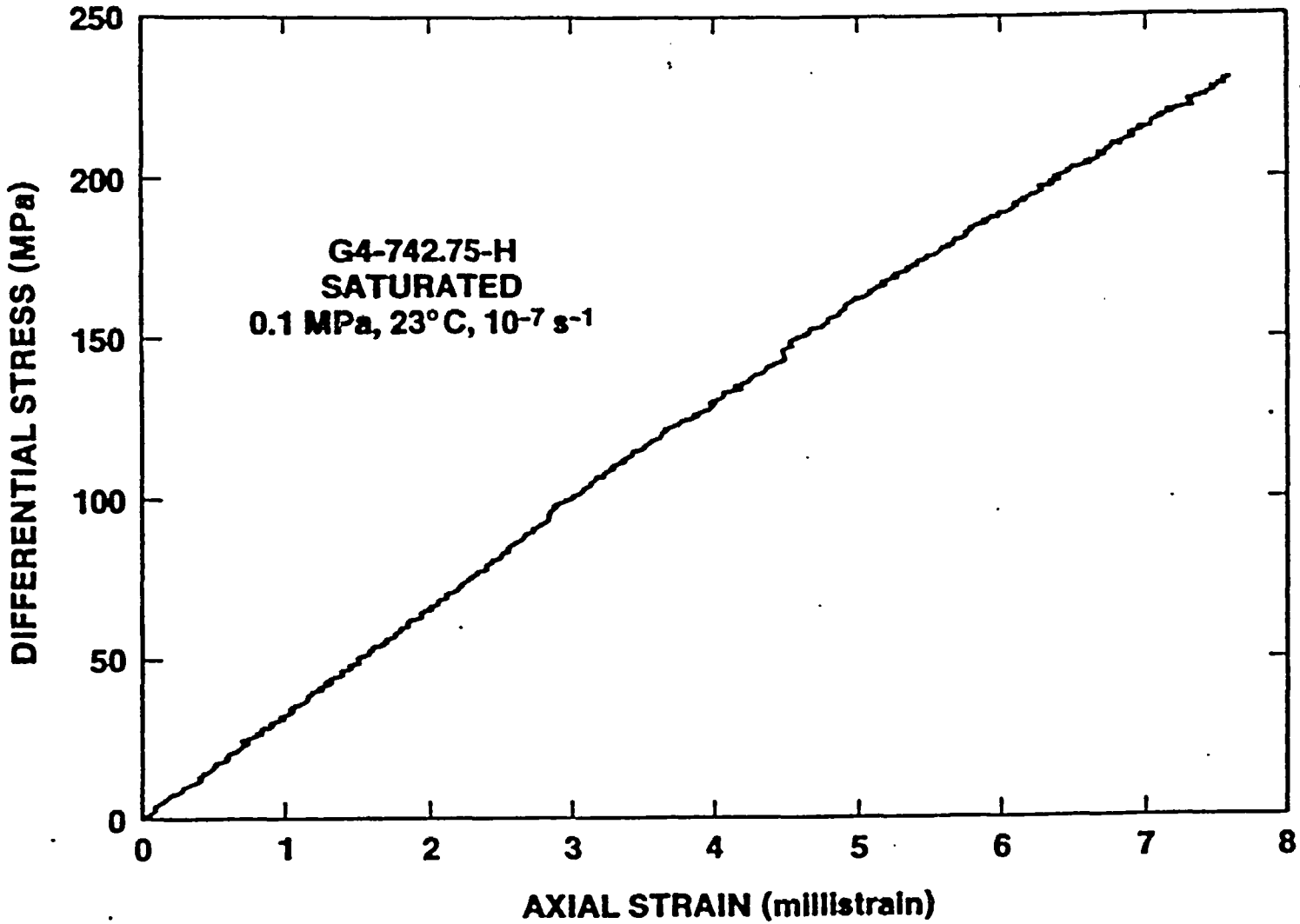

Figure 4o.

Plot of axial stress versus axial strain for sample G4-742.75-H, deformed in compression at 0.1 MPa confining pressure, room temperature, and a nominal axial strain rate of 10^{-7} s^{-1}.

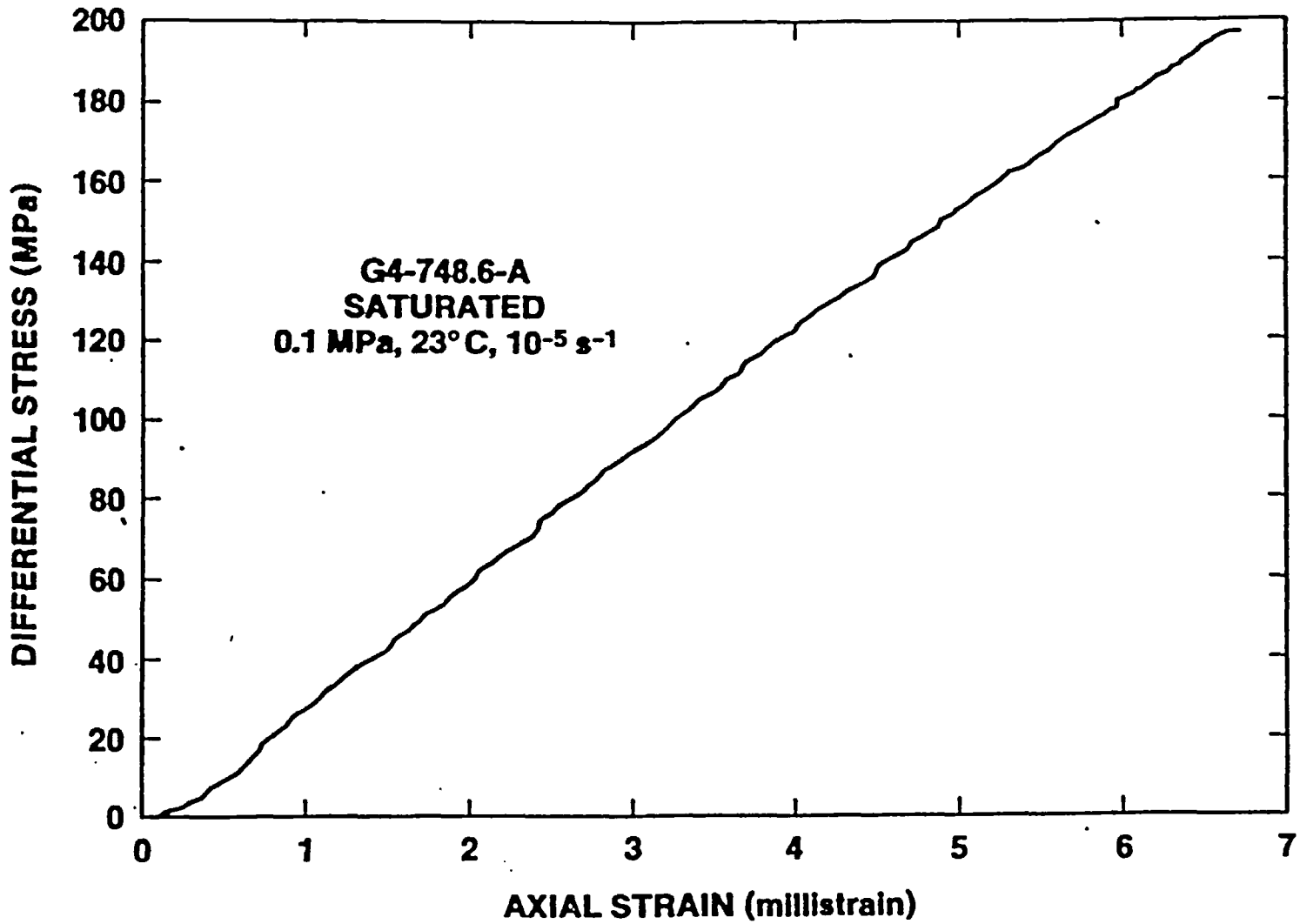

Figure 4p.

Plot of axial stress versus axial strain for sample G4-748.6-A, deformed in compression at 0.1 MPa confining pressure, room temperature, and a nominal axial strain rate of 10^{-5} s^{-1}.

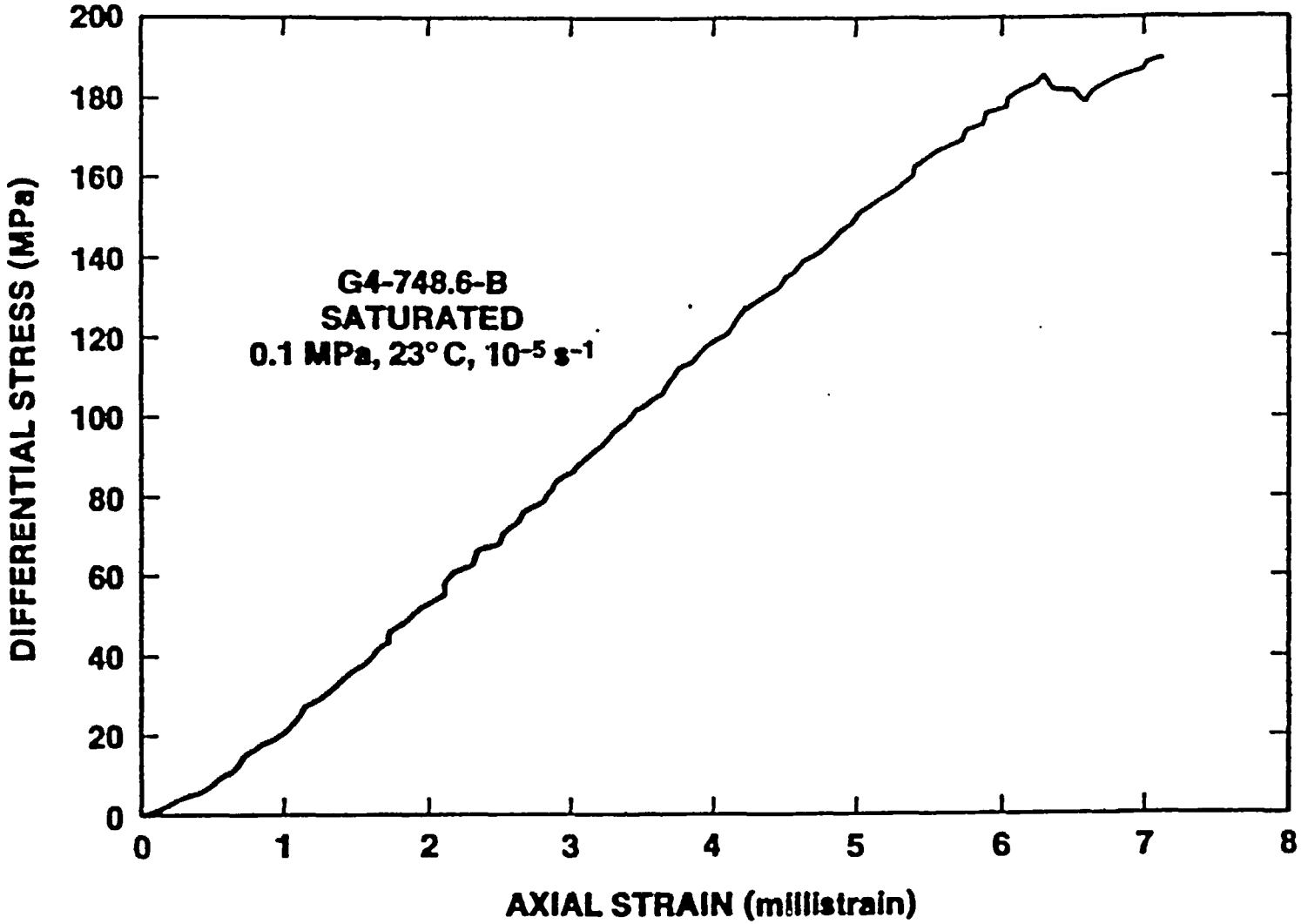

Figure 4q.

Plot of axial stress versus axial strain for sample G4-748.6-B, deformed in compression at 0.1 MPa confining pressure, room temperature, and a nominal axial strain rate of 10^{-5} s^{-1}.

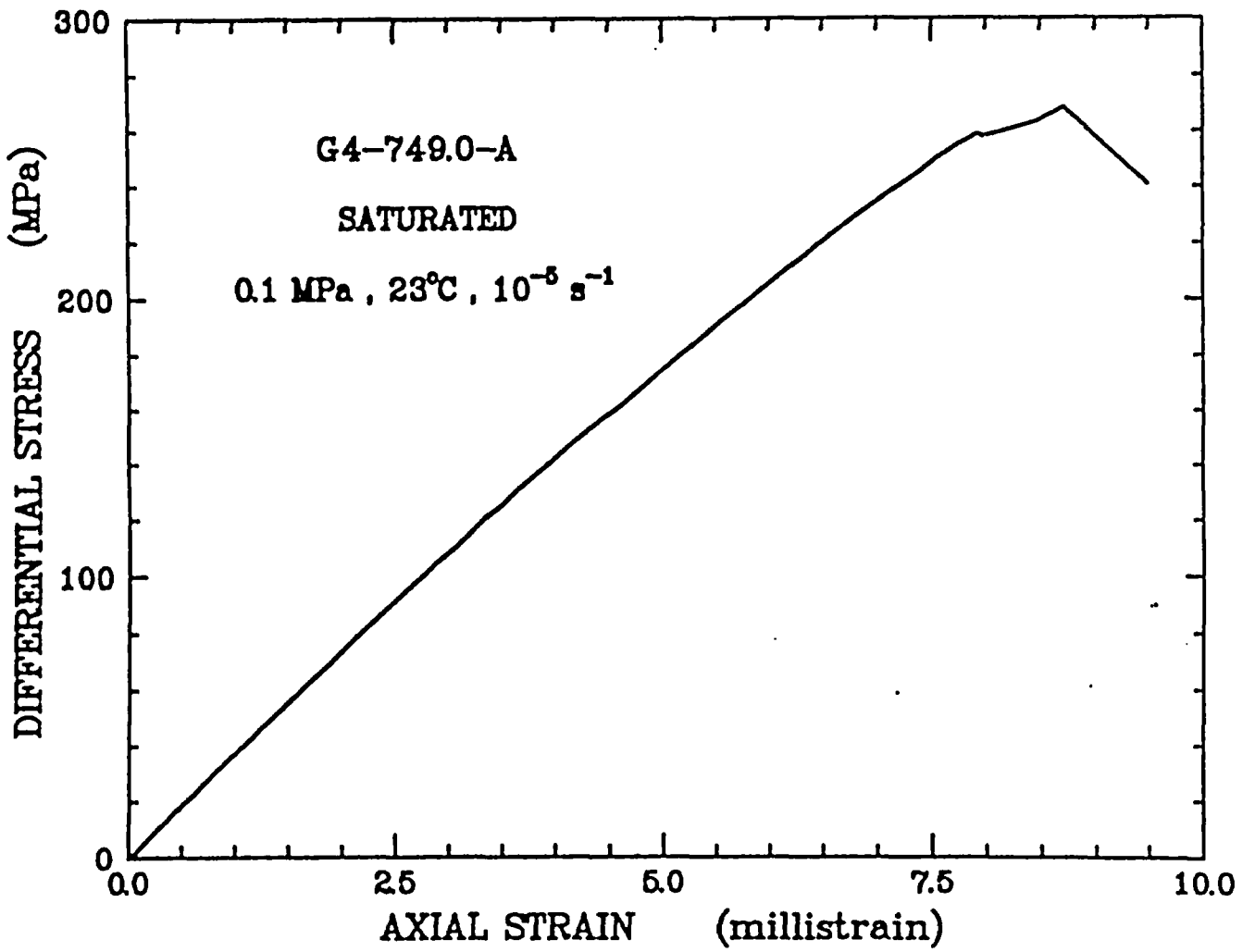

Figure 4r.

Plot of axial stress versus axial strain for sample G4-749.0-A, deformed in compression at 0.1 MPa confining pressure, room temperature, and a nominal axial strain rate of 10^{-5} s^{-1}.

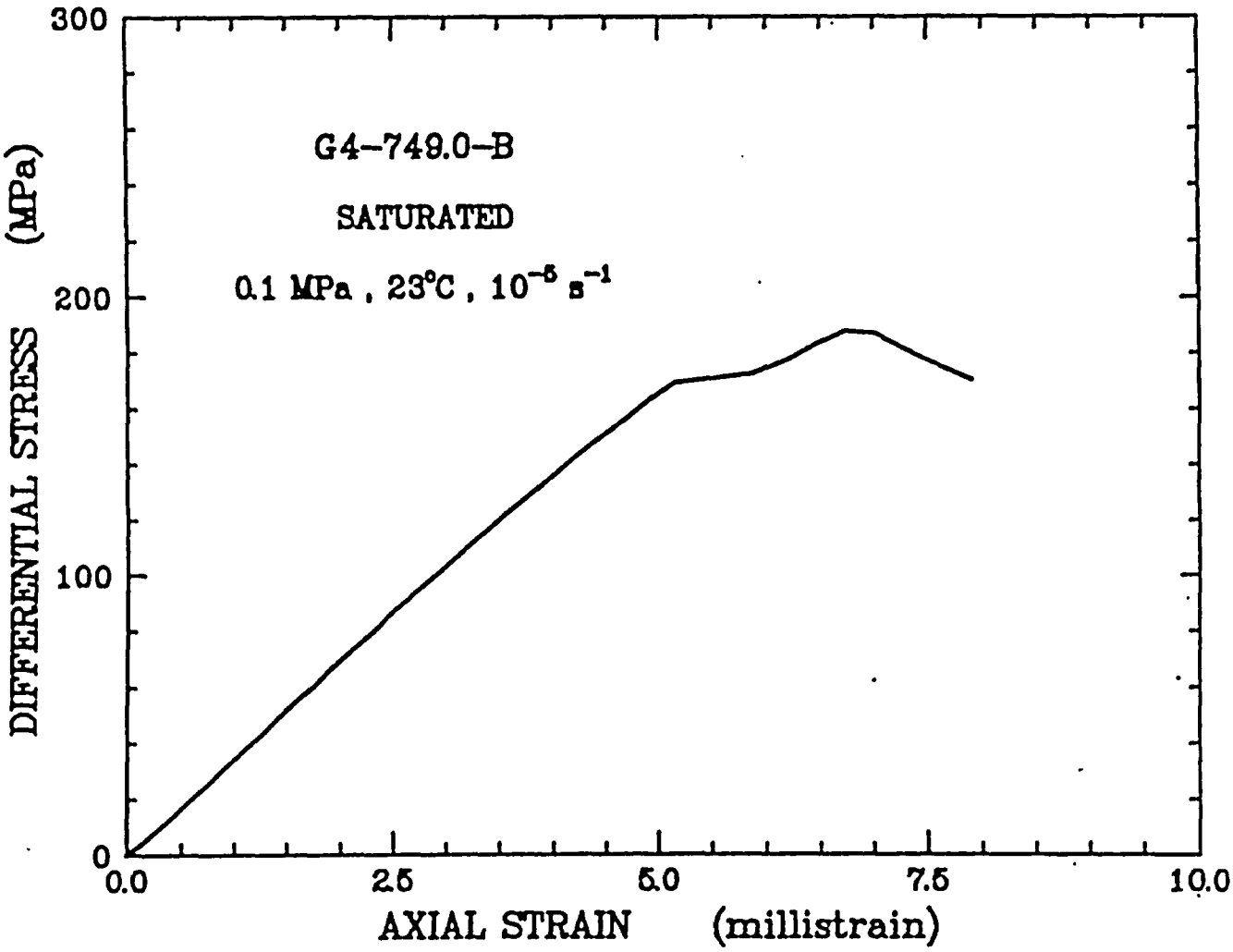

Figure 4s.

Plot of axial stress versus axial strain for sample G4-749.0-B, deformed in compression at 0.1 MPa confining pressure, room temperature, and a nominal axial strain rate of 10^{-5} s^{-1}.

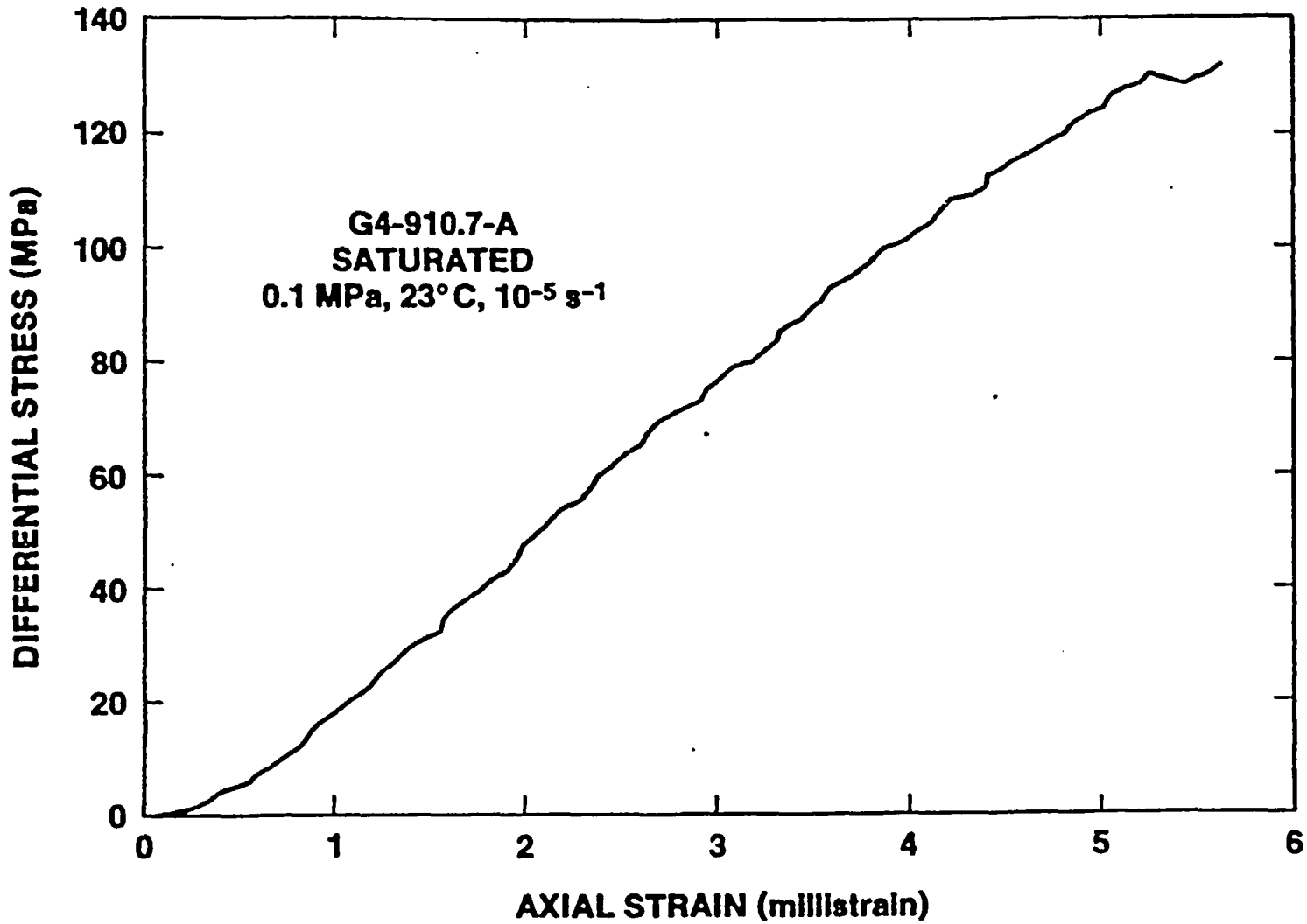

Figure 4t.

Plot of axial stress versus axial strain for sample G4-910.7-A, deformed in compression at 0.1 MPa confining pressure, room temperature, and a nominal axial strain rate of 10^{-5} s^{-1}.

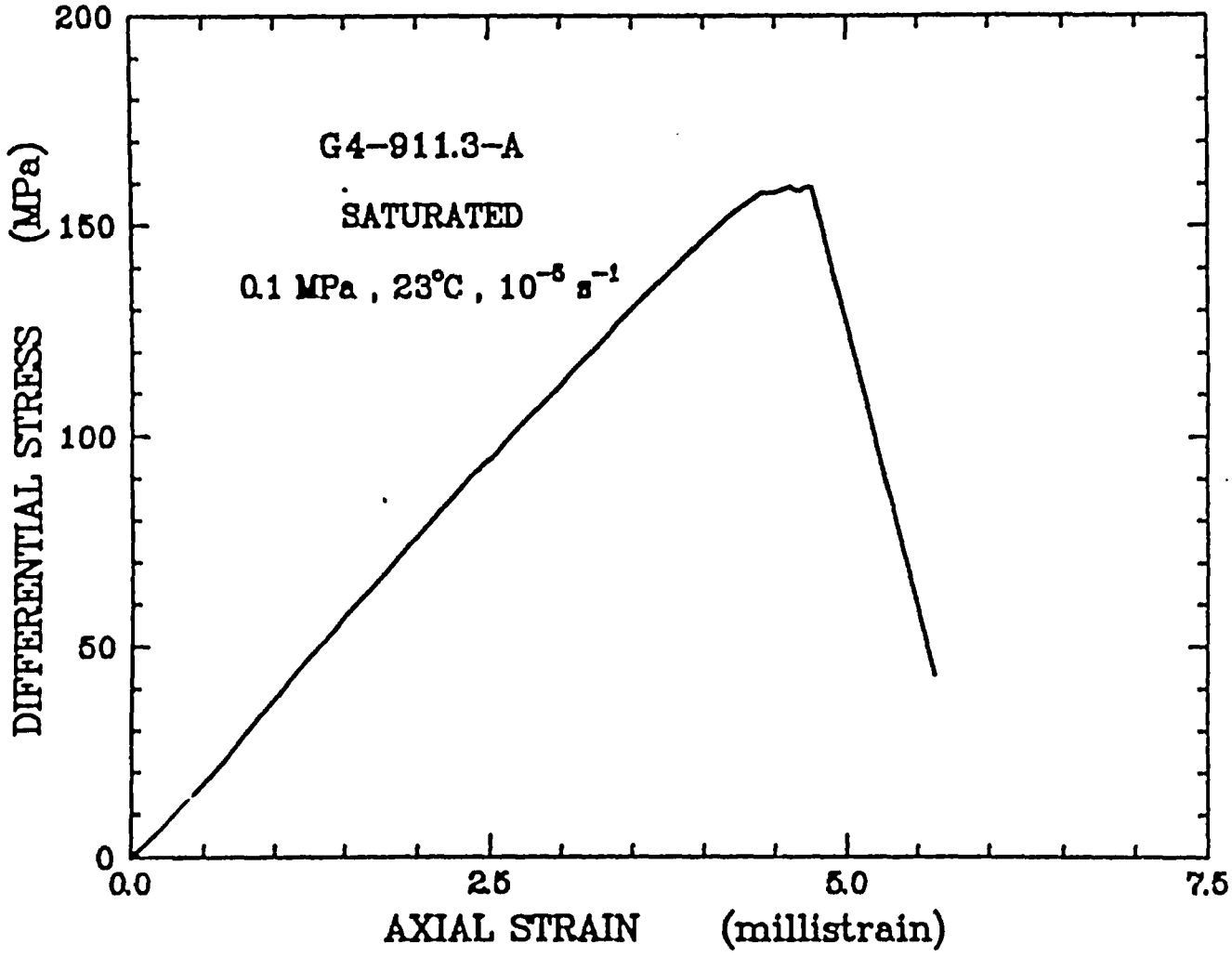

Figure 4u.

Plot of axial stress versus axial strain for sample G4-911.3-A, deformed in compression at 0.1 MPa confining pressure, room temperature, and a nominal axial strain rate of 10^{-5} s^{-1}.

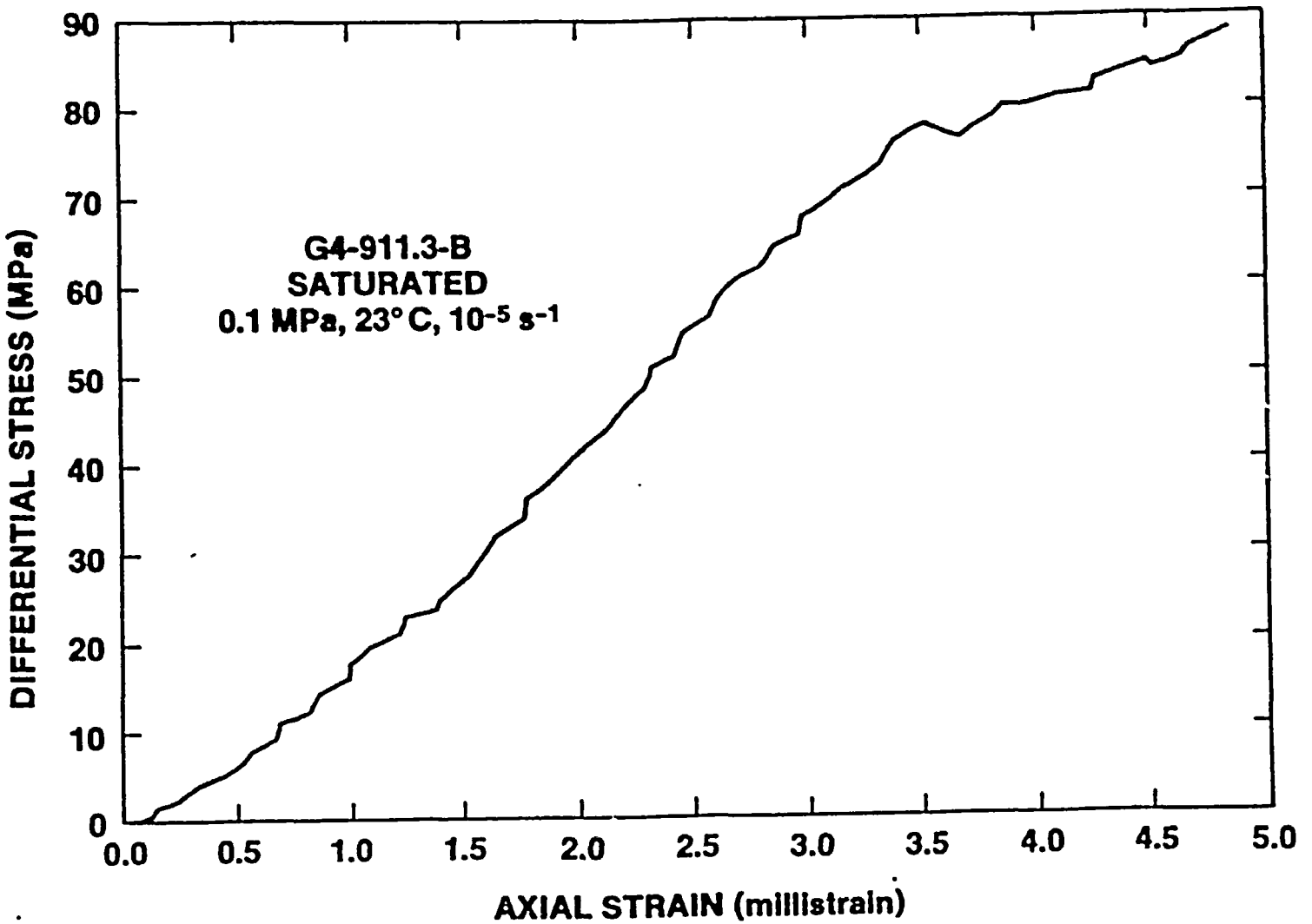

Figure 4v.

Plot of axial stress versus axial strain for sample G4-911.3-B, deformed in compression at 0.1 MPa confining pressure, room temperature, and a nominal axial strain rate of 10^{-5} s^{-1}.

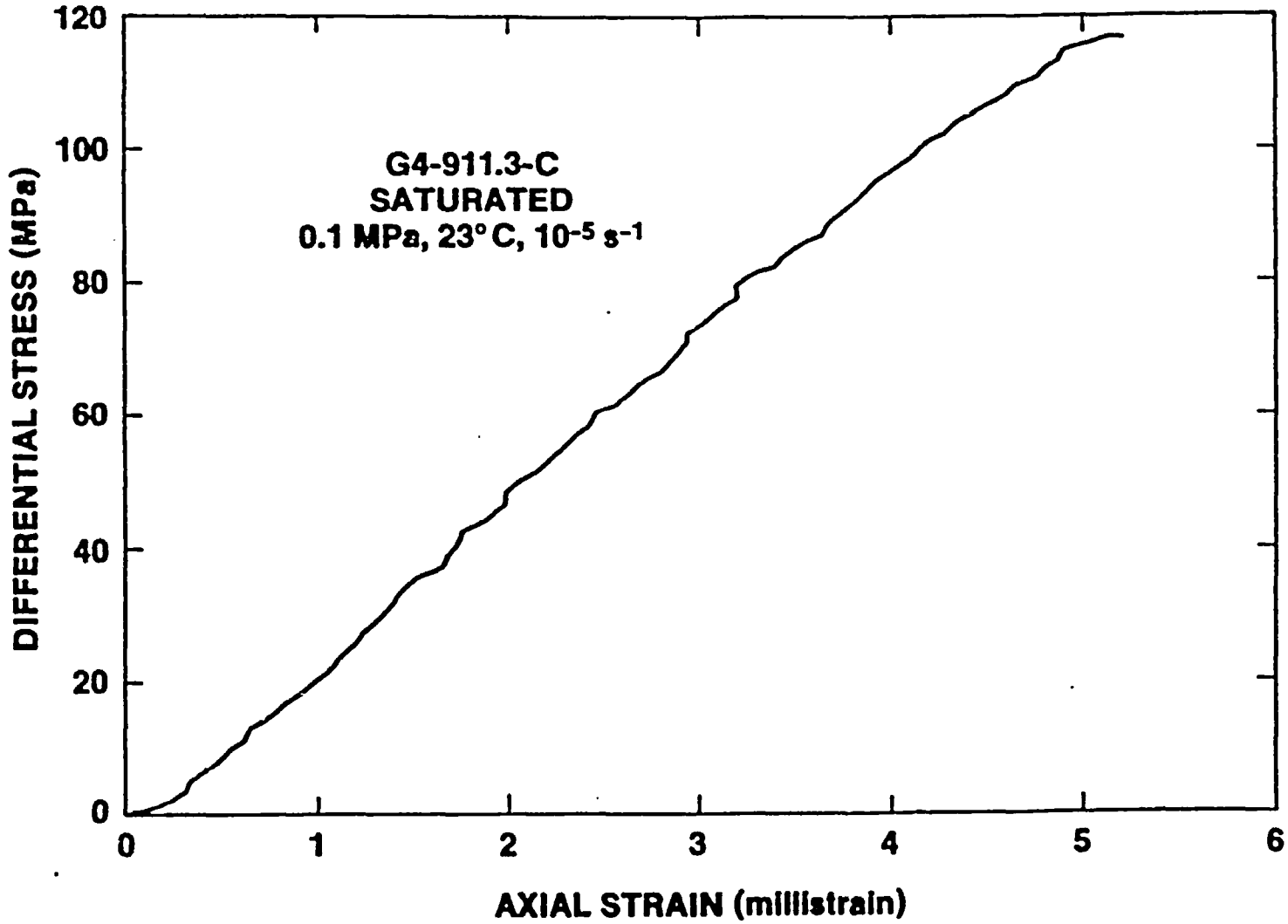

Figure 4w.

Plot of axial stress versus axial strain for sample G4-911.3-C, deformed in compression at 0.1 MPa confining pressure, room temperature, and a nominal axial strain rate of 10^{-5} s^{-1}.

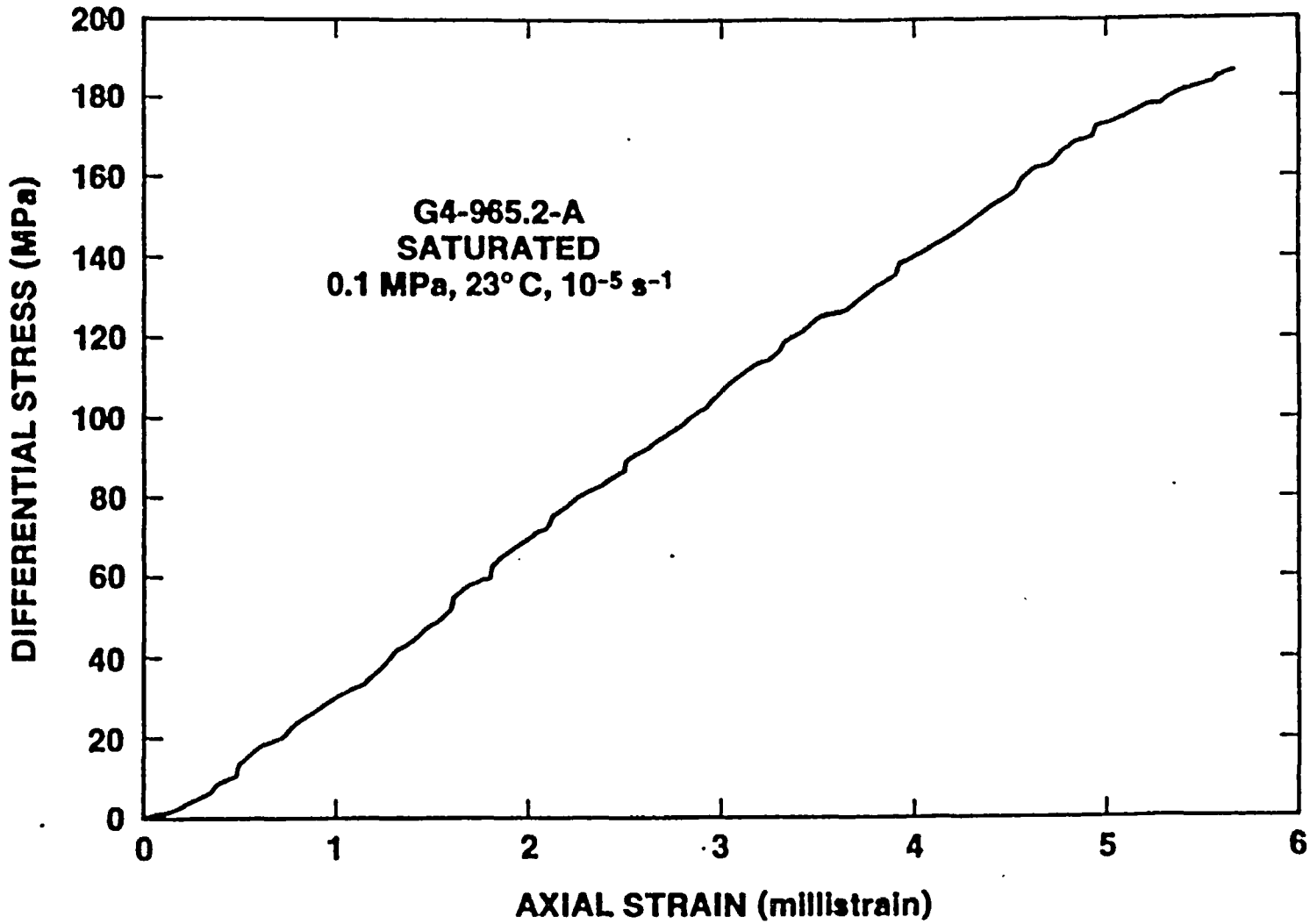

Figure 4x.

Plot of axial stress versus axial strain for sample G4-965.2-A, deformed in compression at 0.1 MPa confining pressure, room temperature, and a nominal axial strain rate of 10^{-5} s^{-1}.

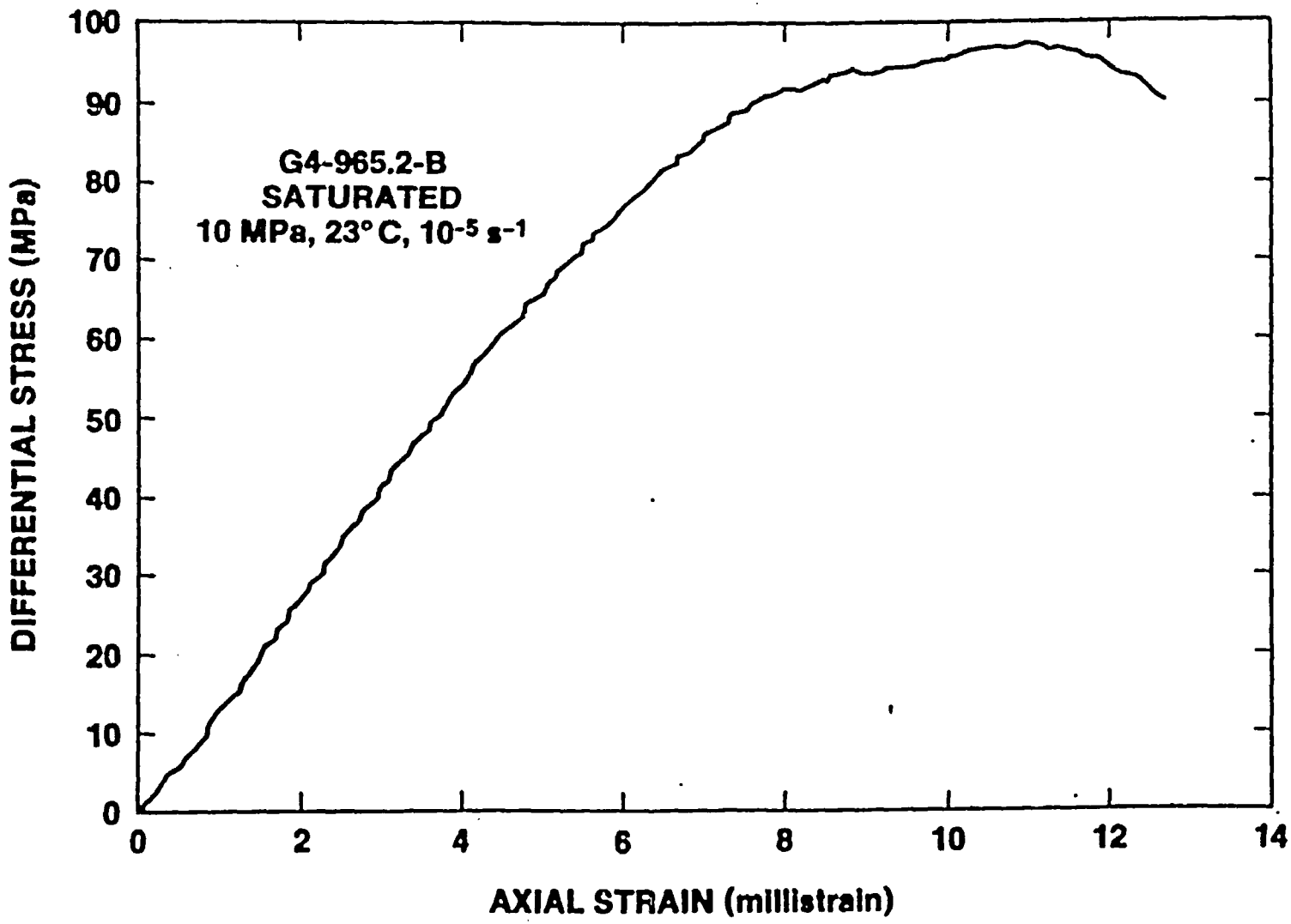

Figure 4y.

Plot of axial stress versus axial strain for sample G4-965.2-B, deformed in compression at 10 MPa confining pressure, room temperature, and a nominal axial strain rate of 10^{-5} s^{-1}.

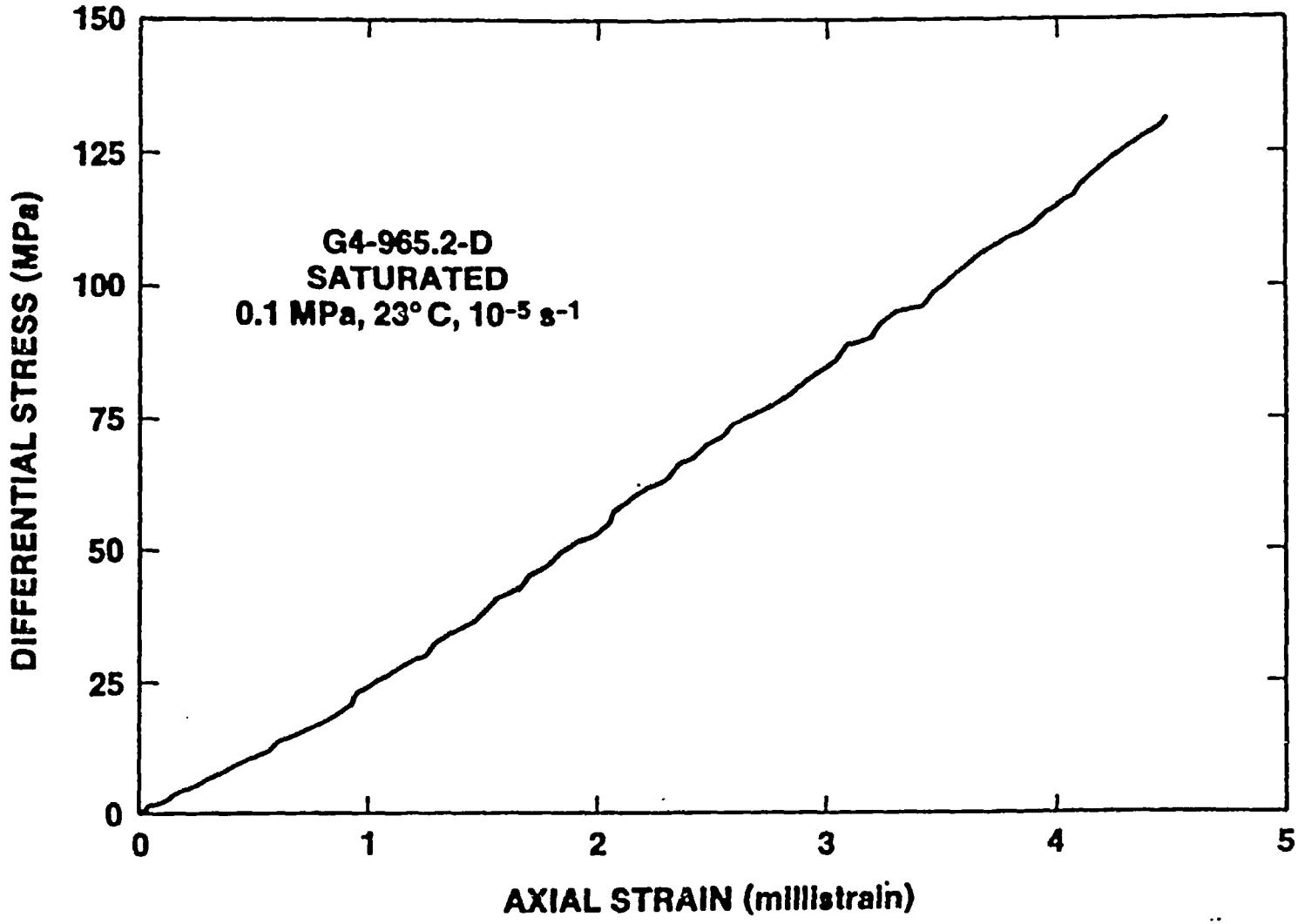

Figure 4z.

Plot of axial stress versus axial strain for sample G4-965.2-D, deformed in compression at 0.1 MPa confining pressure, room temperature, and a nominal axial strain rate of 10^{-5} s^{-1}.

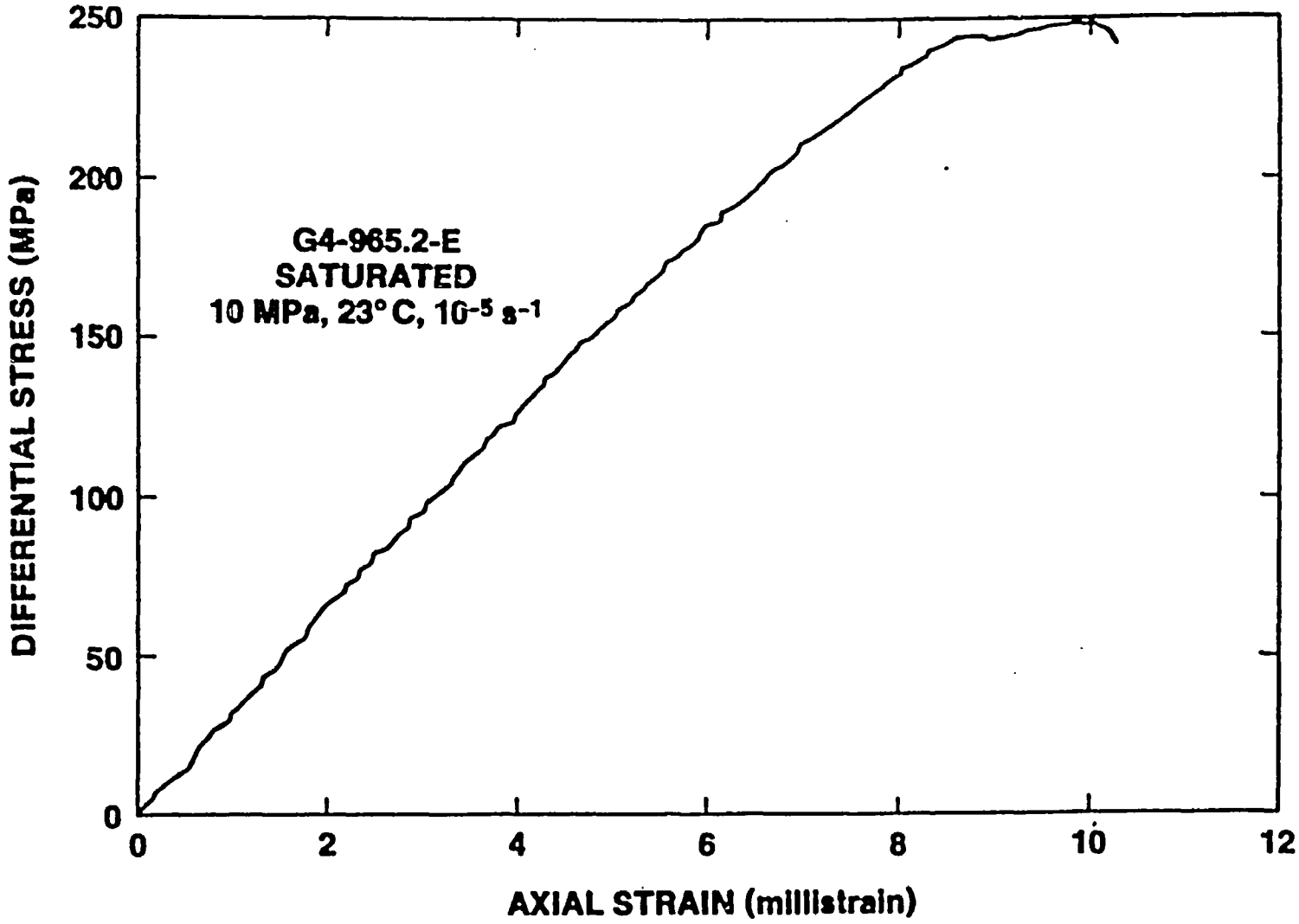

Figure 4aa.

Plot of axial stress versus axial strain for sample G4-965.2-E, deformed in compression at 10 MPa confining pressure, room temperature, and a nominal axial strain rate of 10^{-5} s^{-1}.

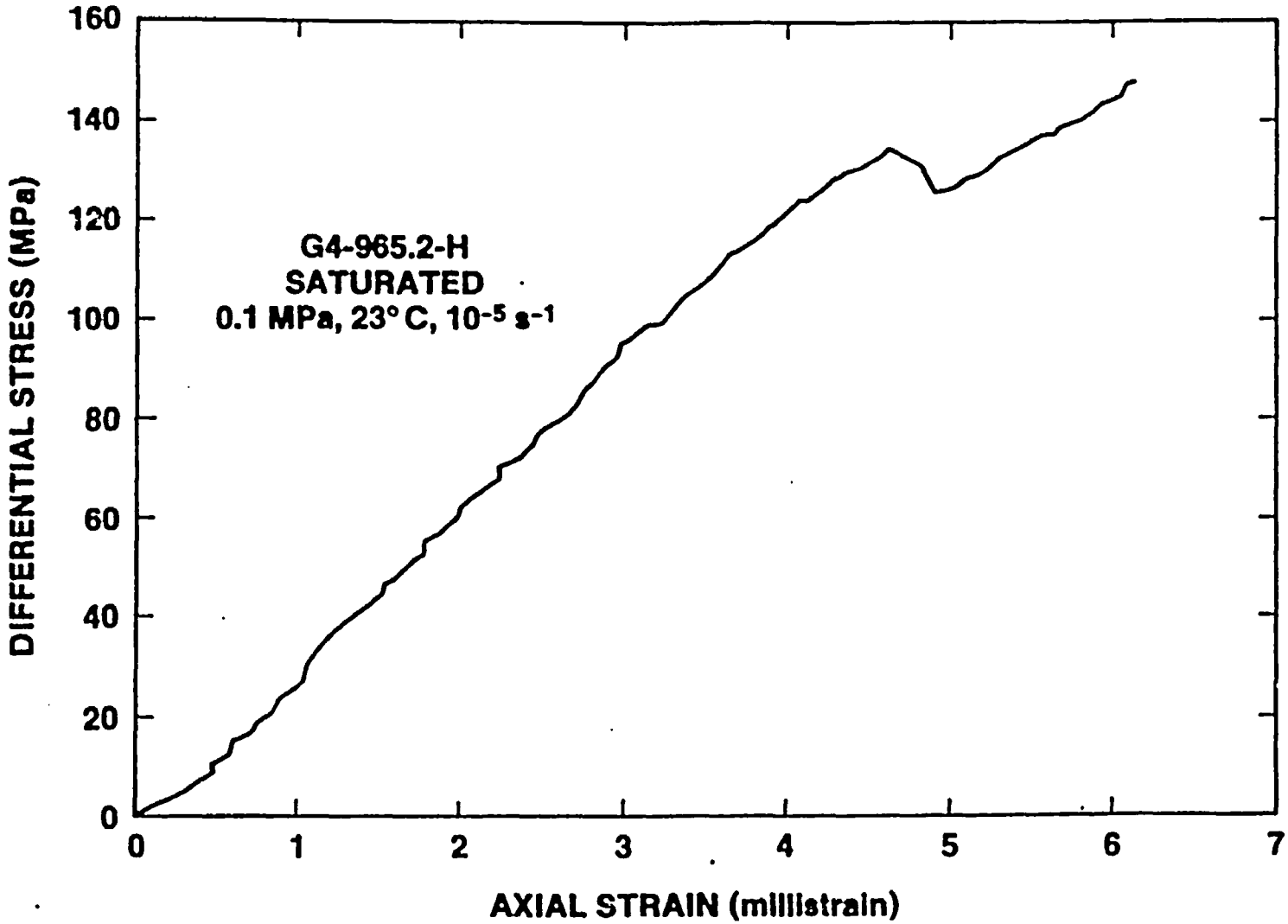

Figure 4bb.

Plot of axial stress versus axial strain for sample G4-965.2-H, deformed in compression at 0.1 MPa confining pressure, room temperature, and a nominal axial strain rate of 10^{-5} s^{-1}.

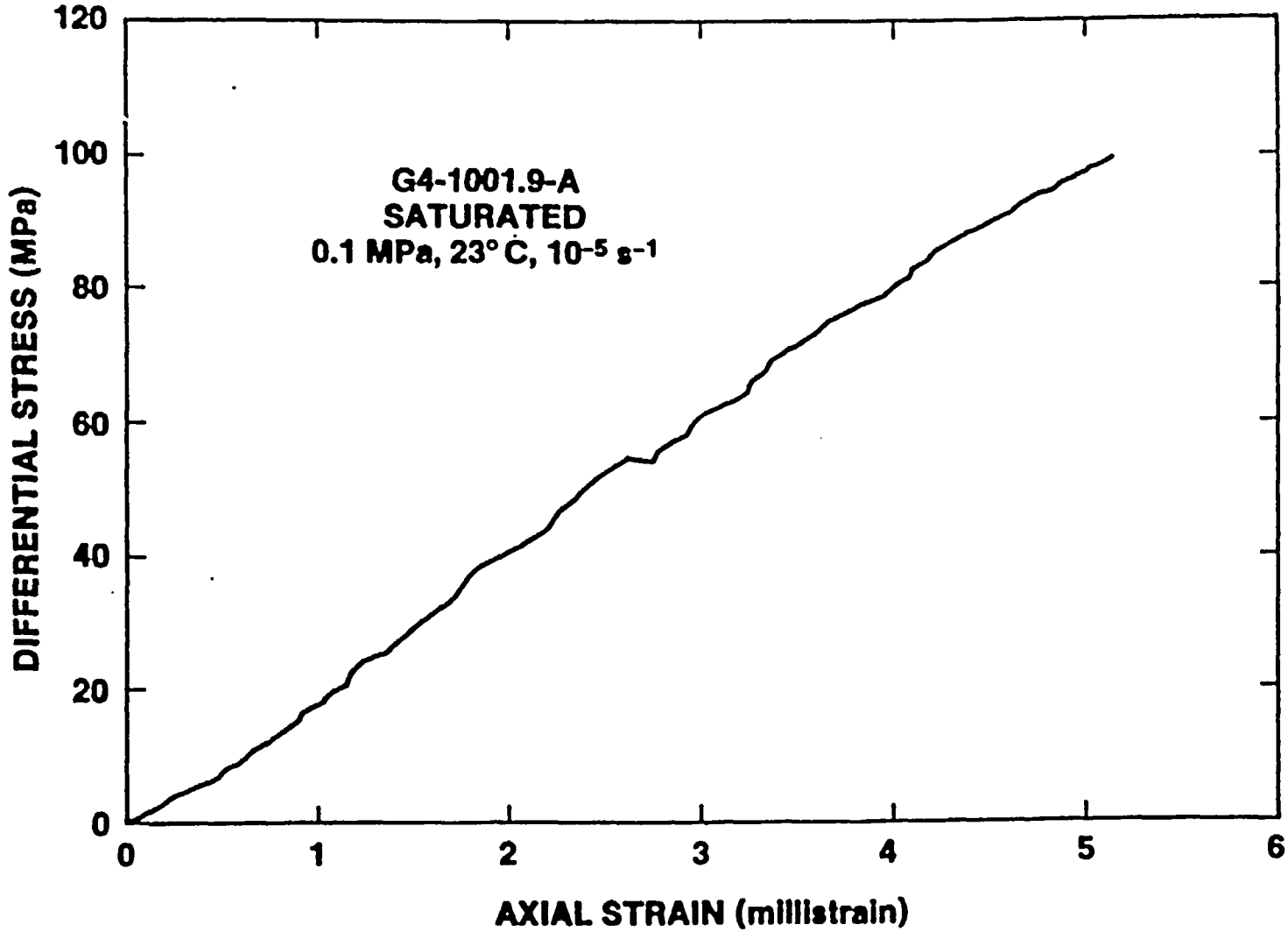

Figure 4cc.

Plot of axial stress versus axial strain for sample G4-1001.9-A, deformed in compression at 0.1 MPa confining pressure, room temperature, and a nominal axial strain rate of 10^{-5} s^{-1}.

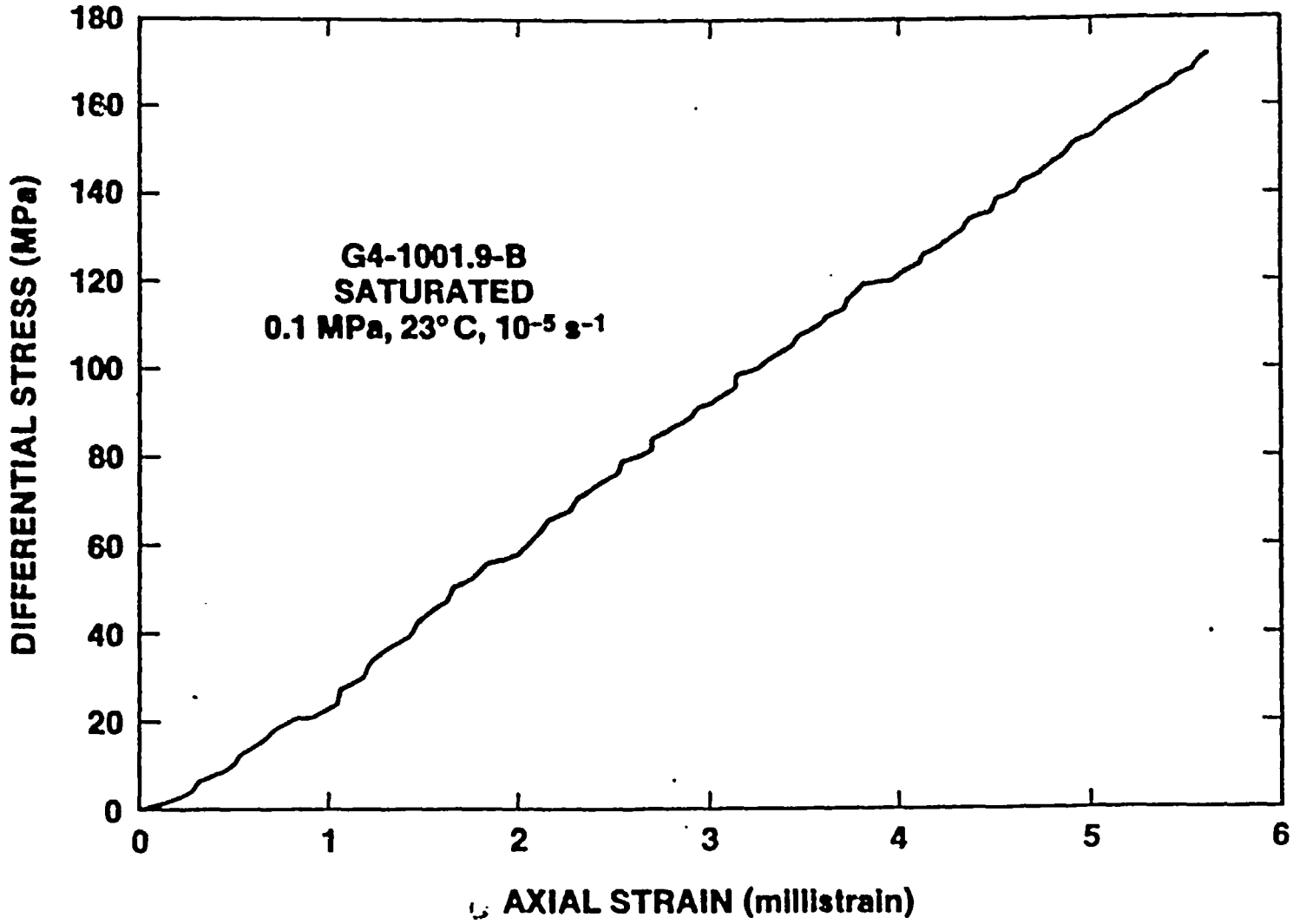

Figure 4dd.

Plot of axial stress versus axial strain for sample G4-1001.9-B, deformed in compression at 0.1 MPa confining pressure, room temperature, and a nominal axial strain rate of 10^{-5} s^{-1}.

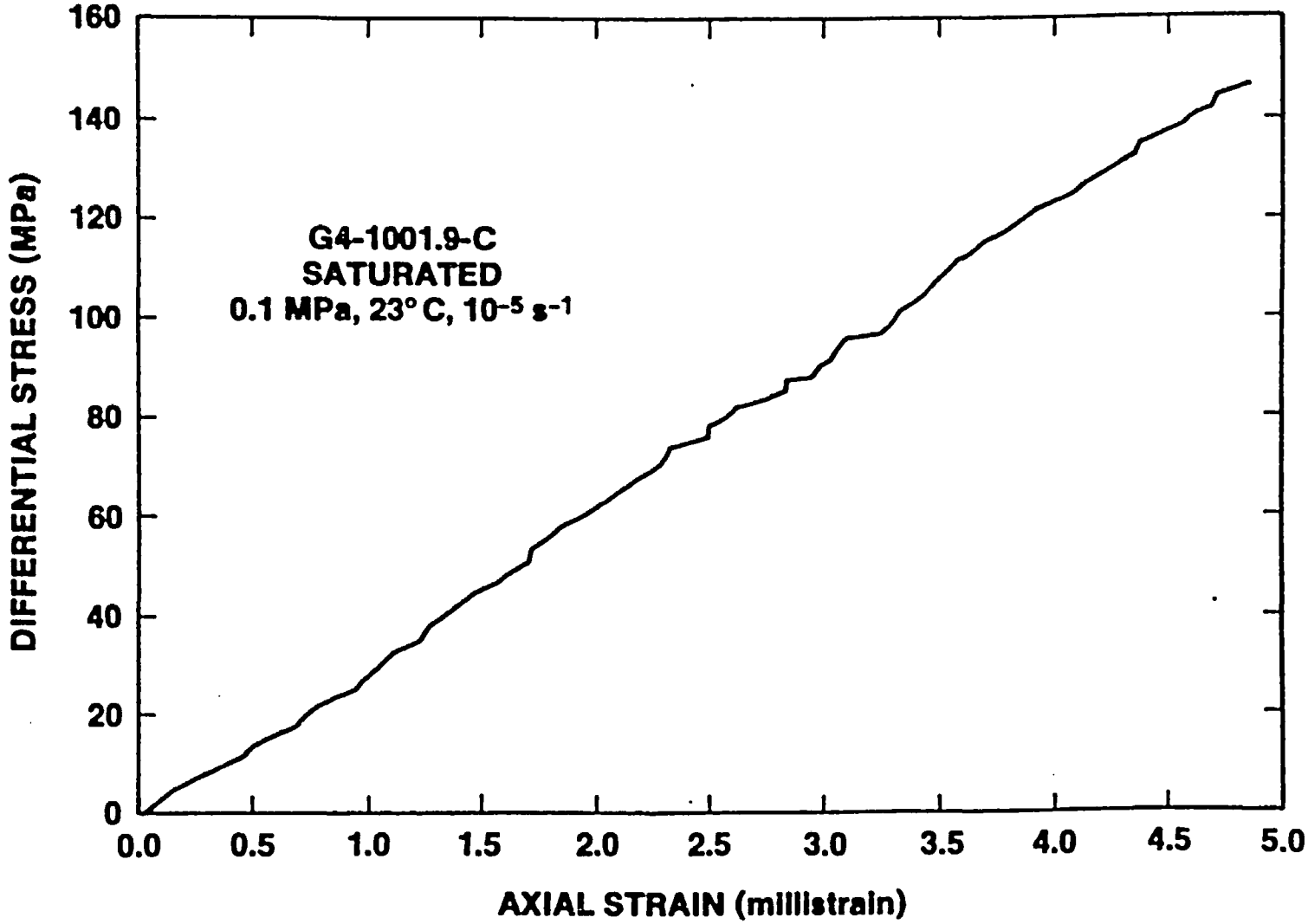

Figure 4ee.

Plot of axial stress versus axial strain for sample G4-1001.9-C, deformed in compression at 0.1 MPa confining pressure, room temperature, and a nominal axial strain rate of 10^{-5} s^{-1}.

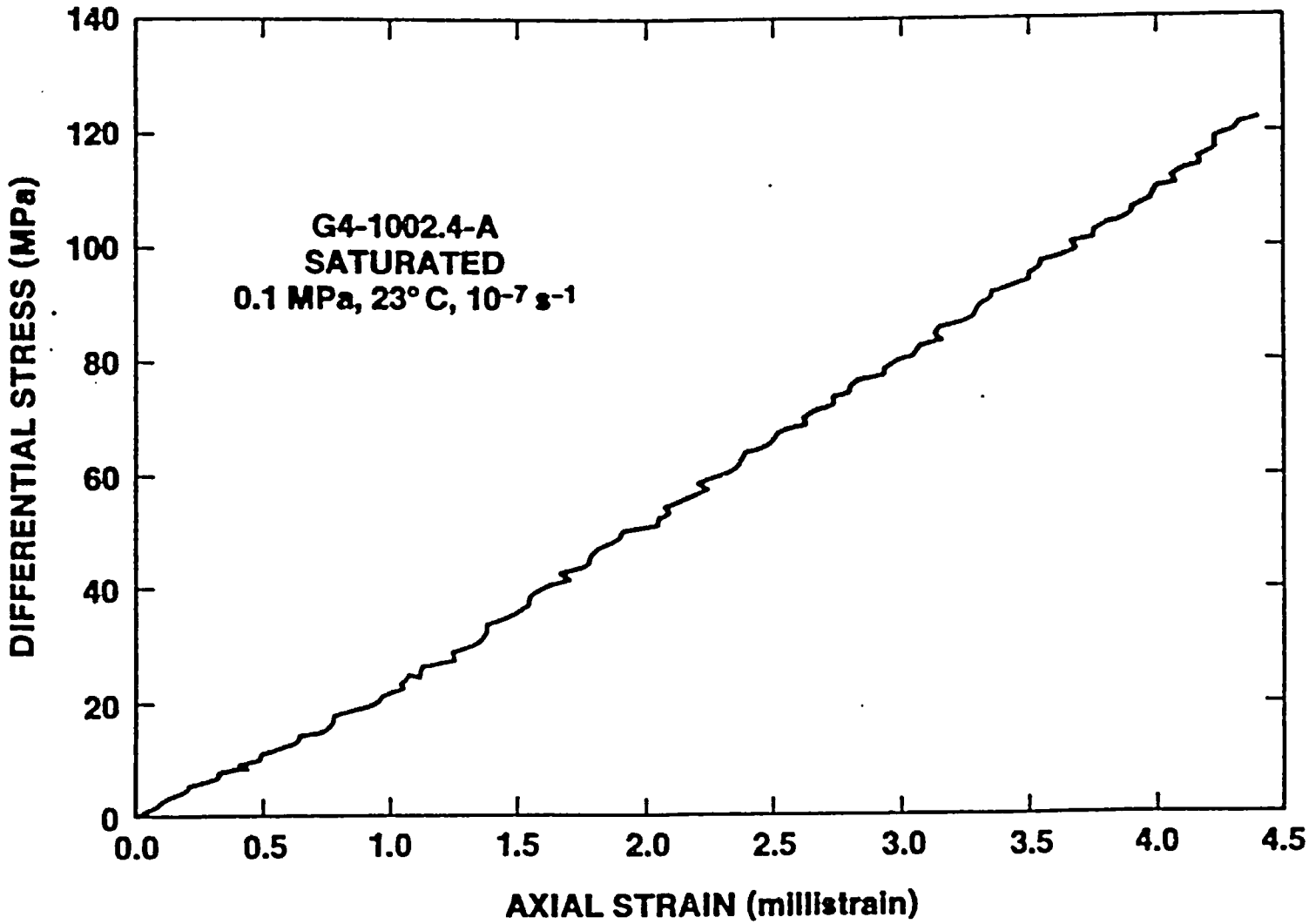

Figure 4ff.

Plot of axial stress versus axial strain for sample G4-1002.4-A, deformed in compression at 0.1 MPa confining pressure, room temperature, and a nominal axial strain rate of 10^{-7} s^{-1}.

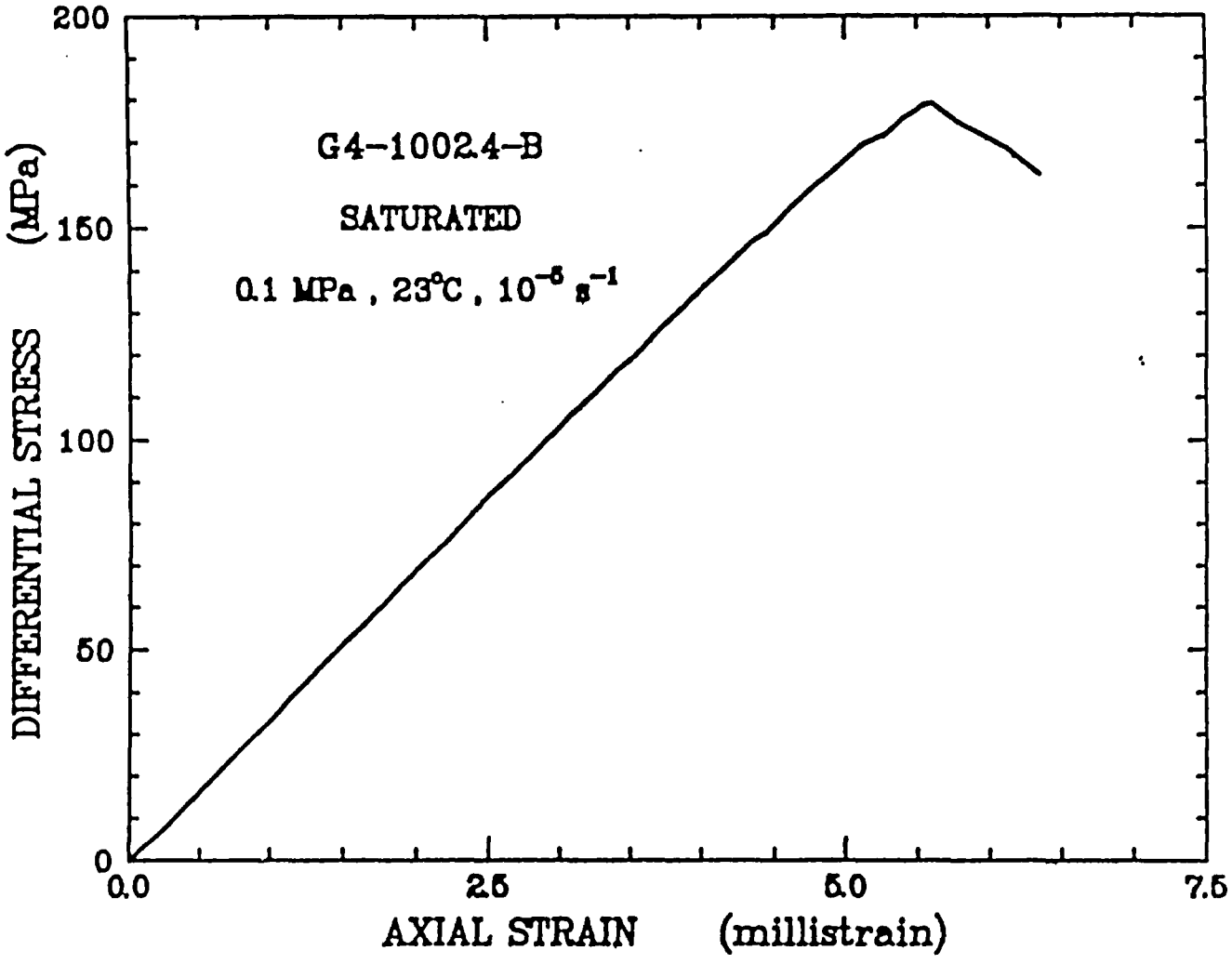

Figure 4gg.

Plot of axial stress versus axial strain for sample G4-1002.4-B, deformed in compression at 0.1 MPa confining pressure, room temperature, and a nominal axial strain rate of 10^{-5} s^{-1}.

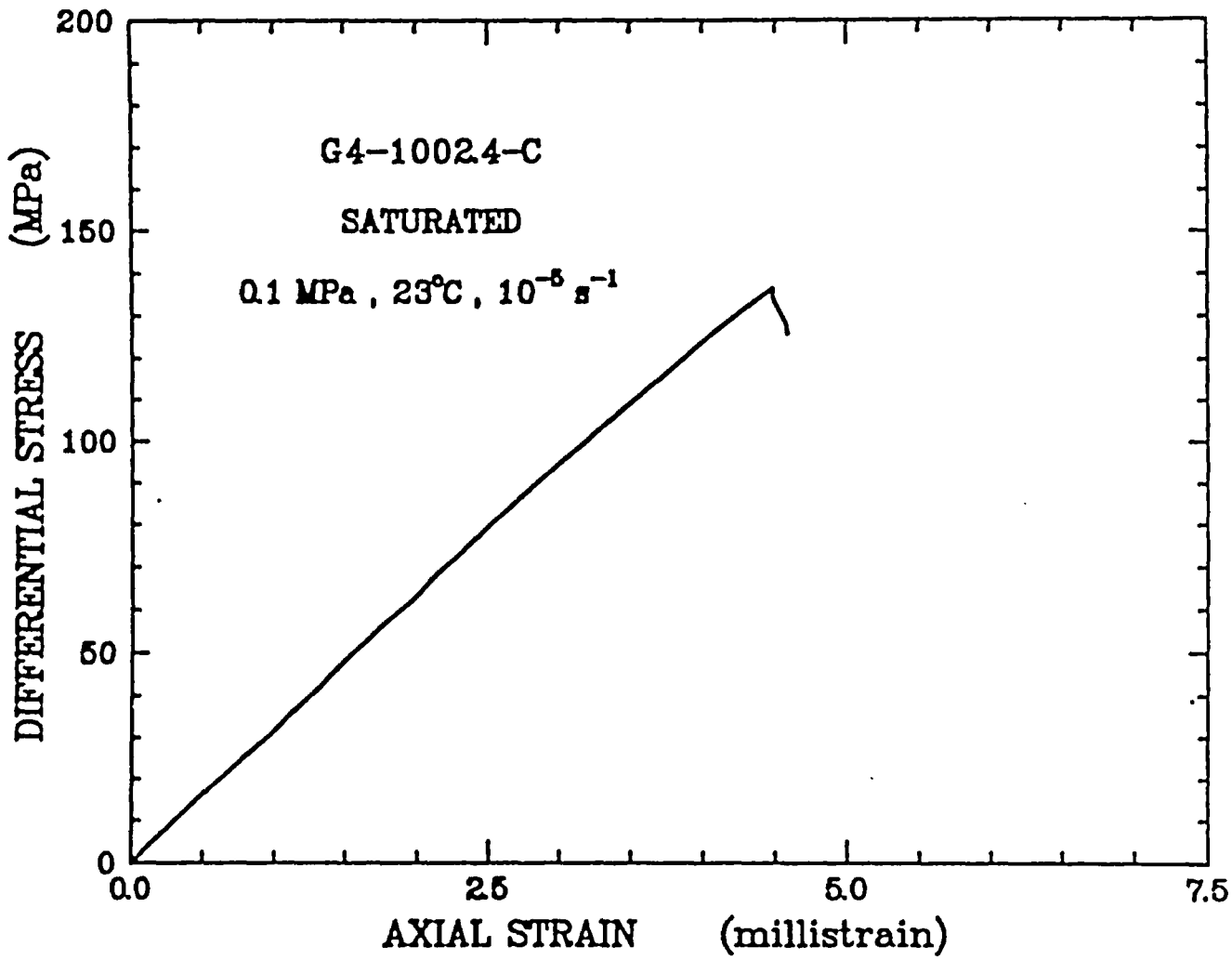

Figure 4hh.

Plot of axial stress versus axial strain for sample G4-1002.4-C, deformed in compression at 0.1 MPa confining pressure, room temperature, and a nominal axial strain rate of 10^{-5} s^{-1}.

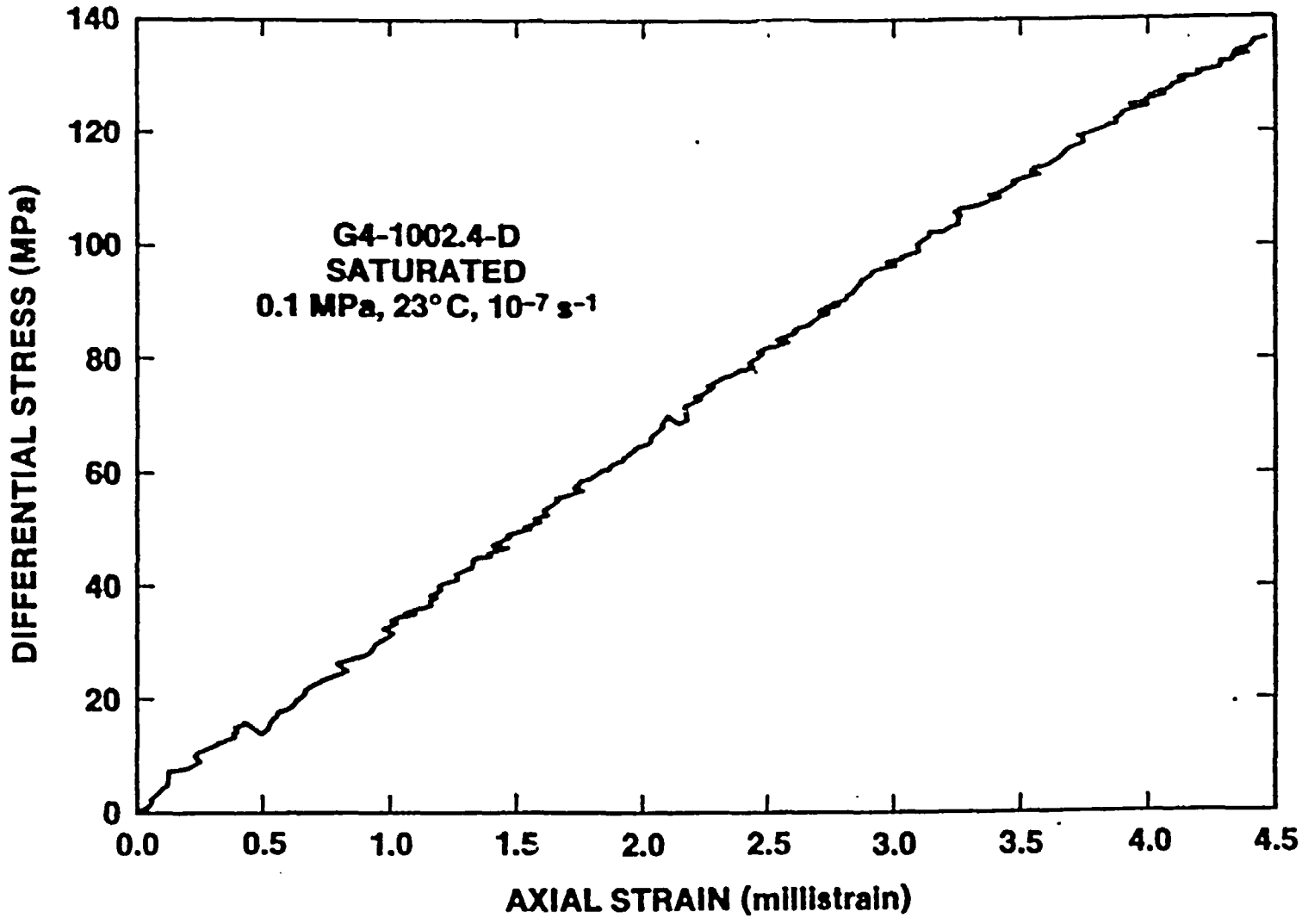

Figure 4ii.

Plot of axial stress versus axial strain for sample G4-1002.4-D, deformed in compression at 0.1 MPa confining pressure, room temperature, and a nominal axial strain rate of 10^{-7} s^{-1}.

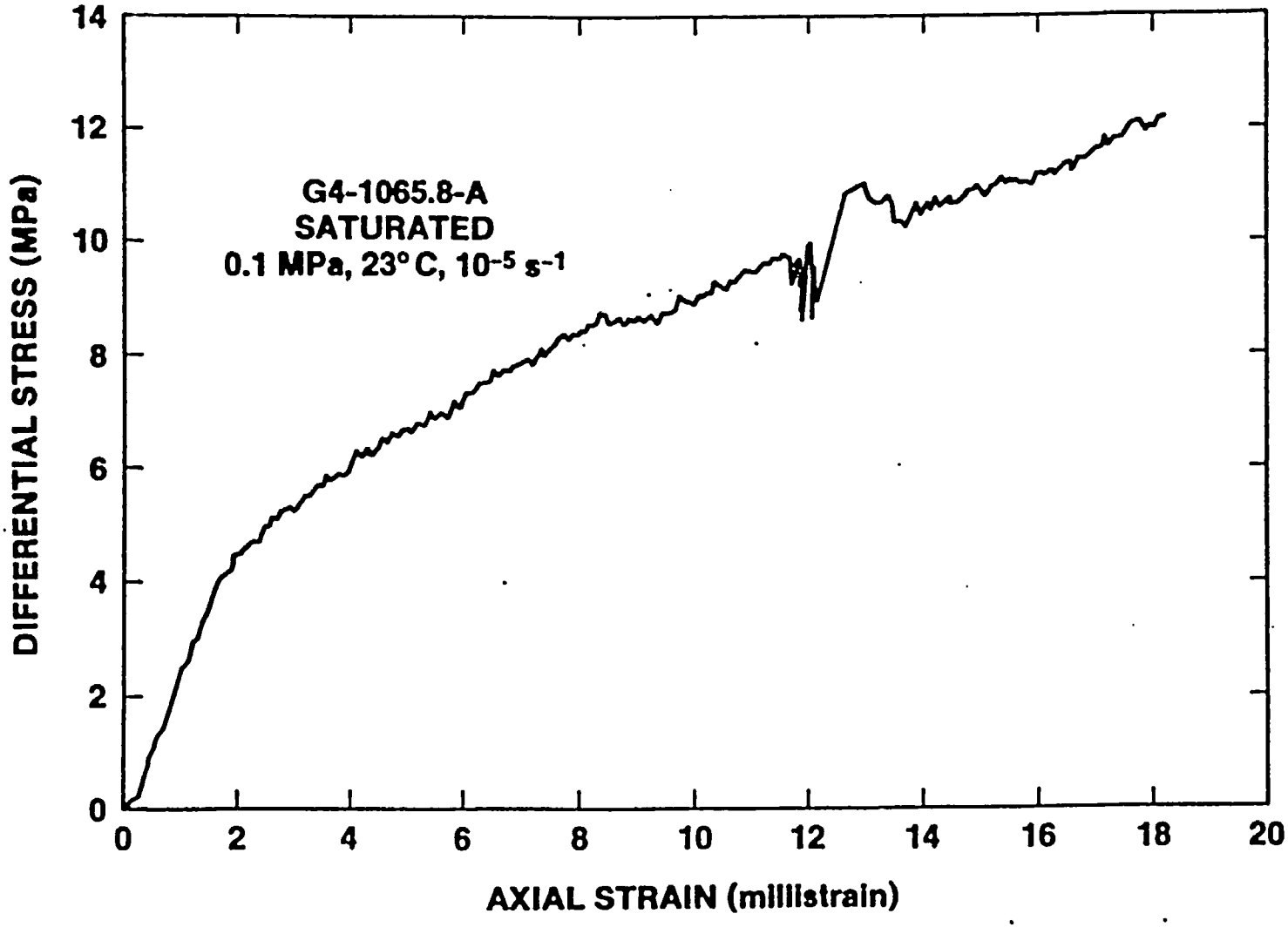

Figure 4jj.

Plot of axial stress versus axial strain for sample G4-1065.8-A, deformed in compression at 0.1 MPa confining pressure, room temperature, and a nominal axial strain rate of 10^{-5} s^{-1}.

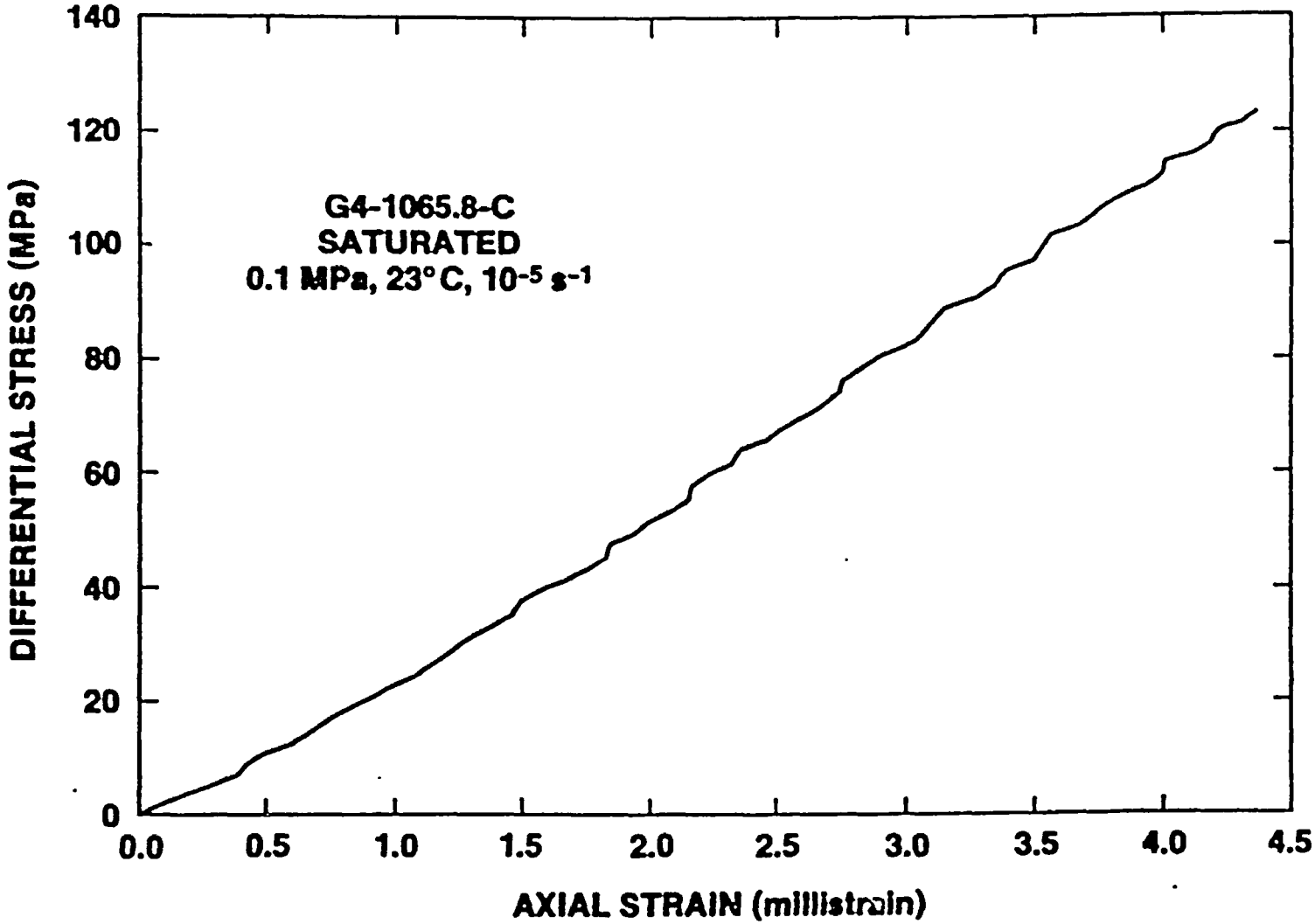

Figure 4kk.

Plot of axial stress versus axial strain for sample G4-1065.8-C, deformed in compression at 0.1 MPa confining pressure, room temperature, and a nominal axial strain rate of 10^{-5} s^{-1}.

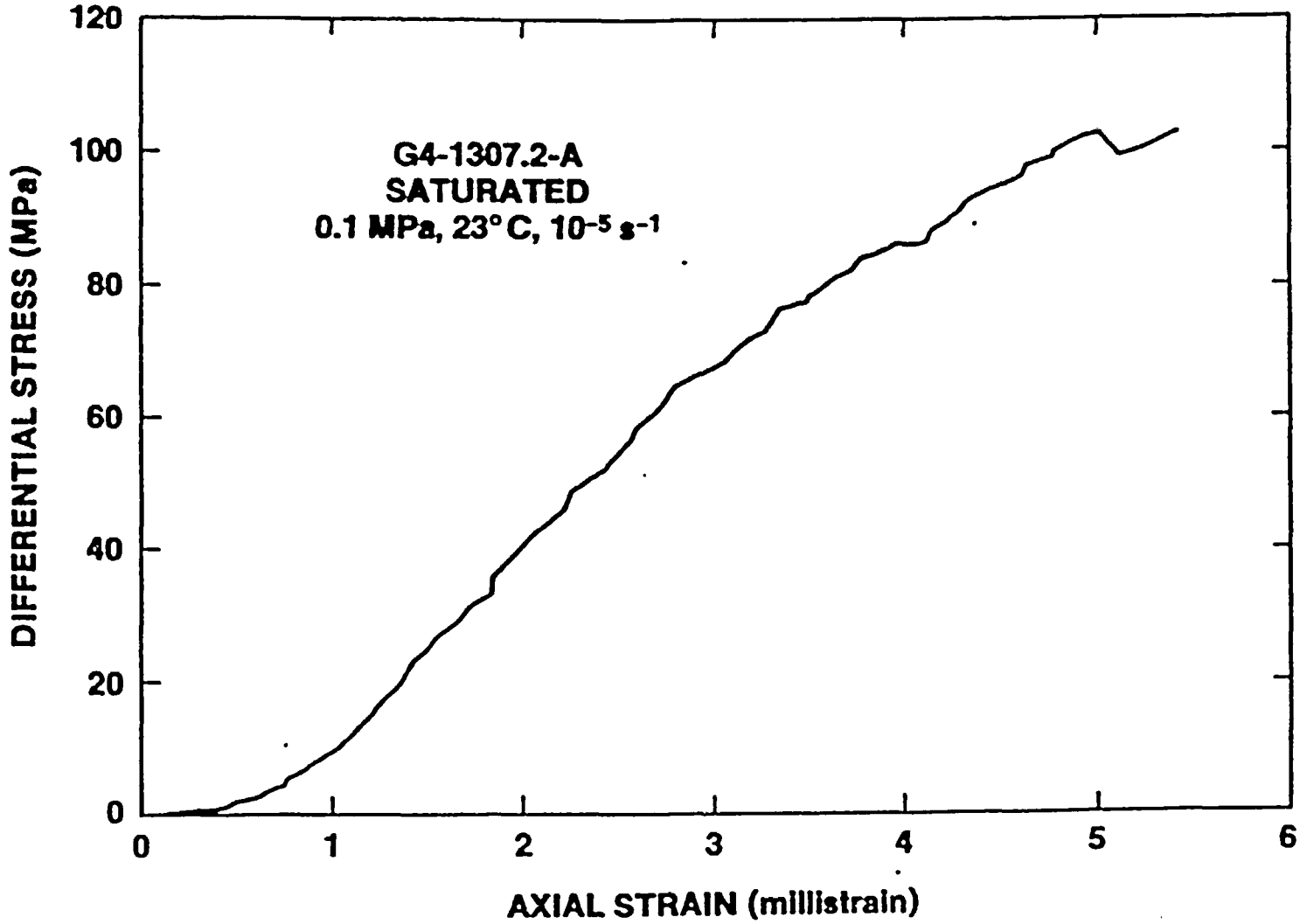

Figure 5a.

Plot of axial stress versus axial strain for sample G4-1307.2-A, deformed in compression at 0.1 MPa confining pressure, room temperature, and a nominal axial strain rate of 10^{-5} s^{-1}.

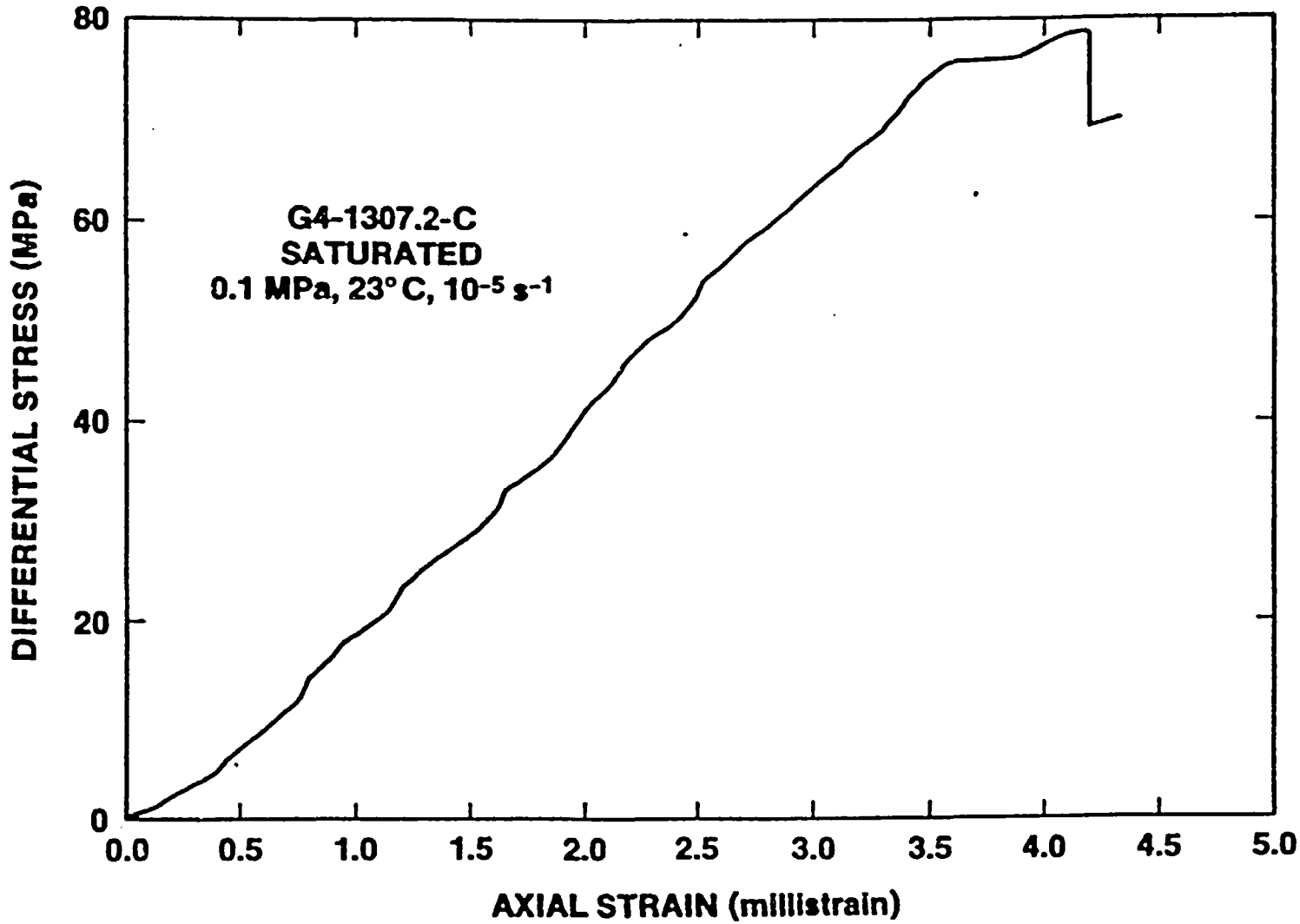

Figure 5b.

Plot of axial stress versus axial strain for sample G4-1307.2-C, deformed in compression at 0.1 MPa confining pressure, room temperature, and a nominal axial strain rate of 10^{-5} s^{-1}.

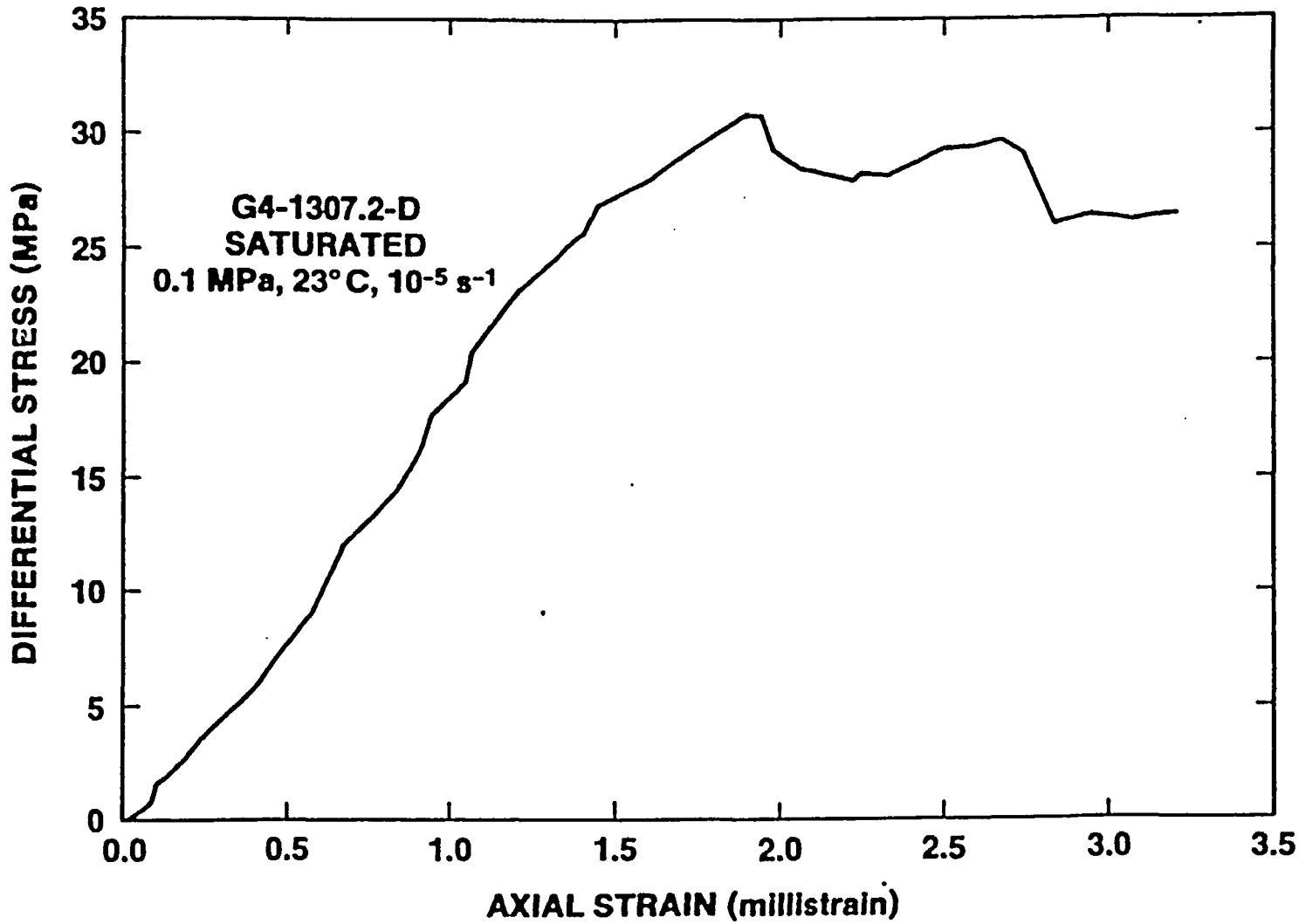

Figure 5c.

Plot of axial stress versus axial strain for sample G4-1307.2-D, deformed in compression at 0.1 MPa confining pressure, room temperature, and a nominal axial strain rate of 10^{-5} s^{-1}.

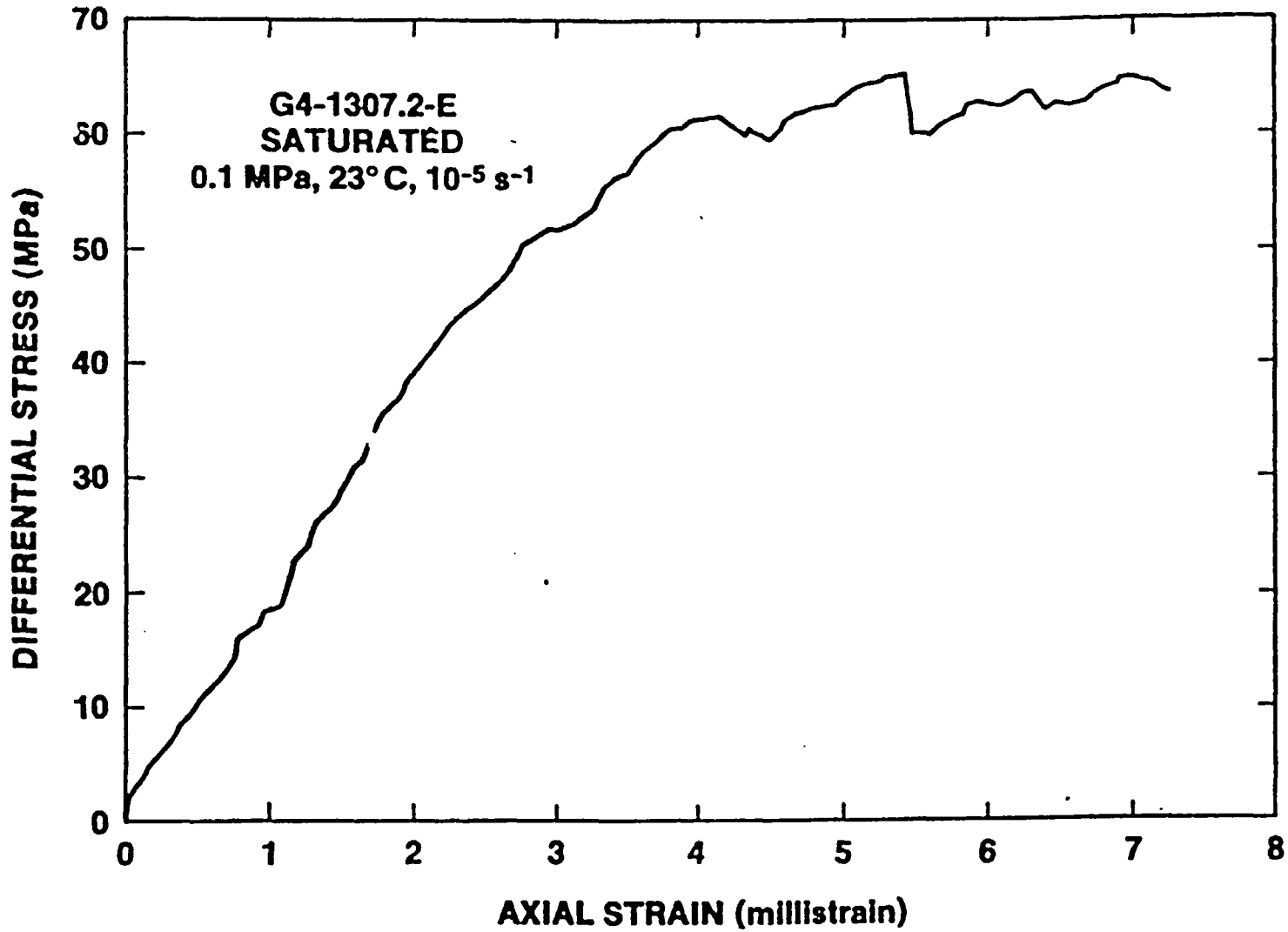

Figure 5d.

Plot of axial stress versus axial strain for sample G4-1307.2-E, deformed in compression at 0.1 MPa confining pressure, room temperature, and a nominal axial strain rate of 10^{-5} s^{-1}.

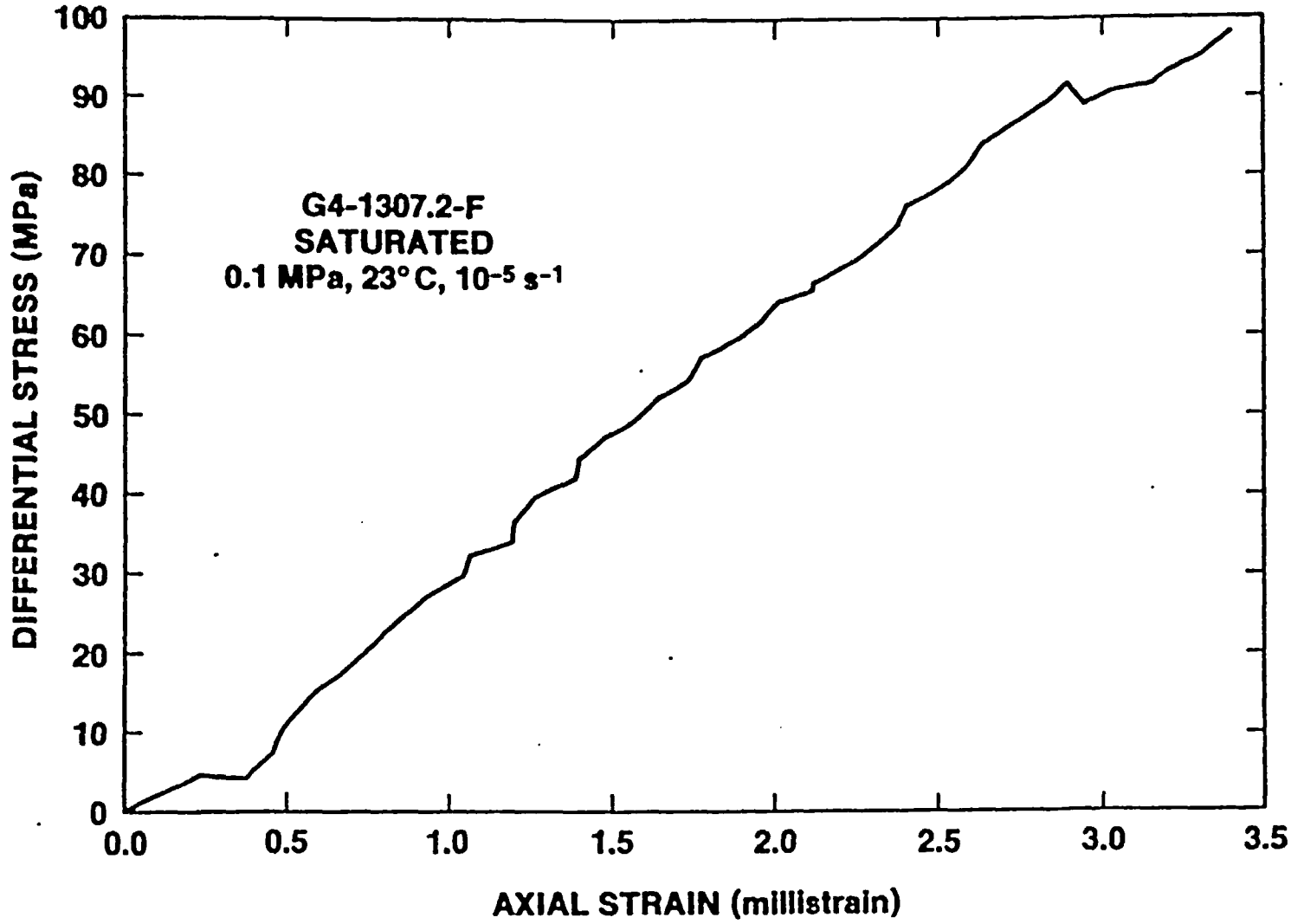

Figure 5e.

Plot of axial stress versus axial strain for sample G4-1307.2-F, deformed in compression at 0.1 MPa confining pressure, room temperature, and a nominal axial strain rate of 10^{-5} s^{-1}.

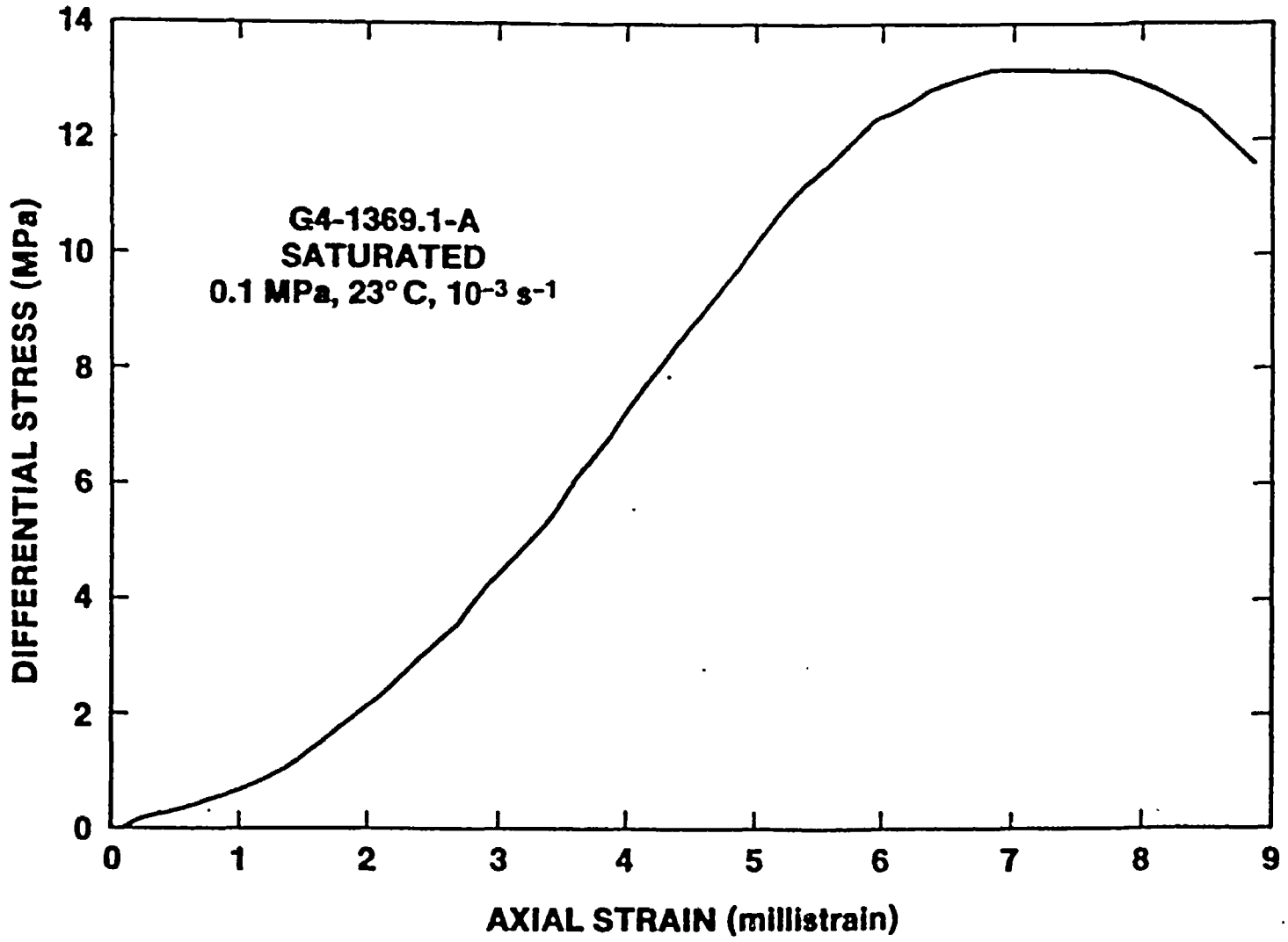

Figure 6a.

Plot of axial stress versus axial strain for sample G4-1369.1-A, deformed in compression at 0.1 MPa confining pressure, room temperature, and a nominal axial strain rate of 10^{-3} s^{-1}.

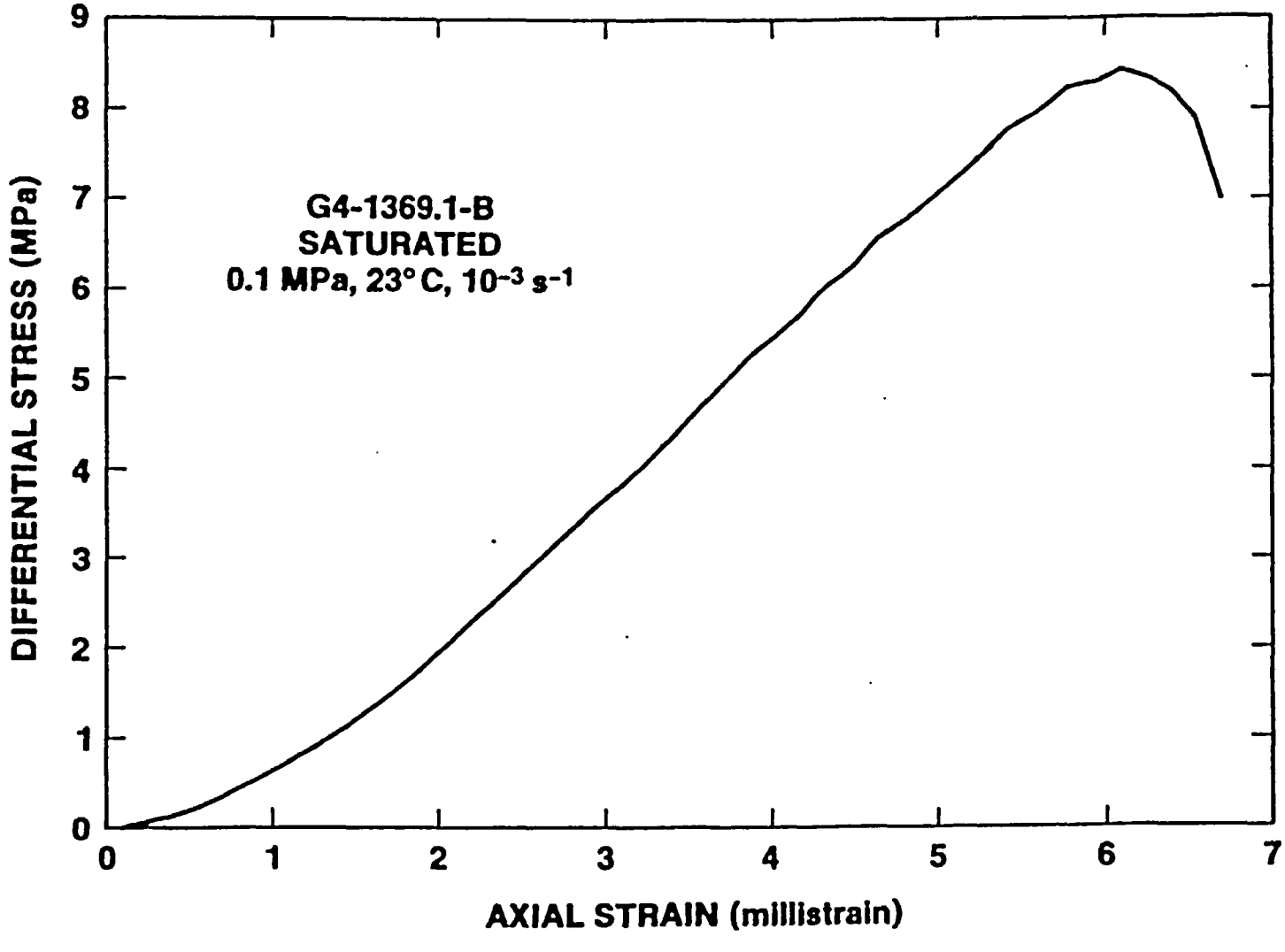

Figure 6b.

Plot of axial stress versus axial strain for sample G4-1369.1-B, deformed in compression at 0.1 MPa confining pressure, room temperature, and a nominal axial strain rate of 10^{-3} s^{-1}.

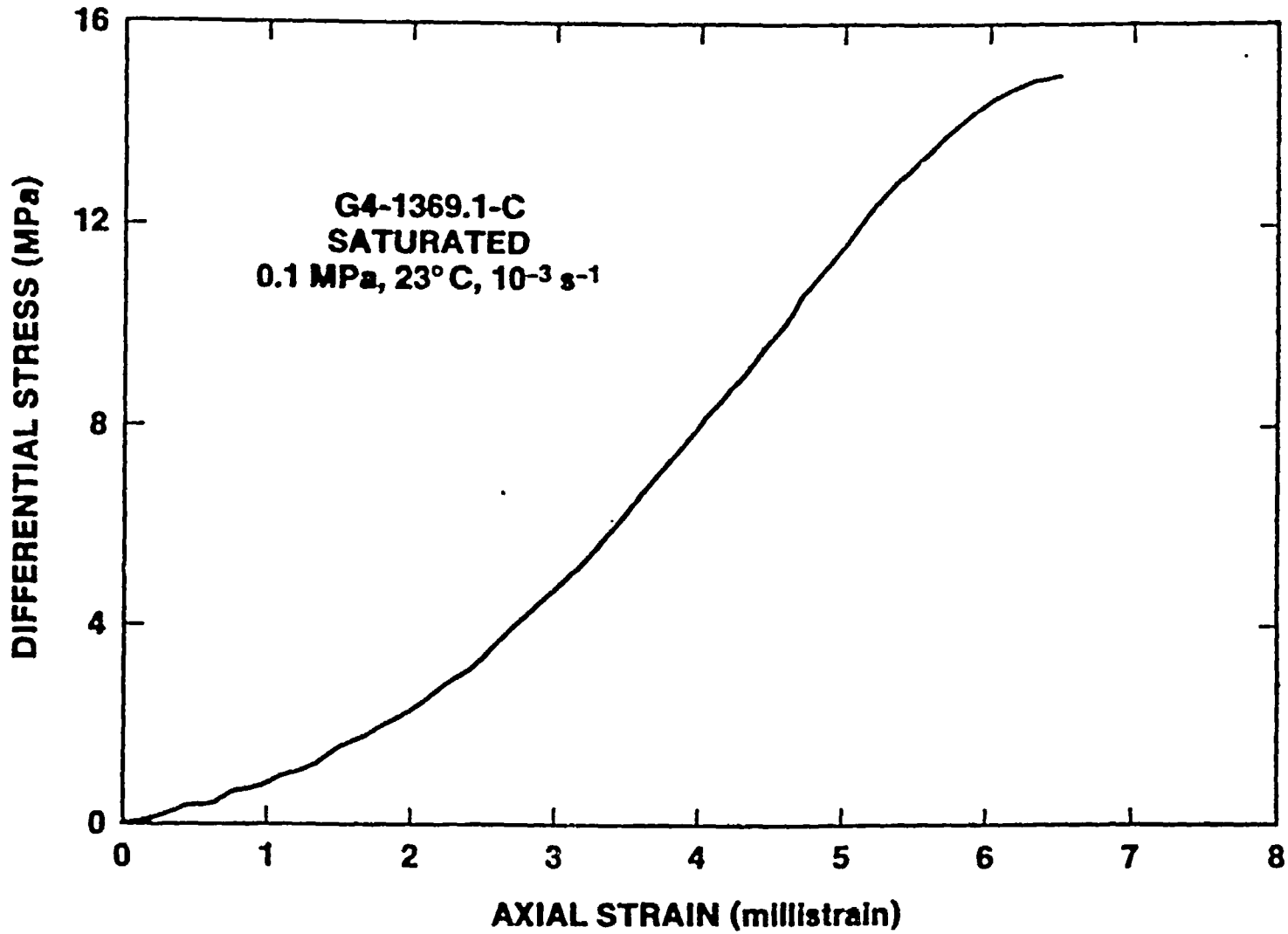

Figure 6c.

Plot of axial stress versus axial strain for sample G4-1369.1-C, deformed in compression at 0.1 MPa confining pressure, room temperature, and a nominal axial strain rate of 10^{-3} s^{-1}.

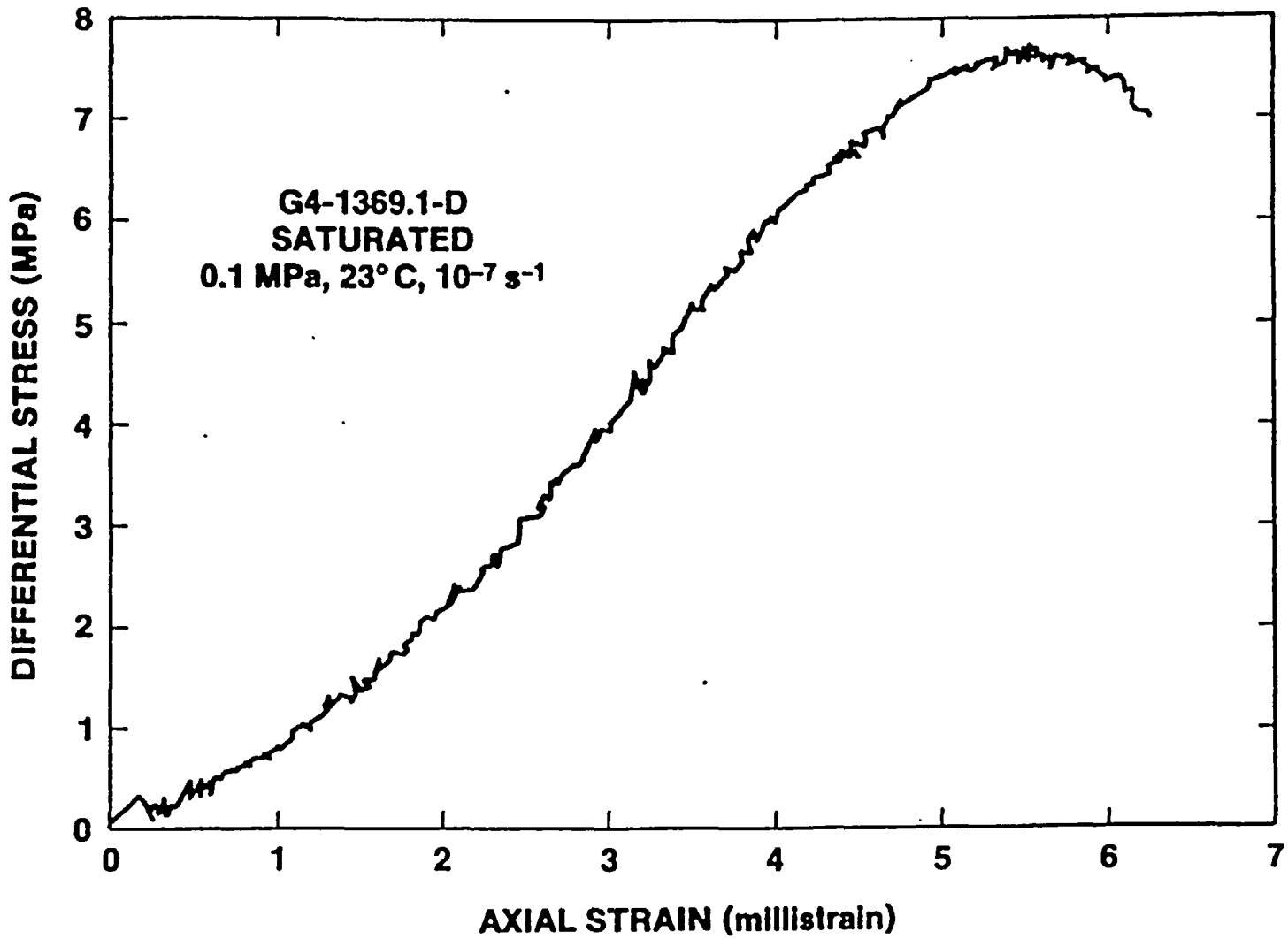

Figure 6d.

Plot of axial stress versus axial strain for sample G4-1369.1-D, deformed in compression at 0.1 MPa confining pressure, room temperature, and a nominal axial strain rate of 10^{-7} s^{-1}.

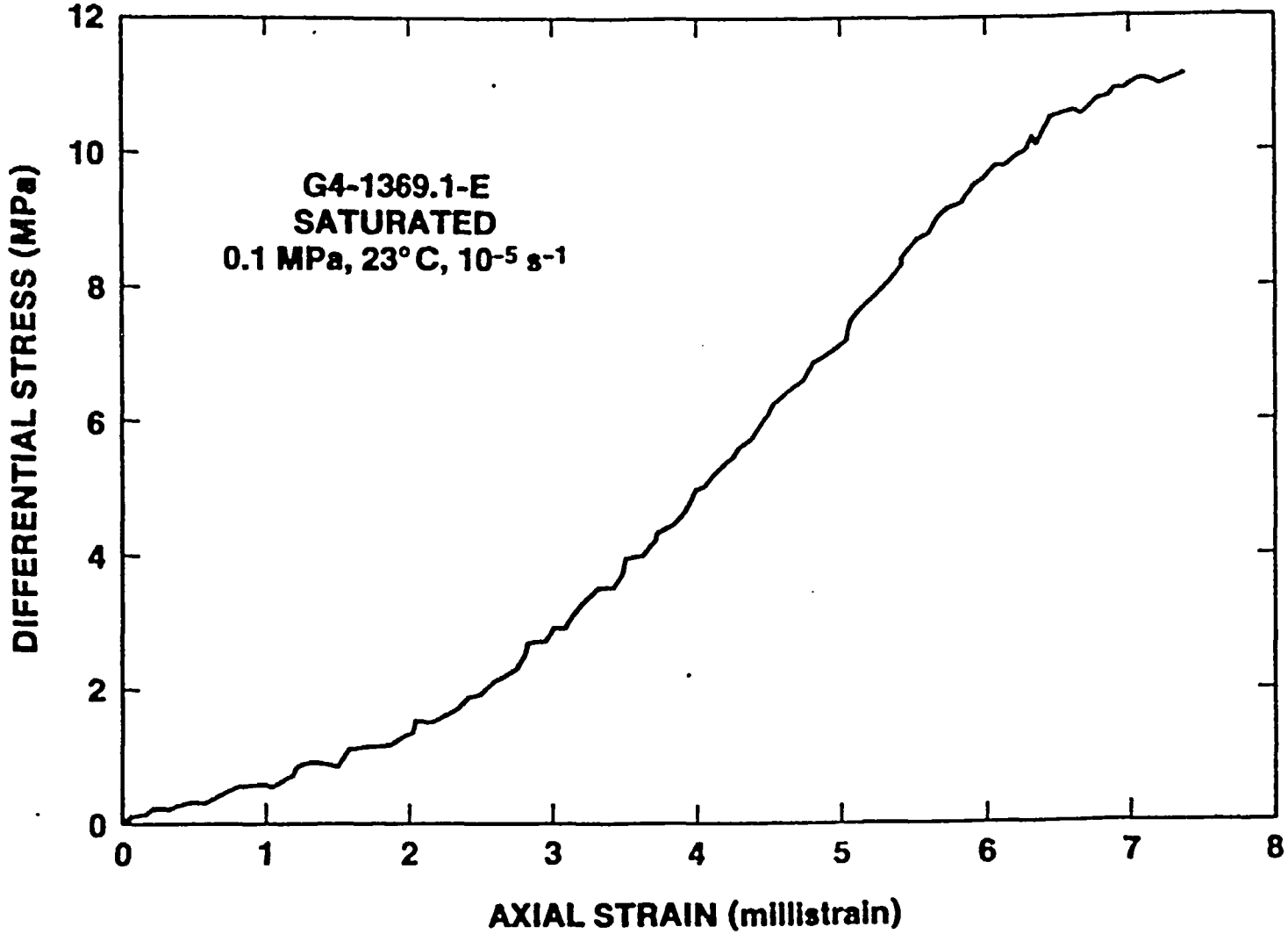

Figure 6e.

Plot of axial stress versus axial strain for sample G4-1369.1-E, deformed in compression at 0.1 MPa confining pressure, room temperature, and a nominal axial strain rate of 10^{-5} s^{-1}.

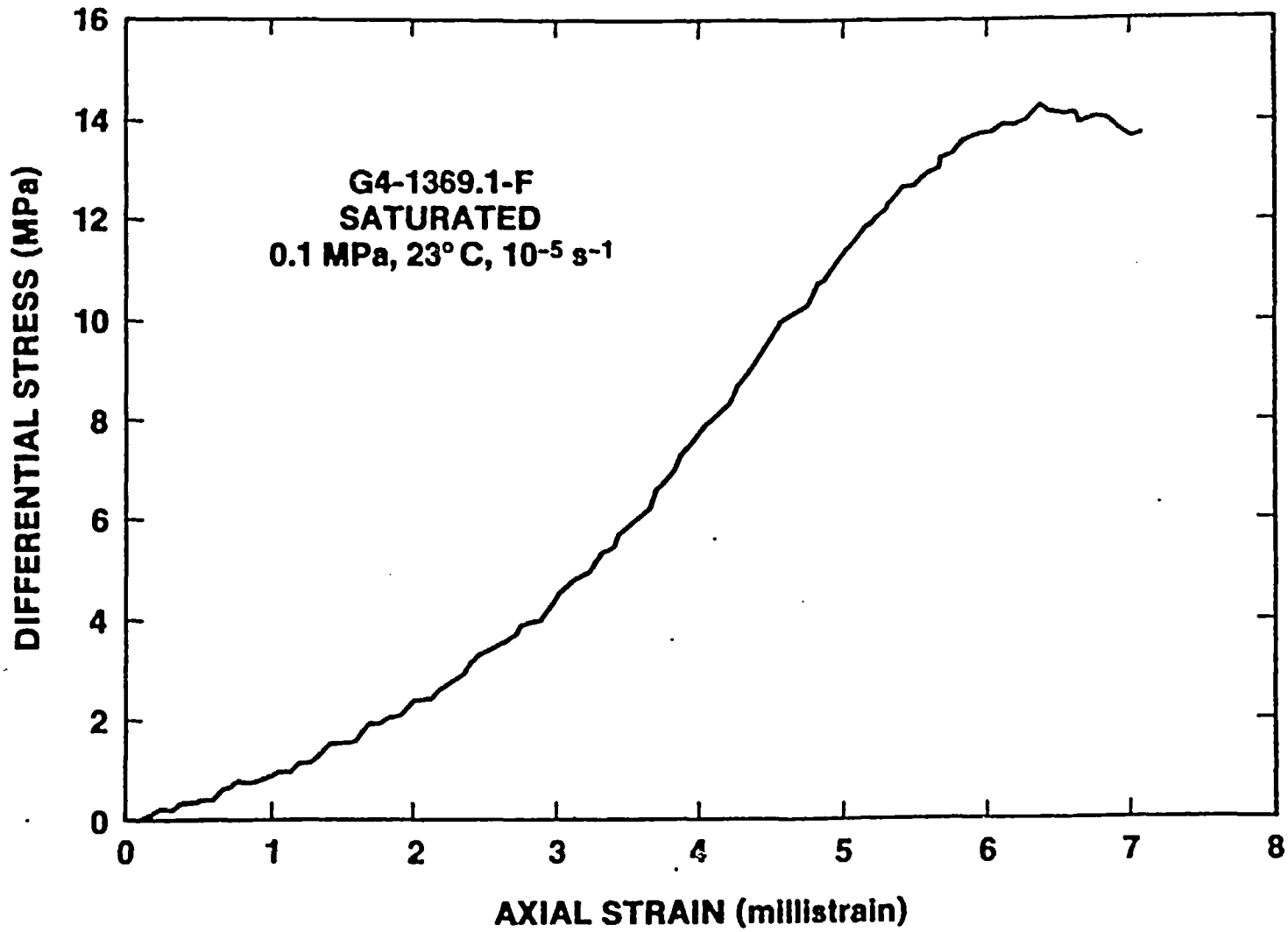

Figure 6f.

Plot of axial stress versus axial strain for sample G4-1369.1-F, deformed in compression at 0.1 MPa confining pressure, room temperature, and a nominal axial strain rate of 10^{-5} s^{-1}.

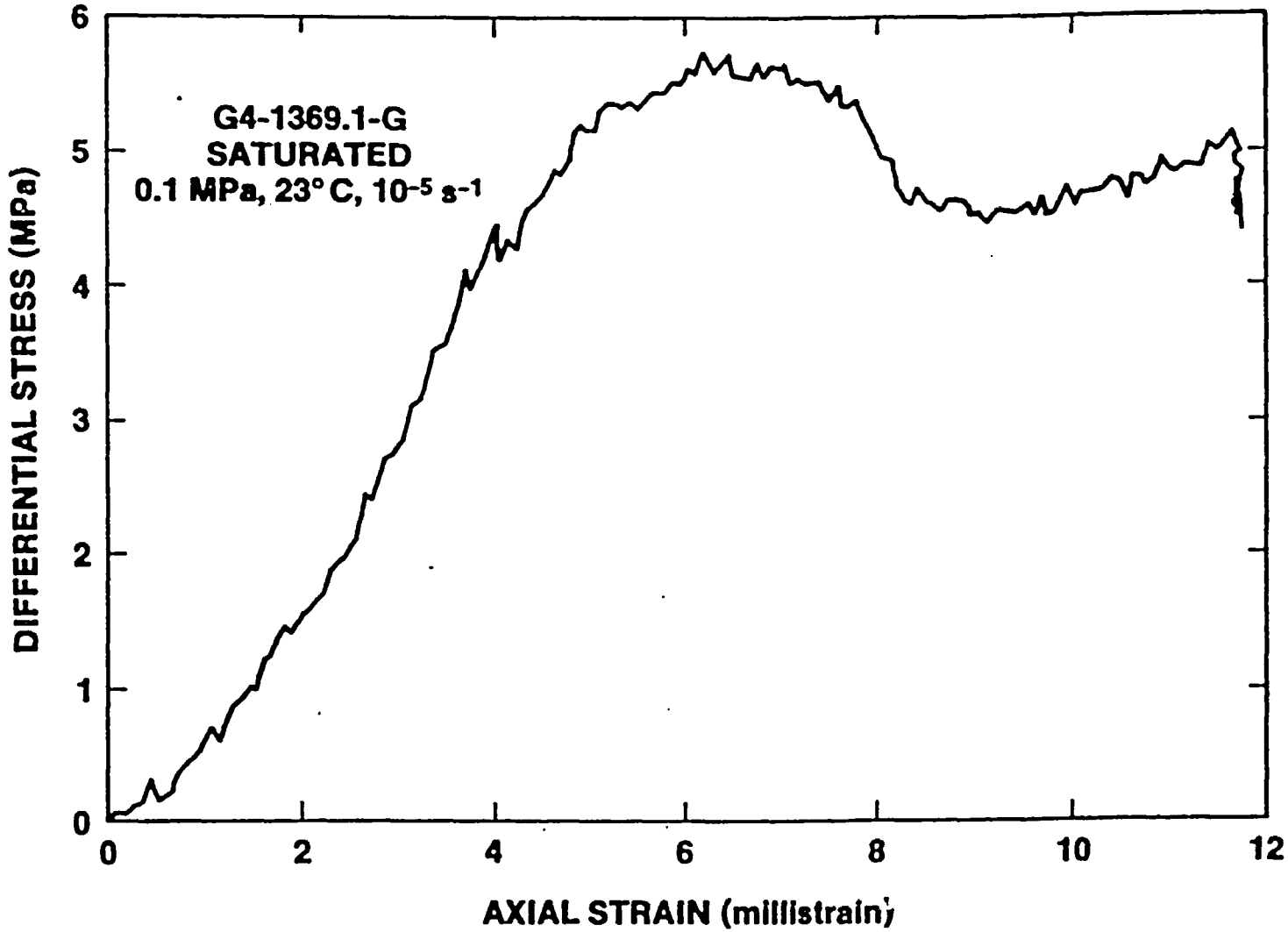

Figure 6g.

Plot of axial stress versus axial strain for sample G4-1369.1-G, deformed in compression at 0.1 MPa confining pressure, room temperature, and a nominal axial strain rate of 10^{-5} s^{-1}.

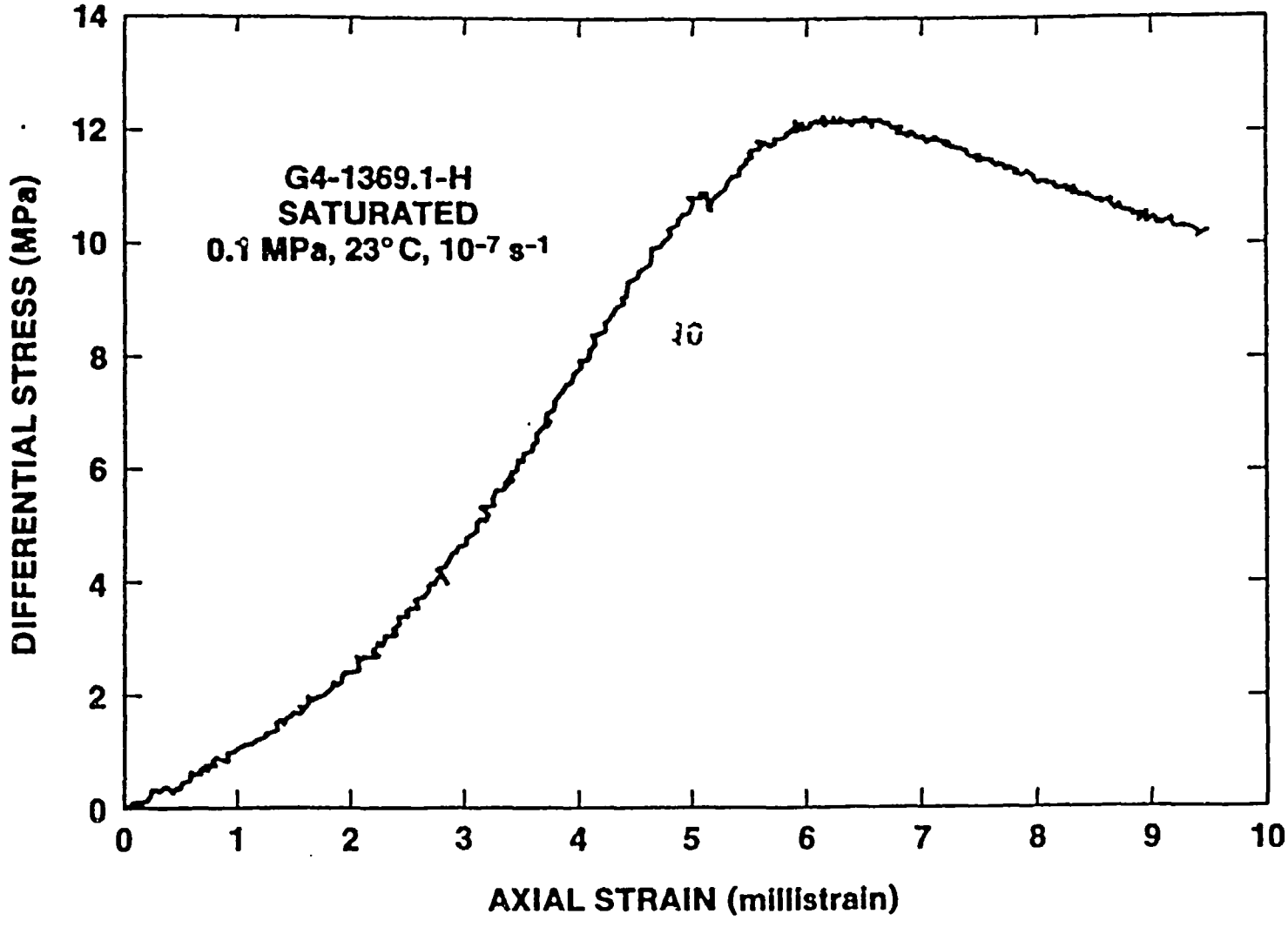

Figure 6h.

Plot of axial stress versus axial strain for sample G4-1369.1-H, deformed in compression at 0.1 MPa confining pressure, room temperature, and a nominal axial strain rate of 10^{-7} s^{-1}.

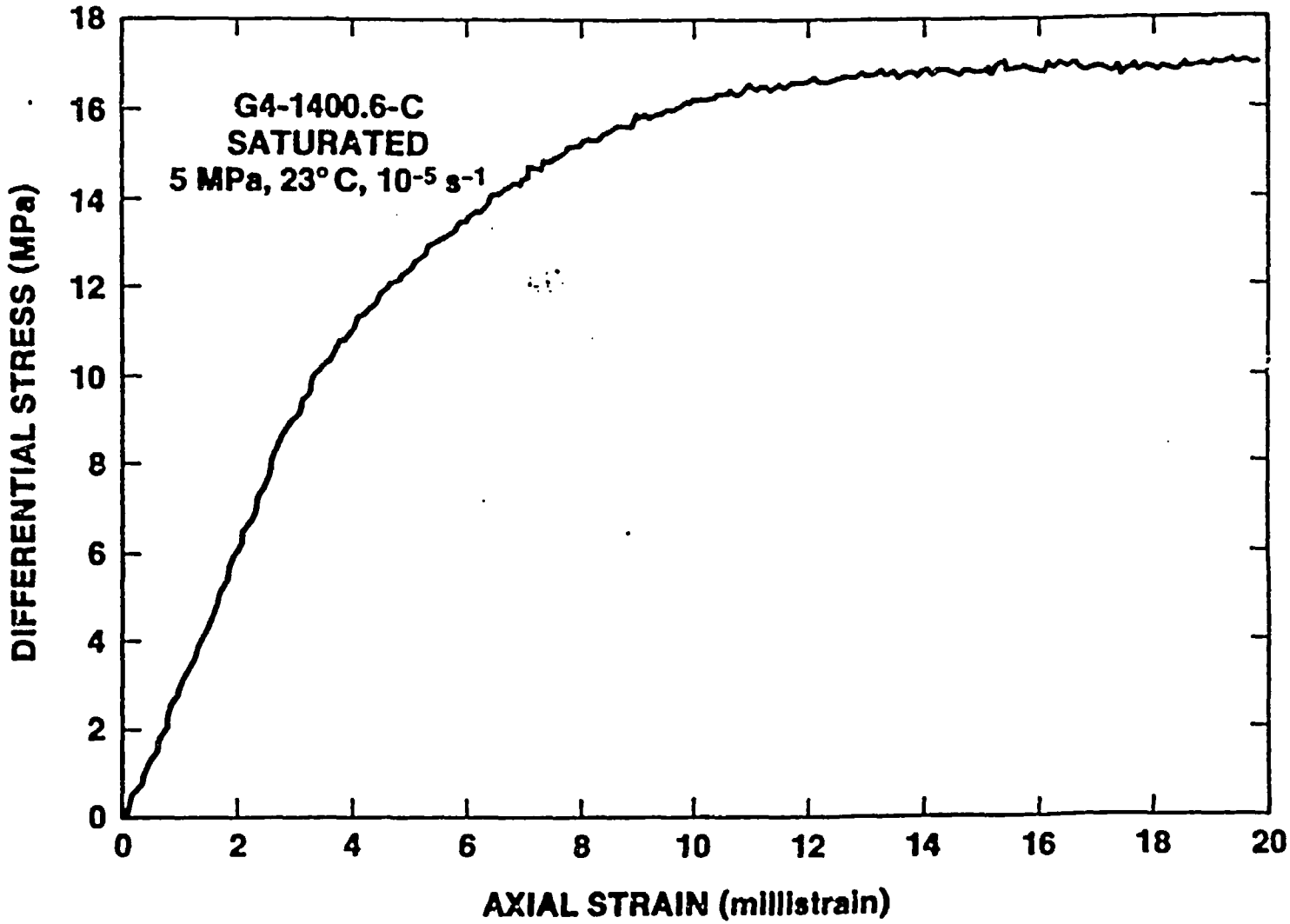

Figure 7a.

Plot of axial stress versus axial strain for sample G4-1400.6-C, deformed in compression at 5 MPa confining pressure, room temperature, and a nominal axial strain rate of 10^{-5} s^{-1}.

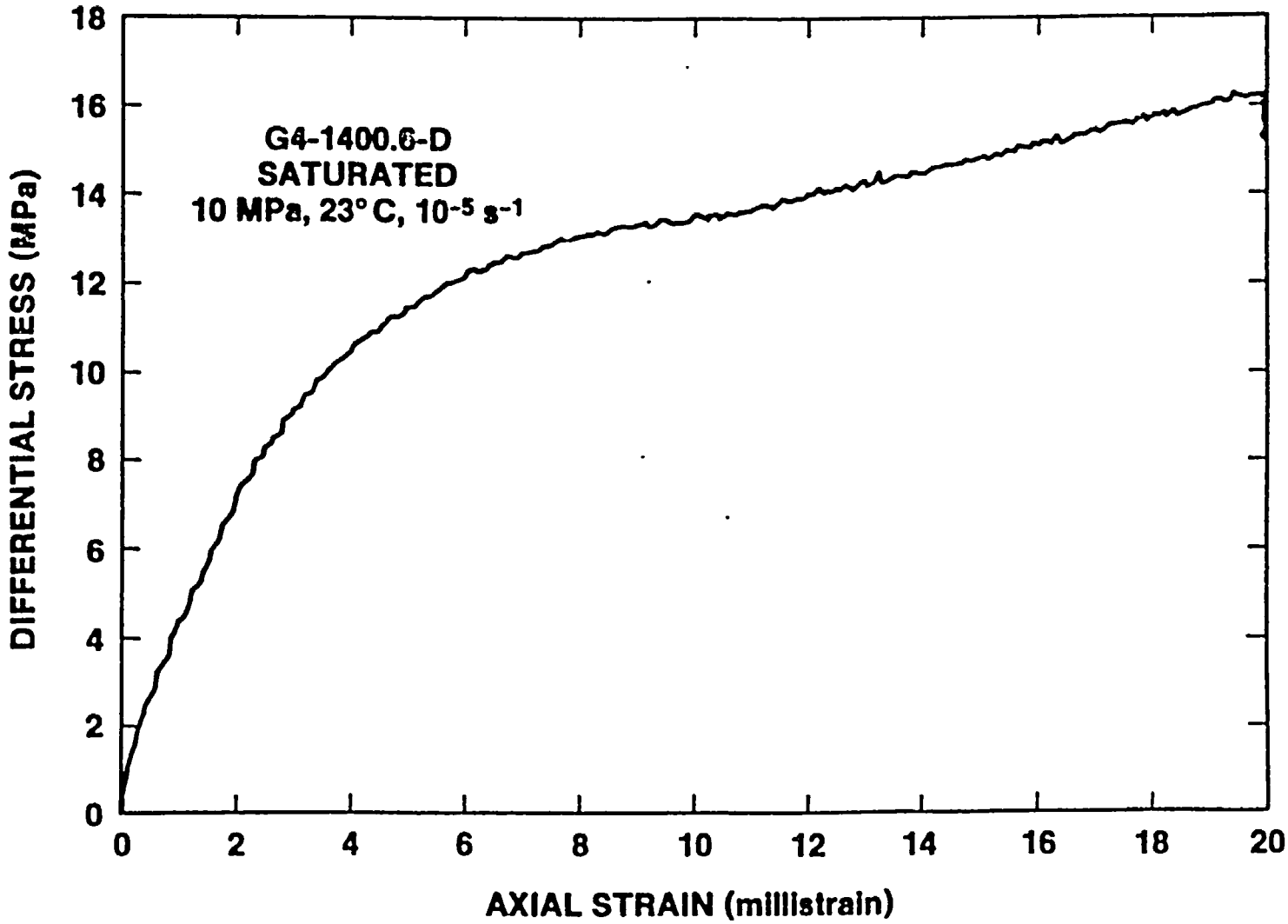

Figure 7b.

Plot of axial stress versus axial strain for sample G4-1400.6-D, deformed in compression at 10 MPa confining pressure, room temperature, and a nominal axial strain rate of 10^{-5} s^{-1}.

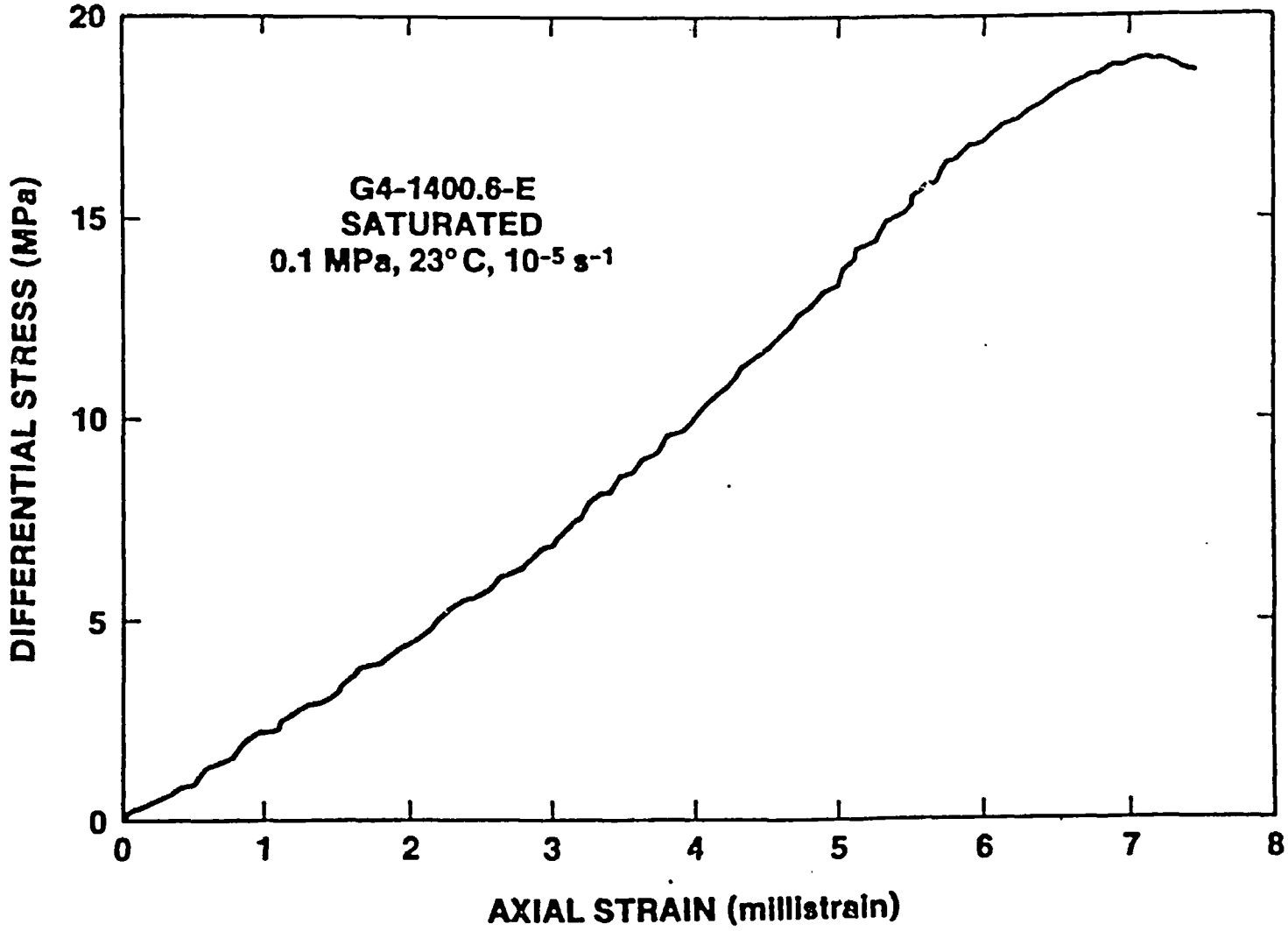

Figure 7c.

Plot of axial stress versus axial strain for sample G4-1400.6-E, deformed in compression at 0.1 MPa confining pressure, room temperature, and a nominal axial strain rate of 10^{-5} s^{-1}.

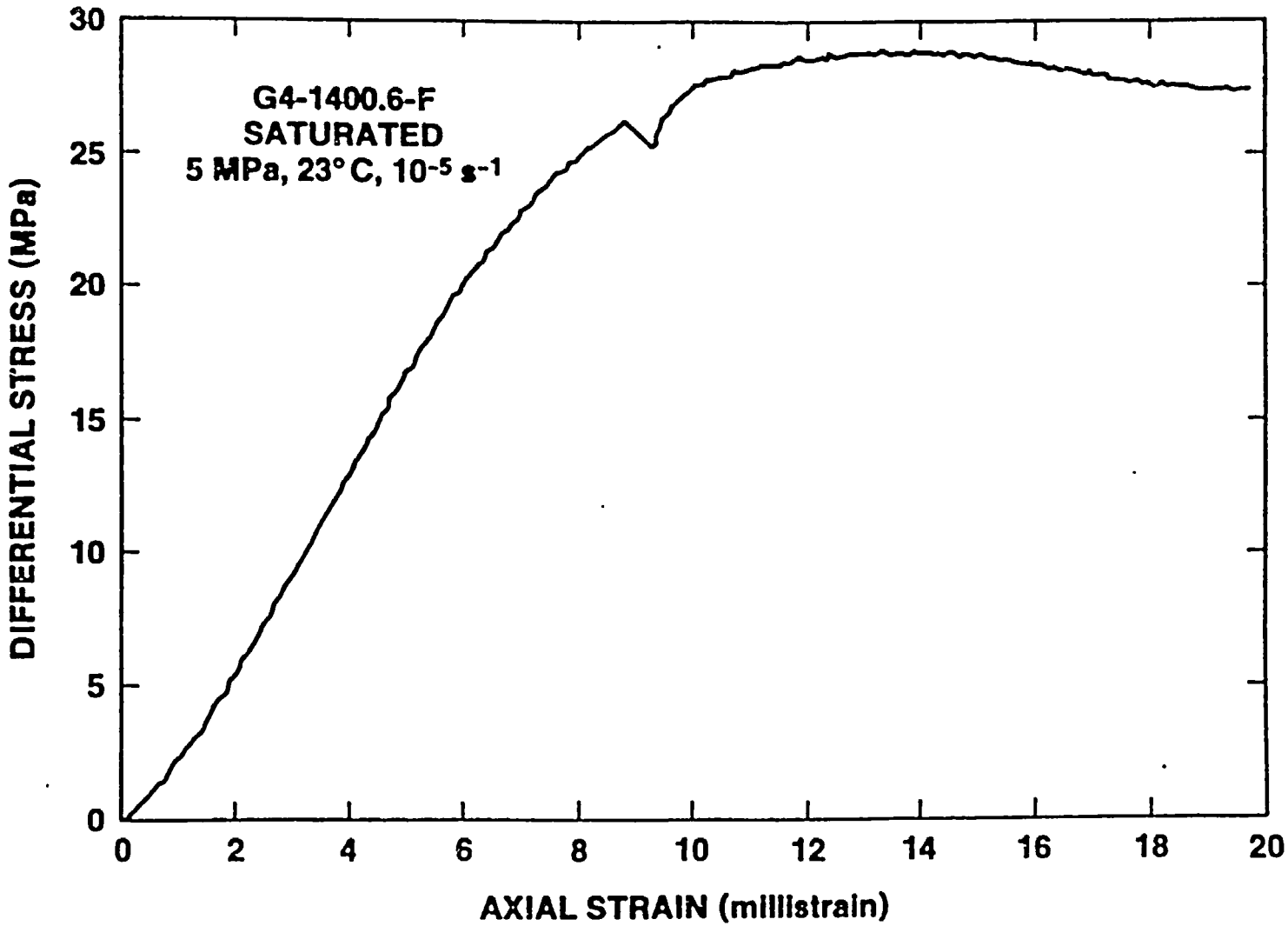

Figure 7d.

Plot of axial stress versus axial strain for sample G4-1400.6-F, deformed in compression at 5 MPa confining pressure, room temperature, and a nominal axial strain rate of 10^{-5} s^{-1}.

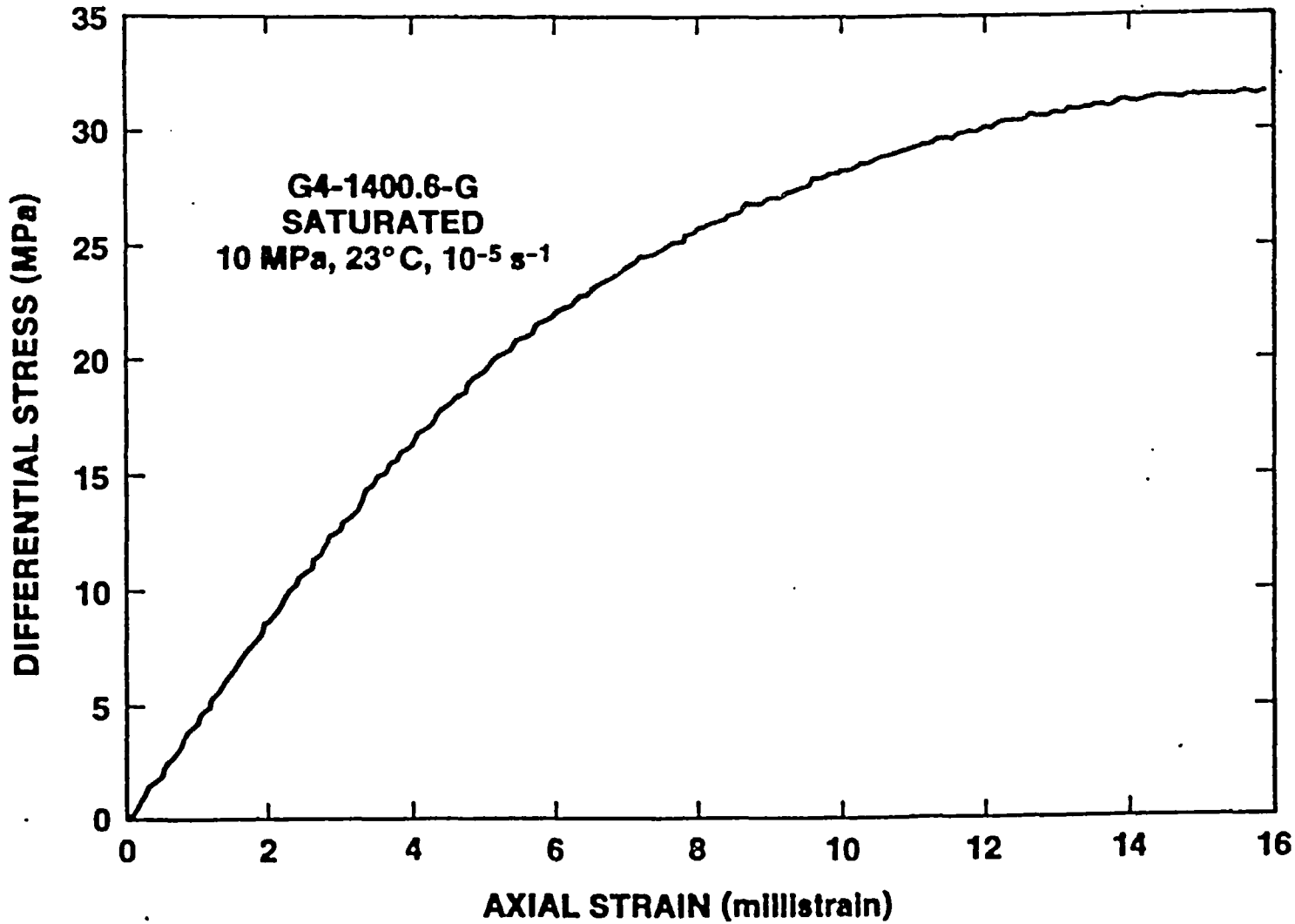

Figure 7e.

Plot of axial stress versus axial strain for sample G4-1400.6-G, deformed in compression at 10 MPa confining pressure, room temperature, and a nominal axial strain rate of 10^{-5} s^{-1}.

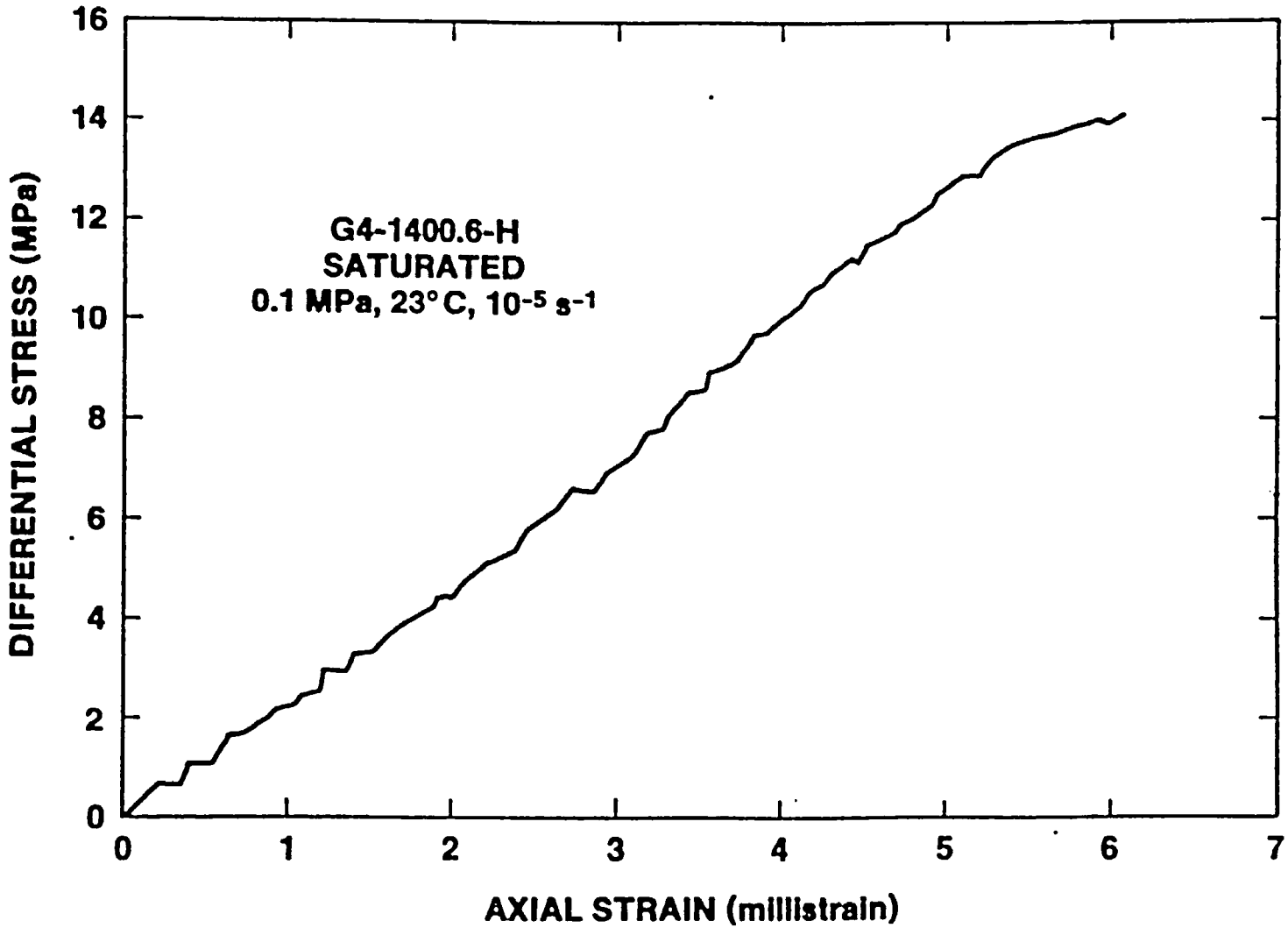

Figure 7f.

Plot of axial stress versus axial strain for sample G4-1400.6-H, deformed in compression at 0.1 MPa confining pressure, room temperature, and a nominal axial strain rate of 10^{-5} s^{-1}.

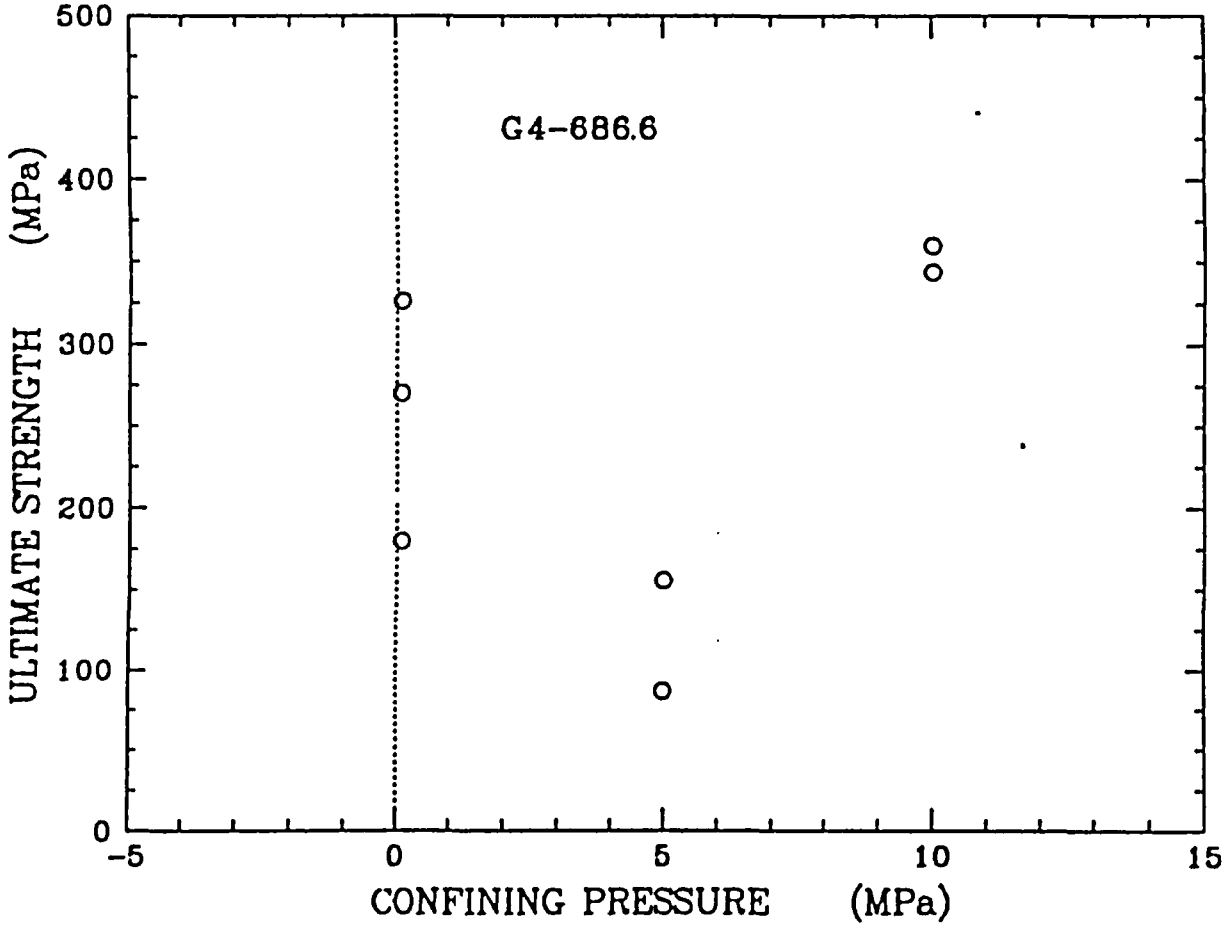

Figure 8a.

Plot of confining pressure versus ultimate differential stress for samples G4-686.6 deformed in compression at room temperature and a nominal axial strain rate of 10^{-5} s^{-1}.

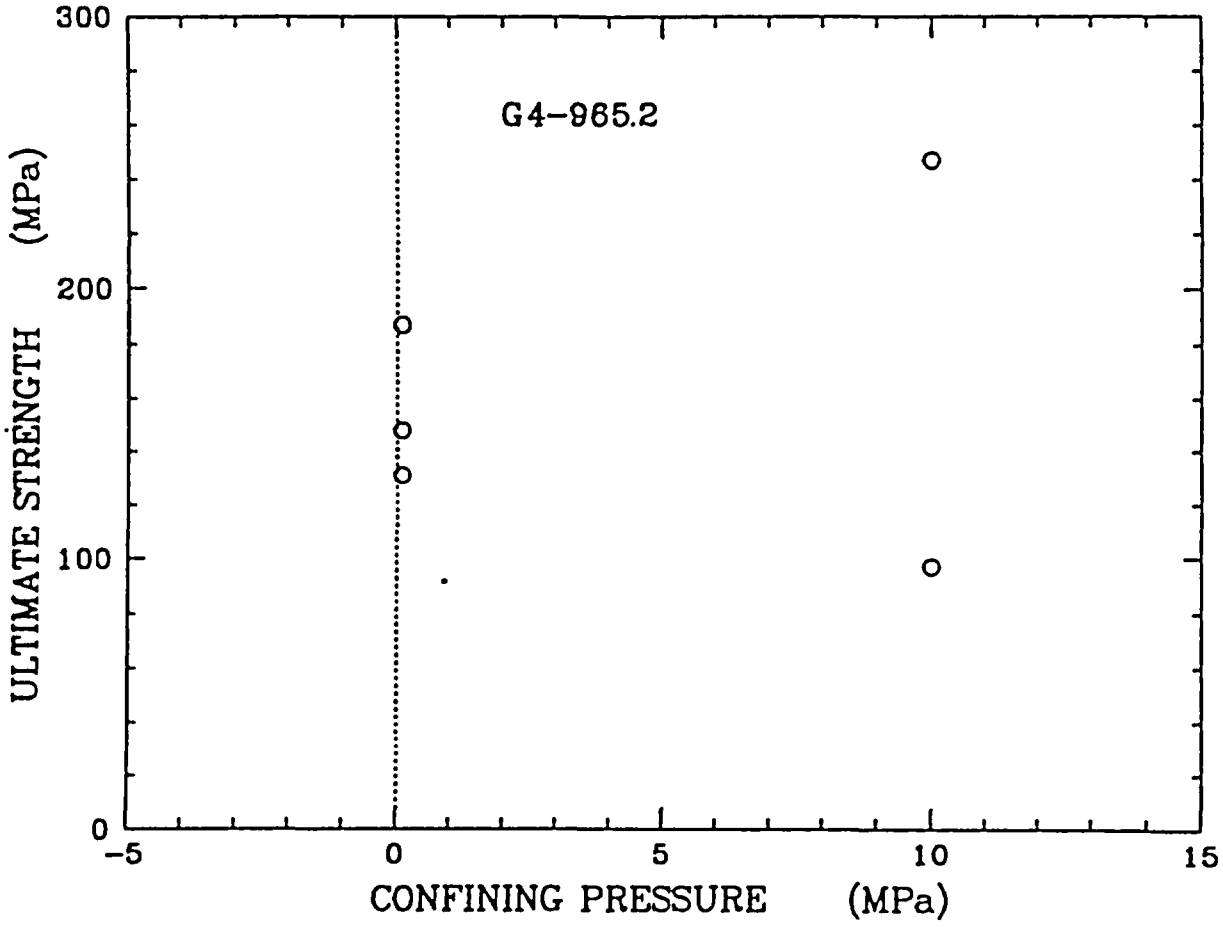

Figure 8b.

Plot of confining pressure versus ultimate differential stress for samples G4-965.2 deformed in compression at room temperature and a nominal axial strain rate of 10^{-5} s^{-1}.

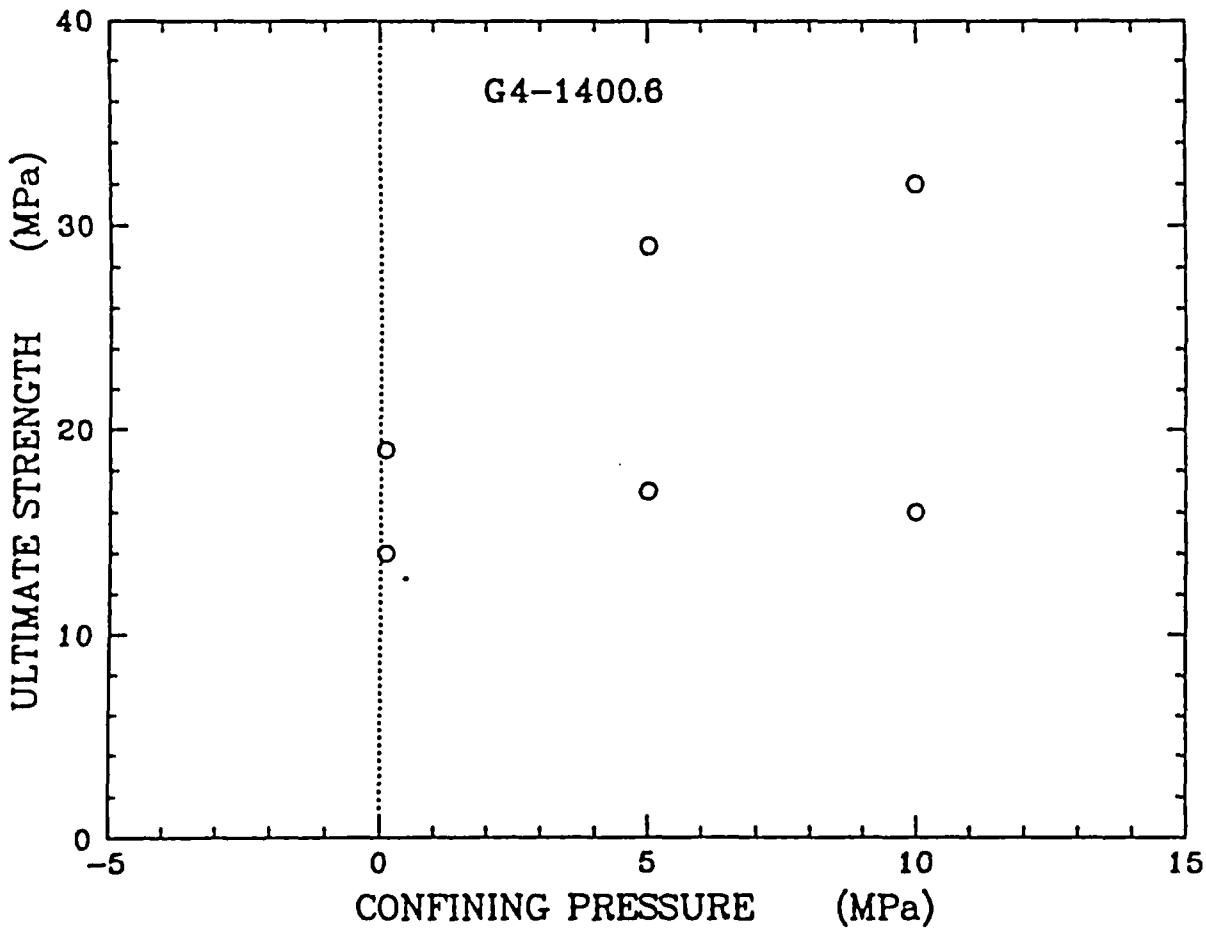

Figure 8c.

Plot of confining pressure versus ultimate differential stress for samples G4-1400.6 deformed in compression at room temperature and a nominal axial strain rate of $10^{-5}\ s^{-1}$.

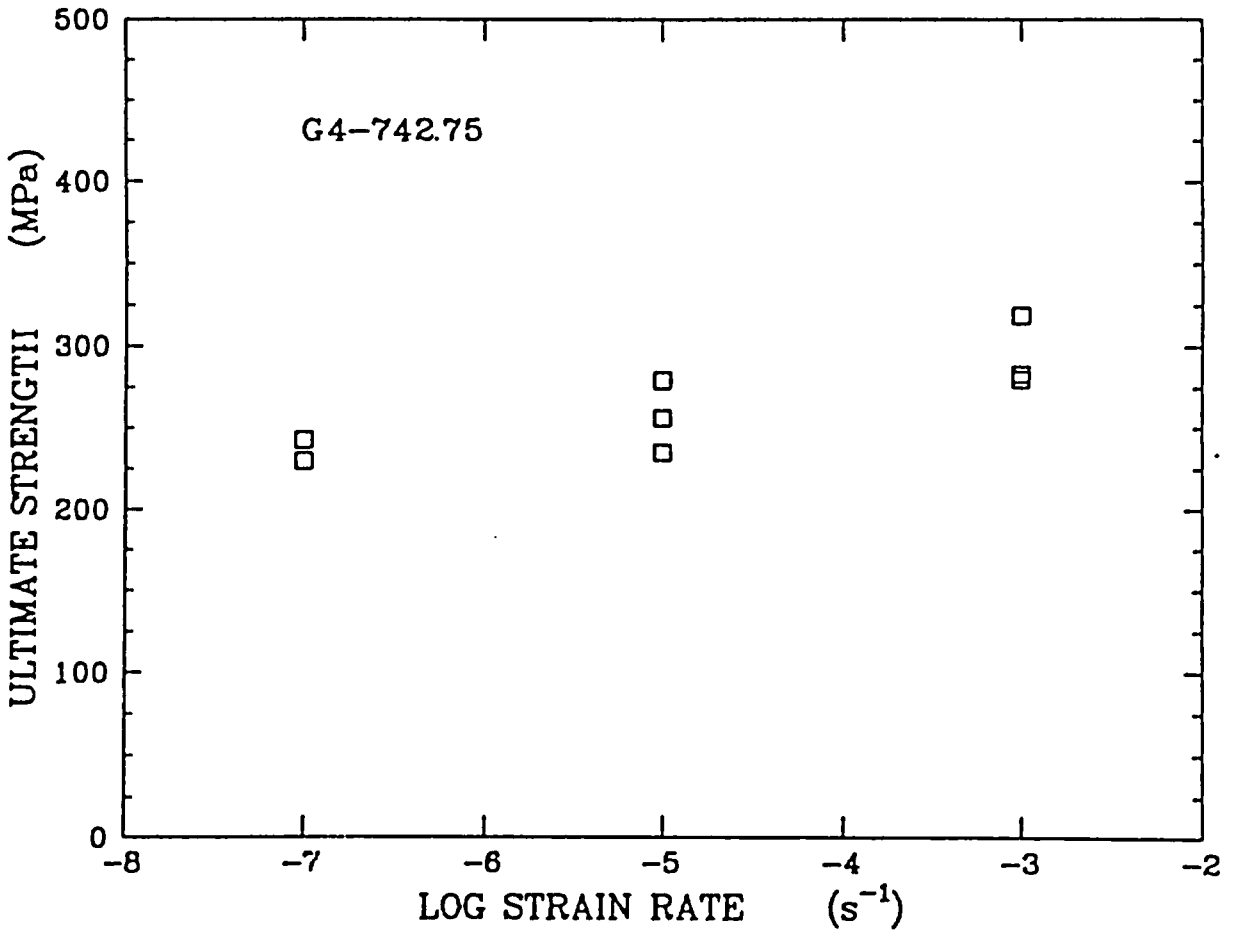

Figure 9a.

Plot of log strain rate versus ultimate differential stress for samples G4-742.75 deformed in compression at 0.1 MPa confining pressure and room temperature.

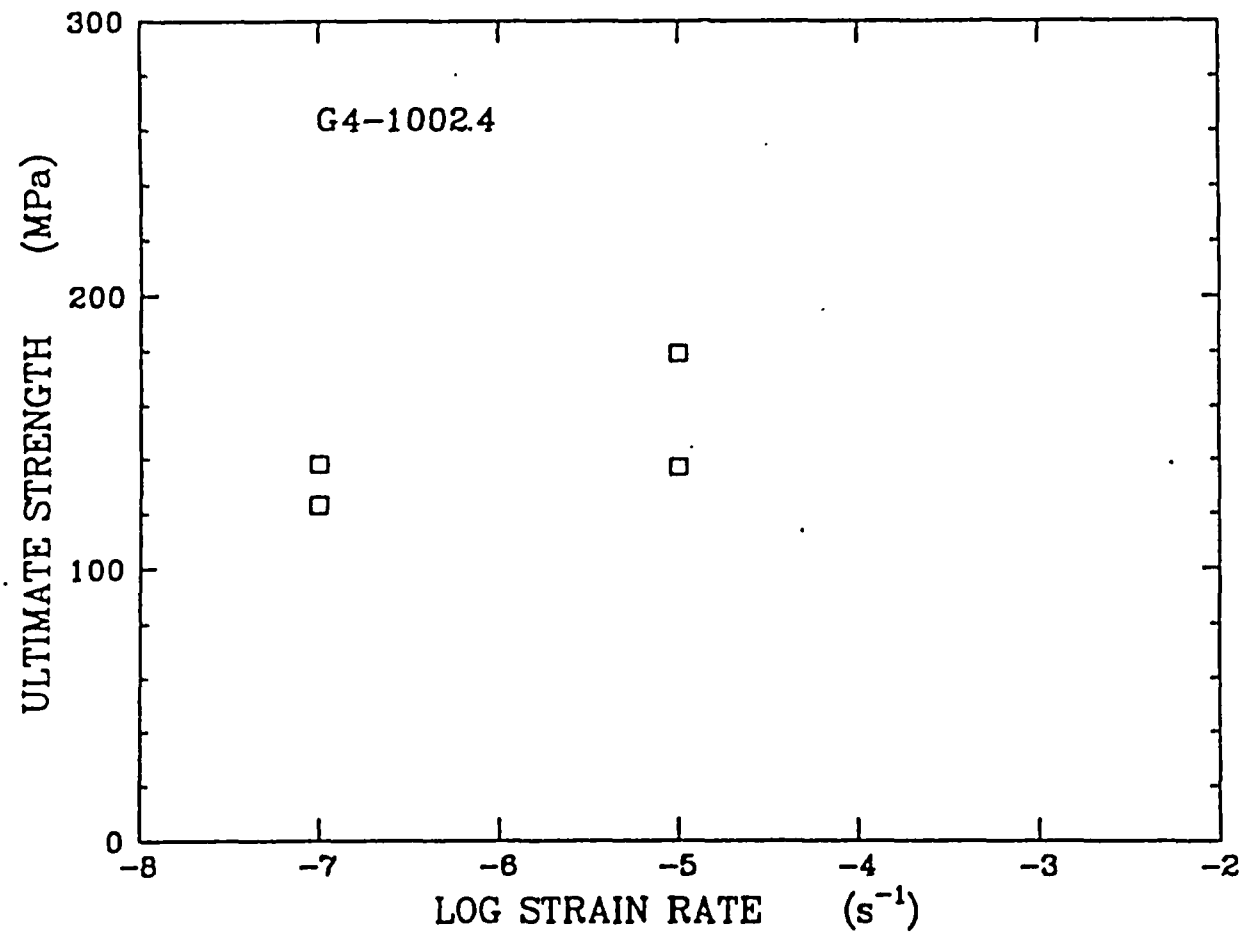

Figure 9b.

Plot of log strain rate versus ultimate differential stress for samples G4-1002.4 deformed in compression at 0.1 MPa confining pressure and room temperature.

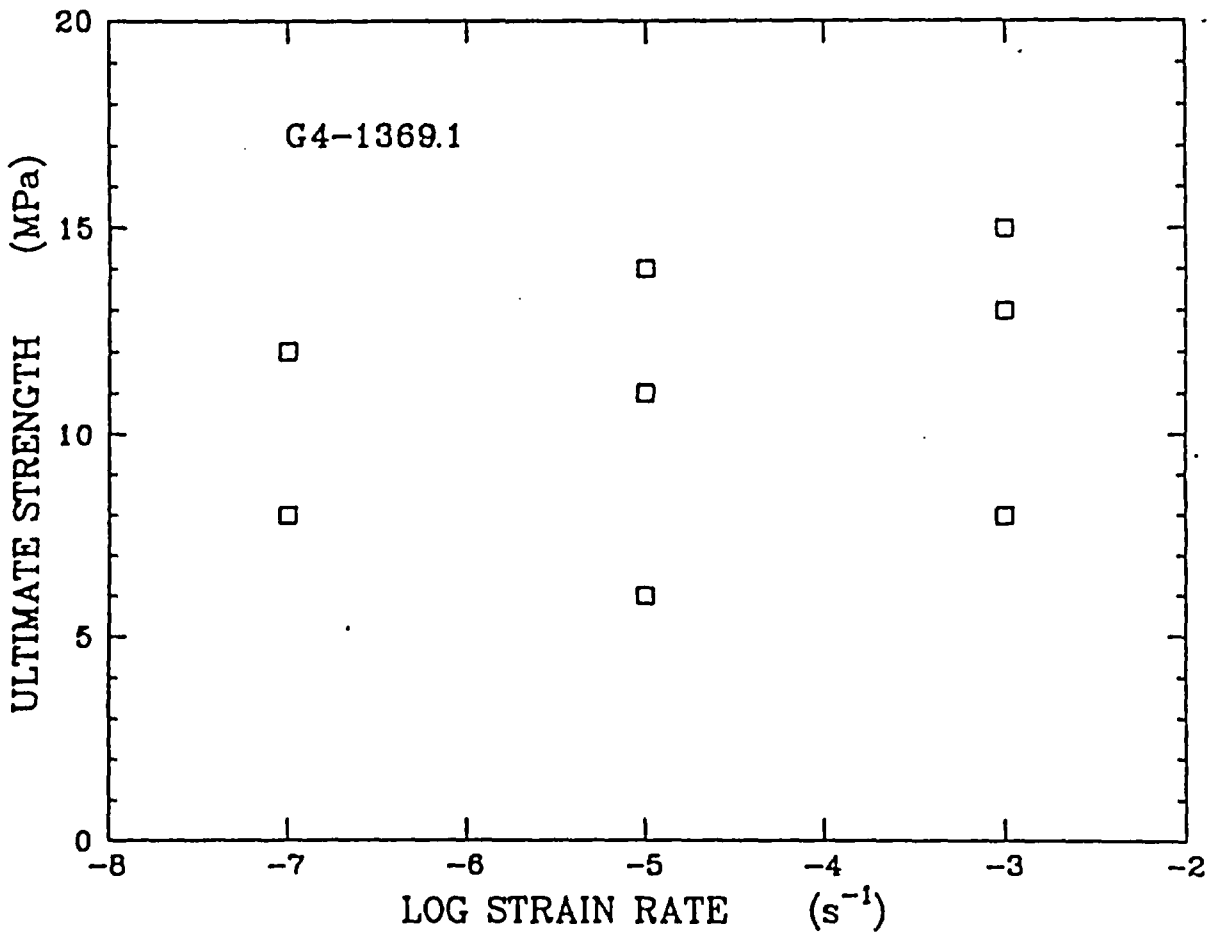

Figure 9c.

Plot of log strain rate versus ultimate differential stress for samples G4-1369.1 deformed in compression at 0.1 MPa confining pressure and room temperature.

DISTRIBUTION LIST

B. C. Rusche, Director (RW-1)
Office of Civilian Radioactive
Waste Management
U. S. Department of Energy
Forrestal Building
Washington, D. C. 20585

R. Stein (RW-23)
Office of Geologic Repositories
U. S. Department of Energy
Forrestal Building
Washington, D. C. 20585

J. J. Fiore (RW-22)
Program Management Division
Office of Geologic Repositories
U. S. Department of Energy
Forrestal Building
Washington, D. C. 20585

M. W. Frei (RW-23)
Engineering & Licensing Division
Office of Geologic Repositories
U. S. Department of Energy
Forrestal Building
Washington, D. C. 20585

E. S. Burton (RW-25)
Siting Division
Office of Geologic Repositories
U. S. Department of Energy
Forrestal Building
Washington, D. C. 20585

C. R. Cooley (RW-24)
Geosciences & Technology Division
Office of Geologic Repositories
U. S. Department of Energy
Forrestal Building
Washington, D. C. 20585

V. J. Cassella (RW-22)
Office of Geologic Repositories
U. S. Department of Energy
Forrestal Building
Washington, D. C. 20585

T. P. Longo (RW-25)
Program Management Division
Office of Geologic Repositories
U. S. Department of Energy
Forrestal Building
Washington, D. C. 20585

C. Klingsberg (RW-24)
Geosciences & Technology Division
Office of Geologic Repositories
U. S. Department of Energy
Forrestal Building
Washington, D. C. 20585

B. G. Gale (RW-25)
Siting Division
Office of Geologic Repositories
U. S. Department of Energy
Forrestal Building
Washington, D. C. 20585

R. J. Blaney (RW-22)
Program Management Division
Office of Geologic Repositories
U. S. Department of Energy
Forrestal Building
Washington, D. C. 20585

R. W. Gale (RW-40)
Office of Policy, Integration, and
and Outreach
U. S. Department of Energy
Forrestal Building
Washington, D. C. 20585

J. E. Shaheen (RW-44)
Outreach Programs
Office of Policy, Integration,
and Outreach
U. S. Department of Energy
Forrestal Building
Washington, D. C. 20585

J. O. Neff
Salt Repository Project Office
U. S. Department of Energy
505 King Avenue
Columbus, OH 43201

D. C. Newton (RW-23)
Engineering & Licensing Division
Office of Geologic Repositories
U. S. Department of Energy
Forrestal Building
Washington, D. C. 20585

O. L. Olson, Manager
Basalt Waste Isolation Project Office
U. S. Department of Energy
Richland Operations Office
Post Office Box 550
Richland, WA 99352

D. L. Vieth, Director (4)
Waste Management Project Office
U. S. Department of Energy
Post Office Box 14100
Las Vegas, NV 89114

D. F. Miller, Director
Office of Public Affairs
U. S. Department of Energy
Post Office Box 14100
Las Vegas, NV 89114

D. A. Nowack (12)
Office of Public Affairs
U. S. Department of Energy
Post Office Box 14100
Las Vegas, NV 89114

B. W. Church, Director
Health Physics Division
U. S. Department of Energy
Post Office Box 14100
Las Vegas, NV 89114

Chief, Repository Projects Branch
Division of Waste Management
U. S. Nuclear Regulatory Commission
Washington, DC 20555

Document Control Center
Division of Waste Management
U. S. Nuclear Regulatory Commission
Washington, DC 20555

S. A. Mann, Manager
Crystalline Rock Project Office
U. S. Department of Energy
9800 South Cass Avenue
Argonne, IL 60439

K. Street, Jr.
Lawrence Livermore National Laboratory
Post Office Box 808
Mail Stop L-209
Livermore, CA 94550

L. D. Ramspott (3)
Technical Project Officer for NNWSI
Lawrence Livermore National Laboratory
Post Office Box 808
Mail Stop L-204
Livermore, CA 94550

W. J. Purcell (RW-20)
Office of Geologic Repositories
U. S. Department of Energy
Forrestal Building
Washington, D. C. 20585

D. T. Oakley (4)
Technical Project Officer for NNWSI
Los Alamos National Laboratory
Post Office Box 1663
Mail Stop F-619
Los Alamos, NM 87545

W. W. Dudley, Jr. (3)
Technical Project Officer for NNWSI
U. S. Geological Survey
Post Office Box 25046
418 Federal Center
Denver, CO 80225

NTS Section Leader
Repository Projects Branch
Division of Waste Management
U. S. Nuclear Regulatory Commission
Washington, DC 20555

V. M. Glanzman
U. S. Geological Survey
Post Office Box 25046
913 Federal Center
Denver, CO 80225

P. T. Prestholt
NRC Site Representative
1050 East Flamingo Road
Suite 319
Las Vegas, NV 89109

M. E. Spaeth
Technical Project Officer for NNWSI
Science Applications International, Corp.
2769 South Highland Drive
Las Vegas, NV 89109

SAIC-T&MSS Library (2)
Science Applications International, Corp.
2950 South Highland Drive
Las Vegas, NV 89109

W. S. Twenhofel, Consultant
Science Applications International, Corp.
820 Estes Street
Lakewood, CO 80215

A. E. Gurrola, General Manager
Energy Support Division
Holmes & Narver, Inc.
Post Office Box 14340
Las Vegas, NV 89114

J. A. Cross, Manager
Las Vegas Branch
Fenix & Scisson, Inc.
Post Office Box 15408
Las Vegas, NV 89114

N. Duncan (RW-44)
Office of Policy, Integration,
and Outreach
U. S. Department of Energy
Forrestal Building
Washington, D. C. 20585

J. Fordham
Desert Research Institute
Water Resources Center
Post Office Box 60220
Reno, NV 89506

J. B. Wright
Technical Project Officer for NNWSI
Westinghouse Electric Corporation
Waste Technology Services Division
Nevada Operations
Post Office Box 708
Mail Stop 703
Mercury, NV 89023

ONWI Library
Battelle Columbus Laboratory
Office of Nuclear Waste Isolation
505 King Avenue
Columbus, OH 43201

W. M. Hewitt, Program Manager
Roy F. Weston, Inc.
2301 Research Blvd., 3rd. Floor
Rockville, MD 20850

H. D. Cunningham, General Manager
Reynolds Electrical & Engineering Company, Inc.
Post Office Box 14400
Mail Stop 555
Las Vegas, NV 89114

T. Hay, Executive Assistant
Office of the Governor
State of Nevada
Capitol Complex
Carson City, NV 89710

R. R. Loux, Jr., Director (3)
Nuclear Waste Project Office
State of Nevada
Capitol Complex
Carson City, NV 89710

C. H. Johnson, Technical Program Manager
Nuclear Waste Project Office
State of Nevada
Capitol Complex
Carson City, NV 89710

Dr. M. Mifflin
Desert Research Institute
Water Resources Center
Suite 1
2505 Chandler Avenue
Las Vegas, NV 89120

Department of Comprehensive Planning
Clark County
225 Bridger Avenue, 7th Floor
Las Vegas, NV 89155

Lincoln County Commission
Lincoln County
Post Office Box 90
Pioche, NV 89043

Community Planning and Development
City of North Las Vegas
Post Office Box 4086
North Las Vegas, NV 89030

City Manager
City of Henderson
Henderson, NV 89015

N. A. Norman
Project Manager
Bechtel National Inc.
Post Office Box 3965
San Francisco, CA 94119

F. Butler
Los Alamos Technical Associates
1650 Trinity Drive
Los Alamos, NM 87544

T. G. Barbour
Science Applications
International Corporation
1626 Cole Boulevard, Suite 270
Golden, CO 80401

Planning Department
Nye County
Post Office Box 153
Tonopah, NV 89049

Economic Development Department
City of Las Vegas
400 East Stewart Avenue
Las Vegas, NV 89101

Director of Community Planning
City of Boulder City
Post Office Box 367
Boulder City, NV 89005

Commission of European Communities
200 Rue de la Loi
B-1049 Brussels
BELGIUM

Technical Information Center
Roy F. Weston, Inc.
2301 Research Boulevard,
Third Floor
Rockville, MD 20850

R. Harig
Parsons, Brinkerhoff, Quade, &
Douglass, Inc.
1625 Van Ness Avenue
San Francisco, CA 94109-3678

Dr. M. M. Singh, President
Engineers International, Inc.
98 East Naperville Road
Westmont, IL 60559-1595

Dr. N. L. Carter, Director
Center for Tectonophysics
Texas A& M University
College Station, TX 77843

RE/SPEC, Inc. (2)
Post Office Box 725
Rapid City, SD 57701
Attention:
P. F. Gnirk
P. E. Senseny

RE/SPEC, Inc. (2)
Post Office Box 14984
Albuquerque, NM 87191
Attention:
S. W. Key
D. K. Parrish

R. Coppage, Senior Mining Engineer
Fenix & Scisson, Inc.
Post Office Box 498
Mercury, NV 89023

Christopher Barton
U. S. Geological Survey
Post Office Box 327
Mercury, NV 89023

Eugene P. Binnall
Field Systems Group
Building 50B/4235
Lawrence Berkeley Laboratory
University of California
Berkeley, CA 94720

1510	J. W. Nunziato
1520	D. J. McCloskey
1521	R. D. Krieg
1524	K. W. Schuler
1524	W. W. Sullivan
1530	L. W. Davison
1534	J. R. Asay
1540	W. C. Luth
1541	H. C. Hardee
1542	B. M. Butcher
1542	L. S. Costin
1542	D. J. Holcomb
1542	W. A. Olsson
1542	R. H. Price (20)
1542	L. W. Teufel
1542	W. R. Wawersik
1543	T. M. Gerlach
3141	S. A. Landenberger (5)
3151	W. L. Garner (3)
3154-3	C. H. Dalin, for DOE/OSTI (28)
6300	R. W. Lynch
6310	T. O. Hunter
6310	NNWSICF
6311	L. W. Scully
6311	L. Perrine (2)
6312	F. W. Bingham
6312	B. S. Langkopf
6313	T. E. Blejwas
6313	F. B. Nimick (20)
6313	B. M. Schwartz (2)
6313	R. M. Zimmerman
6314	S. J. Bauer
6314	B. L. Ehgartner
6314	L. M. Ford
6314	A. J. Mansure
6314	J. R. Tillerson
6315	S. Sinnock
6315	D. H. Zeuch
6332	WMT Library (20)
6430	N. R. Ortiz
7417	F. L. McFarling
8024	P. W. Dean

Org.	Bldg.	Name	Rec'd by	Org.	Bldg.	Name	Rec'd by

Sandia National Laboratories